EPFL

Thèse n° 9081

Universal Aspects of Metamagnetic Transitions in Frustrated Ising Chains

Présentée le 12 août 2021

Faculté des sciences de base
Laboratoire de magnétisme quantique
Programme doctoral en physique

pour l'obtention du grade de Docteur ès Sciences

par

Nagabhushan GANESH HEGDE

Acceptée sur proposition du jury

Prof. J. H. Dil, président du jury
Prof. H. M. Rønnow, Dr I. Zivkovic, directeurs de thèse
Prof. S. Giblin, rapporteur
Prof. P. M. Derlet, rapporteur
Prof. O. Yazyev, rapporteur

École
polytechnique
fédérale
de Lausanne

2021

ಧರ್ಮ, ಧ್ಯಾನ, ತಪಸ್ಯೆಗಳನ್ತೆಯೆ ವಿಜ್ಞಾನವು ಸಾಕ್ಷಾತ್ಕಾರದ ಒಂದು ದಾರಿ

- ಪೂರ್ಣಚಂದ್ರ ತೇಜಸ್ವಿ

Acknowledgements

First of all, I would like to thank my thesis director Prof. Henrik M. Rønnow for providing me a unique opportunity to work in an outstanding research environment. It has always been a delight to discuss physics with him where he comes up with unique ideas. His subject knowledge, keen attention to detail, and incredible problem-solving skills have helped me to understand a bigger picture of the subject. He has also provided me various opportunities to participate in schools, conferences, and experiments at large facilities. I would also like to express my gratitude to my co-supervisor Dr. Ivica Zivkovic without whom my journey would not have been a fruitful one. He has constantly mentored me to understand the subject, and interactions with him have made me a better student of science. He has also actively encouraged me to learn and gain experience during beamtime at PSI, ILL, and BNL. I am grateful to my supervisors for all the guidance and encouragement throughout the years.

Special thanks to Dr. Richard Gaal for his constant assistance in the lab, and David (Wen Hua Bi) for helping me with single-crystal XRD. Discussions with Dr. Jian Rui Soh have helped me to gain a conceptual understanding of difficult topics. Dr. Virgile Favre has patiently taught me to understand the concepts of data analysis and programming at earlier times in my studies. Many thanks to all the members of our group for the memorable moments: discussions during coffee, rafting in the Aare river, hiking and skiing excursions, age of empire and karaoke sessions, beamtime with Virgile, bike rides with Thomas, and much more. I wish all of you good luck in your future endeavors. I would also like to thank the collaborators and workshop for their assistance with my projects.

I have been very fortunate to meet some amazing people during this journey. It has been fun to be part of football organizations, sports, and movies with Aditya Hebbar. I wish you all the best in Paris. During the pandemic, I socialized more with my friends at Triaudes: Ankit, Mukesh, Rasool, Maulik, Harshvardhan, Shantanu, Shreyas, Richa, and Nihar. This place has been a comforting environment with random events of cooking, barbecues, hiking in mountains, travelling, chai pe charcha, and much more. Akshay and Mona always invited me to their place and served excellent Indian food. Further, I enjoyed rock and roll events with Juliette, skiing and hiking with Jeroen, and learnt how to make an authentic pizza with Carlos. My journey also involved some crazy events like rafting in lake Leman and getting rescued by lifeguards, getting lost while hiking in Gasterntal valley, and cycling in Gotthard pass.

I am thankful to Mukesh and Aditya who have always helped me to get back on track during

difficult times. It has been a pleasure to meet my special friend Shasha, who supported me during my thesis. All the best for your masters' studies.

Lastly, I would like to thank my family and friends back at home for their constant support during my stay here. This thesis is dedicated to my parents and my sister Bhoomika for constantly believing in me.

Lausanne **Nagabhushan Ganesh Hegde**
July 27, 2021

Abstract

Frustrated Ising chain systems display plethora of exotic features and intriguing phenomena like magnetization plateaus, extreme long time scales, structural anomalies to mention a few. Although widely studied most of the research on magnetization plateaus have been cornered around finding the exact spin configuration. A general interest to understand the dynamical aspects of jumps in magnetization curve between two plateaus or a plateau and saturation has been neglected. In Ising chains of Co oxides, a jump in magnetization between $1/3^{\mathrm{rd}}$ plateau to saturation has been reported in few materials with different ground state characteristics. This has brought our attention to study these metamagnetic transitions not only from the material perspective but also from a general point-of-view how universal are these first-order transitions, which has never been inspected before. In this project we seek to eliminate compound specific features and investigate universal aspects of metamagnetic transitions in frustrated ising chains. Here we propose to investigate universal aspects by scaling magnetization curves using data collapse on three chosen samples $Ca_3Co_2O_6$, CoV_2O_6 and $CoCl_2{\cdot}2H_2O$, which exhibit metamagnetic transitions between $1/3^{\mathrm{rd}}$ magnetization plateau to saturation.

Material specific investigation was carried out on each of these samples to study their magnetization profiles and phase diagrams. Additional analysis was carried out specifically on $Ca_3Co_2O_6$ to obtain information on relaxation time and energy barriers as well as investigate new features observed around SDW-CAFM phase transition. Magnetization, susceptibility and heat capacity were the primary experimental technique employed during the project. Coherent x-ray scattering and magnetic SANS measurements were further proposed to investigate the characteristics of finite correlations across metamagnetic transitions.

This thesis presents a preliminary study of similarity in metamagnetic transitions combining different experimental techniques with an attempt to eliminate material specific behavior. Results and implications of this research are discussed subsequently.

Keywords: Metamagnetic phase transitions, Similarity, Ising chains, Superparamagnet susceptibility

Résumé

Les systèmes de chaînes d'Ising frustrées présentent une pléthore de caractéristiques exotiques et de phénomènes intrigants comme les plateaux de magnétisation, les échelles de temps extrêmement longues, les anomalies structurelles, pour n'en citer que quelques-uns. Bien que largement étudiées, la plupart des recherches sur les plateaux de magnétisation ont été limitées à la recherche de la configuration exacte du spin. L'intérêt général de comprendre les aspects dynamiques des sauts de la courbe de magnétisation entre deux plateaux ou entre un plateau et la saturation a été négligé. Dans les chaînes d'Ising des oxydes de Co, un saut de magnétisation entre le plateau 1/3 et la saturation a été rapporté dans quelques matériaux avec des caractéristiques d'état fondamental différentes. Cela a attiré notre attention sur l'étude de ces transitions métamagnétiques, non seulement du point de vue du matériau, mais aussi d'un point de vue général sur l'universalité de ces transitions de premier ordre, qui n'ont jamais été inspectées auparavant. Dans ce projet, nous cherchons à éliminer le comportement spécifique des composés et à étudier les aspects universels des transitions métamagnétiques dans les chaînes d'Ising frustrées. Nous proposons ici d'étudier l'universalité en mettant à l'échelle les courbes d'aimantation en utilisant l'effondrement des données sur trois échantillons choisis : $Ca_3Co_2O_6$, CoV_2O_6 et $CoCl_2{\cdot}2H_2O$, qui présentent des transitions métamagnétiques entre le plateau d'aimantation de 1/3 et la saturation.

Des recherches spécifiques aux matériaux ont été menées sur chacun de ces échantillons pour étudier leurs profils de magnétisation et leurs diagrammes de phase. Une analyse supplémentaire a été effectuée spécifiquement sur $Ca_3Co_2O_6$ pour obtenir des informations sur le temps de relaxation et les barrières énergétiques ainsi que pour étudier les nouvelles caractéristiques observées autour de la transition de phase SDW-CAFM. La magnétisation, la susceptibilité et la capacité thermique ont été les principales techniques expérimentales employées au cours du projet. Des mesures de diffusion cohérente des rayons X et de SANS magnétique ont également été proposées pour étudier les caractéristiques des corrélations finies à travers les transitions métamagnétiques.

Cette thèse présente une étude préliminaire de similarité dans les transitions métamagnétiques combinant différentes techniques expérimentales avec une tentative d'éliminer le comportement spécifique du matériau. Les résultats et les implications de cette recherche sont discutés par la suite.

Mots clés : Transitions de phase métamagnétiques, Similarité, Chaînes d'Ising, Susceptibilité des superparamagnets.

Contents

Acknowledgements i

Abstract iii

Résumé v

List of figures xi

1 General Theory 1

- 1.1 Phase Transitions 1
  - 1.1.1 Classification of Phase Transitions 1
  - 1.1.2 Characteristics of First-order Transitions 2
- 1.2 Metamagnetic Phase Transitions 4
  - 1.2.1 Metastable Plateaus: "Stairway to Saturation" 4
  - 1.2.2 Ising Chains in Co Oxides 4
- 1.3 Critical Phenomena 7
  - 1.3.1 Universal Behavior in Metamagnetic Transitions 8
  - 1.3.2 Supercriticality and Widom lines 9
- 1.4 Magnetic Relaxation 9
  - 1.4.1 Slow Dynamics 11
  - 1.4.2 Energy Barrier: Climbing or Tunneling ? 12

2 Samples: Structural and Magnetic Properties 15

- 2.1 $Ca_3Co_2O_6$: Ising Chains on Regular Triangular Lattice 15
- 2.2 CoV_2O_6: Ising Chains on Distorted Triangular Lattice 19
- 2.3 $CoCl_2{\cdot}2D_2O$: Ising Chains on Two Sub-lattice Structure 22

3 Experimental Methods and Instrumentation 25

- 3.1 Magnetometry 25
  - 3.1.1 Magnetization 25
  - 3.1.2 Susceptibility 25
  - 3.1.3 Magnetometers 26
- 3.2 Heat capacity 31
- 3.3 Neutron Experiments 33
  - 3.3.1 Magnetic Small Angle Neutron Scattering 34

    3.3.2 Sample Preparation 36
  3.4 X-ray Experiments 36
    3.4.1 Coherent Soft X-ray Scattering 37
    3.4.2 Sample Preparation using Focused Ion Beam 37

4 Similarity Prospects for Staircase Magnetization 39
  4.1 Inspection of Field-induced Magnetization across $\uparrow\uparrow\downarrow\longleftrightarrow\uparrow\uparrow\uparrow$ Transition 39
    4.1.1 Case 1: $Ca_3Co_2O_6$ 39
    4.1.2 Case 2: CoV_2O_6 44
    4.1.3 Case 3: $CoCl_2{\cdot}2D_2O$ 46
  4.2 Disparate Origin and Similarity 48
    4.2.1 Data Collapse 48
    4.2.2 Scaling Diagram 51
  4.3 Conclusion 52

5 Dynamical Aspects of Metamagnetic Transitions 53
  5.1 Near Identical Superparamagnet-like Behavior in $\mathscr{T}_0$ and $\mathscr{T}_+$ Transitions 53
  5.2 Investigation of Slow Dynamics across $\mathscr{T}_+$ transition in $Ca_3Co_2O_6$ 55
    5.2.1 Implementation of Cole-Cole Model 58
    5.2.2 Relaxation Time and Energy Barrier 59
    5.2.3 Discussion 61
  5.3 Synonymous Slow Dynamics in $CoCl_2{\cdot}2D_2O$ and CoV_2O_6 63
  5.4 Comparison and Conclusion 65

6 Endeavor for Microstructure Determination using Magnetic SANS 67
  6.1 Origin of Ferrimagnetic Nano-fluctuations at Zero-field 67
  6.2 Nano-phase Characteristics across $\mathscr{T}_+$ Transition 69
    6.2.1 Detector Images 69
    6.2.2 Analysis of Scattered Intensity 69
  6.3 Discussion and Conclusion 70

7 Search for Nano-fluctuations using Coherent Soft X-ray Scattering 73
  7.1 Experimental Details 73

8 Emergence of New Phase over $\mathscr{T}_0$ Transition in $Ca_3Co_2O_6$ 75
  8.1 Initial Observations from Magnetization Measurements 75
  8.2 Distinct Dynamic Features of Intermediate Phase 77
  8.3 Thermomagnetic Hysteresis 79
  8.4 Discussion and Conclusion 81

9 Summary 85

10 Outlook 87

A Linear Response Theory **89**
A.1 Single Relaxation Time 90
A.2 Generalized Debye Model 90
A.3 Uniqueness Criteria 91

B Cole-Cole Distribution **93**

C Superparamagnet Susceptibility **95**
C.1 Probability Distributions 97

D Code to Fit Superparamagnet Susceptibility **101**

Bibliography **105**

Curriculum Vitae **115**

List of Figures

1.1 (a) $Ca_3Co_2O_6$, (b) CoV_2O_6 and (c) $CoCl_2{\cdot}2H_2O$ exhibit plateau at $(1/3)^{rd}$ of magnetization at saturation. Despite different origin and behavior at zero-field all three materials display seemingly different $\uparrow\uparrow\downarrow\longleftrightarrow\uparrow\uparrow\uparrow$ transition. 6

1.2 A remarkable collapse of metamagnetic transition between $1/3^{rd}$ plateau and saturation state in materials whose magnetic ions are transition and rare-earth elements. This inspires us to investigate universal aspects of metamagnetic transitions where the phenomena supersedes the inception of magnetic behavior in respective materials. In both figures magnetization is normalized to respective M_s, and magnetic field is scaled. 6

1.3 The framework of critical phenomena built using the themes of scaling relations, universality and renormalization. 7

1.4 Temperature dependence of reduced magnetization data for five different materials ($CrBr_3$, EuO, Ni, YiG and Pd_3Fe) have been collapsed into a single curve. Not any of these materials are idealized ferromagnet. Despite different individual magnetic properties it has been possible to scale the data using $d = 3$ Heisenberg model. This figure is reused with permission from this article [1]. A metric to quantify data collapse for two thermodynamic parameters from scaling analysis is proposed here [2]. 9

1.5 Approximate time-scales of different experimental techniques. 10

1.6 Doubly degenerate spin states. Conventionally spontaneous reversal between the two spin states occur by jumping across the energy barrier. At low temperatures the switching mechanism can happen via quantum tunneling. 12

1.7 A double well picture demonstrating quantum tunneling of magnetization. (a) at zero-field M_s levels on left and right in resonance. (b) at non-zero magnetic field this degeneracy is lifted. (c) for some values of magnetic field M_s levels on left and right are in resonance. 14

2.1 Crystal structure of $Ca_3Co_2O_6$. The structure consists of 1d Ising chains running along *c* axis. In the perpendicular direction these chains are arranged on a triangular lattice in *ab* plane. Non-magnetic Calcium ions occupy the space between chains. Spins are shown pictorially to showcase the easy axis. 16

2.2 Crystal structure of α-CoV_2O_6. The magnetic ion Co^{2+} forms an octahedra with surrounding O ions. Quasi 1d chains are observed to be along b-direction with ising spins pointing parallel to c-axis. 19

2.3 Schematic of parallelogram cell in ac-plane of crystalline α-CoV_2O_6. Each circle denotes one magnetic chain perpendicular to the plane, and the cell is divided into four scalene triangles with three edges. Each triangle has dimensions of $a/2$, c and d with exchange interactions J_1, J_3 and J_2 respectively. 20

2.4 Crystal structure of $CoCl_2 \cdot 2H_2O$. The structure consists of 1d chains along c axis. Every Co^{2+} ion is surrounded by two O^{2-} along b direction and four Cl^- in ab plane. Ising nature of spins is observed parallel to b axis which makes it the easy axis. 22

2.5 Spin configurations of $CoCl_2{\cdot}2H_2O$. Blue dots indicate ↑ spins and red indicate ↓. (a) AFM (b) FiM and (c) FM spin structures are attained when an external magnetic field is applied parallel to the easy axis. This schematic is cross-section of Ising spin chain coming out-of-plane. J_1 is the nearest neighbor exchange interaction (solid line) where as J_2 (dashed line) and J_3 (dash-dotted line) are next-nearest neighbor interactions. Unlike $Ca_3Co_2O_6$ there is no obvious frustration in spin arrangements [4]. 24

3.1 Ac susceptibility demonstrated as gradient of magnetization. The red line is the measure of gradient and blue line is the dc magnetic field applied (H_{dc}). A small excitation field H_{ac}, which is sinusoidal in nature, is superimposed on H_{dc}. Magnetization obtained in the presence of H_{ac} is given by M_{ac}. 26

3.2 Schematic of VSM. A sample is positioned in the region of uniform magnetic field generated by electromagnets. Using a motor this sample is vibrated and the induced voltage due to change in flux is recorded by the pick-up coils. . . . 27

3.3 Schematic of ac susceptometer is shown in (a). Either ac current or voltage source is used to generate ac field. Lock-in amplifiers are used to eliminate noise and extract signal obtained from the pick-up coils. A schematic of cryostat containing ac, dc (optional) and pick-up coils is shown in (b). The sample under study is positioned in the region between a pair of pick-up coils. 28

3.4 Schematic of superconducting pick-up loop in a SQUID is shown in (a). The pick-up and secondary coils are counter wound. (b) Change in flux giving rise to a response in voltage. The periodicity of voltage is one quantum flux. 30

3.5 Schematic of thermal connections to sample and platform in specific heat option. Apiezon grease facilitates thermal connection between the sample and platform. A thermometer and heater are placed on the undersurface suspended by platinum wires which are connected to the surrounding thermal bath. Heat capacity measurements were carried out in Quantum Design PPMS HC module. 31

3.6 Schematic of SANS experimental setup. Using a velocity selector or chopper incident neutrons of a band of wavelengths are filtered out. Devices like polarizer (P), spin-flipper (F) and analyzer (A) are optionally used in the setup. The sample is placed between velocity selector and detector. Neutrons (of wave vector $k0$) are incident of the sample and scattered neutrons $k1$ are detected on the detector. q is the scattering vector, which depend on neutron wavelength λ and scattering angle ψ. SD is the distance between sample and detector. On the detector image angular anisotropy is given by θ, and r is the radial distance from the beam center. 35

3.7 Sample holder for SANS experiment. (a) Sample is glued horizontally in the middle of the holder. (b) Aluminum foil wrapped to on the whole plate 36

3.8 Prethinned samples of $Ca_3Co_2O_6$ were prepared using focused ion beam in two different orientations for measurements in reflection and transmission mode. . 38

4.1 Field-induced magnetization profile of $Ca_3Co_2O_6$ for $T \geq 10$ K. Metamagnetic transitions $\mathscr{T}_0$ and $\mathscr{T}_+$, and kink ($\bar{K}$) developed at high temperatures are denoted using arrows. Magnetization fieldscan at $T = 2$ K with significant hysteretic effects. Additional steps are highlighted with arrows. 40

4.2 A cluster spins completely polarized at higher magnetic fields ($B >> B_c$). On decreasing the field an excitation occurs, followed by consecutive spin flips on further decreasing the field approaching B_c. 40

4.3 Field-induced magnetization at 20 K, and derivatives. $\frac{dM}{dB}$ exhibits a maximum across in-field transition. $\frac{d^2M}{dB^2}$ across in-field transition has an inflection point at magnetic field corresponding to max($\frac{dM}{dB}$). 41

4.4 B-T field phase diagram of $Ca_3Co_2O_6$. The plateaus at $1/3M_s$ and M_s are approximately shaded. A line is drawn at 10 K below which hysteretic behavior emerges. Dashed lines indicate appearance of additional steps at low temperatures. The ordered state breaks down at 25 K where the system enter paramagnetic state. . 42

4.5 Temperature dependence of the max($\frac{dM}{dB}$) across the $\mathscr{T}_+$ transition. A sudden drop is observed below 10 K which indicates appearance of different magnetic behavior. 43

4.6 Temperature dependence of $\frac{M}{M_s}$ at the kink, which saturates to 2/3 approaching 10 K. A possible configuration at the kink at low temperatures could be 5 ↑ and 1 ↓ state or 2 ↑ and 1 partially disordered state. Near T_N the spin configuration at the kink could be 2 ↑ and 1 ↓ state. 43

4.7 Field-induced magnetization curves in CoV_2O_6 at temperatures where the metamagnetic transitions are apparent. In-field transitions $\mathscr{T}_I$ and $\mathscr{T}_{II}$ are indicated with arrows. The kink $\bar{K}$ in CoV_2O_6 is less pronounced compared to other two samples. Also the kink here is developed in $\mathscr{T}_I$ transition. 44

4.8 Field-induced magnetization and corresponding $\frac{dM}{dB}$ close to T_c. One can notice that for $T > 10$ K $\mathscr{T}_{II}$ transition becomes wider and eventually terminates at 10.4 K. $\mathscr{T}_I$ transition is observed beyond T_c until the ordering is suppressed at T_N. . 44

4.9 B - T phase diagram of CoV_2O_6. Phase boundary corresponding to $\mathscr{T}_{II}$ terminates at a crossover temperature T_c, leading to the existence of a supercritical region. 45

4.10 Temperature dependence of max($\frac{dM}{dB}$) in CoV_2O_6. At crossover temperature the trajectory of max($\frac{dM}{dB}$) for $\mathscr{T}_I$ undergoes a major deviation. At low temperatures another energy scale develops which results in decline of max($\frac{dM}{dB}$) for both transitions. 45

4.11 Magnetization fieldscan profile of $CoCl_2 \cdot 2D_2O$. Metamagnetic transitions $\mathscr{T}_I$ and $\mathscr{T}_{II}$, and kink $\bar{K}$ are indicated using arrows. At higher temperatures ($T > T_{MC}$) a kink ($\bar{K}$) is observed which itself is the transition ($\mathscr{T}_{III}$). 46

4.12 $\frac{dM}{dB}$ of magnetization curves have been used to inspect the termination of $\mathscr{T}_I$ and $\mathscr{T}_{II}$ close to T_{MC}. Beyond 9.4 K only $\mathscr{T}_{III}$ exists. 47

4.13 B-T phase diagram of $CoCl_2 \cdot 2D_2O$. A multicritical point is observed close to 9.4 K, denoted using an arrow. B_0^I and B_0^{II} indicate magnetic fields at which phase boundaries saturate at low temperatures. 47

4.14 Temperature dependence of max($\frac{dM}{dB}$) in $CoCl_2 \cdot 2D_2O$. Notice the sudden drop in max($\frac{dM}{dB}$) of $\mathscr{T}_I$ below 3 K due to a different energy scale which doesn't affect $\mathscr{T}_{II}$. 47

4.15 Comparison of $Ca_3Co_2O_6$ fieldscan at 18.5 K with several fieldscans of CoV_2O_6. Best overlap of fieldscan profiles is observed in (b). In (a), (c) and (d) the profiles appears to overlap well yet there exists slight mismatch at higher fields. These comparisons are observational and are not statistically analyzed. 49

4.16 Comparison of $Ca_3Co_2O_6$ fieldscan at 18.5 K with fieldscans of CoV_2O_6 at 7.6 K (a) and 8 K (b). The former plot showcases data collapse close to saturation ($\uparrow\uparrow\uparrow$), and the latter one at the plateau ($\uparrow\uparrow\downarrow$). 50

4.17 Re-scaling magnetic field (x-axis) of CoV_2O_6 in order to make a comparison with that of $CoCl_2 \cdot 2D_2O$ (a) Original data of individual magnetization profiles (b) A prefactor of 1.405 has been multiplied for comparison. 50

4.18 Re-scaling magnetic field (x-axis) of $CoCl_2 \cdot 2D_2O$ to compare with $Ca_3Co_2O_6$. Comparisons at different temperatures are shown in (a) and (b). 50

4.19 Scaling diagram depicting the scaling behavior of magnetization curves at saturation and 1/3rd plateau. 51

5.1 Temperature dependence of ac susceptibility in $Ca_3Co_2O_6$ for B = 0 T, 3.5 T and 1.85 T. Qualitatively temperature scans of susceptibility in the middle of $\mathscr{T}_0$ and $\mathscr{T}_+$ transitions are alike with no features around T_N. Measurements at the 1/3rd plateau reveal a sharp feature at T_N and a drop in the values to zero at low temperatures. 54

5.2 Ac susceptibility across $\mathscr{T}_+$ transition for T = 10 K. The individual fieldscans are smoothed using a moving average. Real component is presented on the left subplot and imaginary on the right. B_{DC} and B_∞ are indicated using arrows. . . 56

5.3 Color maps of the imaginary component where the maximum amplitude of each frequency profile is normalized to unity 57

5.4 Temperature dependence of the crossover frequency 57

5.5 Frequency dependence of susceptibility at $T = 15$ K for several values of B. Circles represent χ', and triangles show χ''. 58

5.6 Magnetic field and temperature dependence of the frequency f_{max} and width α where χ'' exhibits a maximum. 60

5.7 Temperature dependence of the characteristic frequency at $B = 3.58$ T. The solid line is a fit following the Arrhenius law described in equation 5.3. E_{B} above B_{∞}. 60

5.8 Magnetic field dependence of ac susceptibility across $\mathscr{T}_{\text{II}}$ transition in $CoCl_2{\cdot}2D_2O$. As opposed to $Ca_3Co_2O_6$, signatures of crossover region in frequency are not obvious in the measurement range. [left] χ' vs B at 4 K [middle] χ' vs B at 6 K. The arrow indicates drift of max(χ') towards lower fields with change in frequency [right] χ' vs B at 8 K. Characteristic features are denoted using arrows. 63

5.9 Magnetic field dependence of ac susceptibility across $\mathscr{T}_{\text{II}}$ transition in CoV_2O_6. At all measured temperatures, with change in frequency, max(χ') doesn't alter away from B_{∞}. 64

6.1 SANS detector image obtained at zero-field. [Reused with permission from [5]]. 67

6.2 Correlation lengths of SANS scattering ζ_{ab} and ζ_{c}. Neutron diffraction intensity of long-range order and short-range correlations. The short-range order in diffraction has a comparable T- dependence to the SANS intensity. [Reused with permission from [5]]. 68

6.3 SANS detector images obtained at different temperatures and magnetic fields (a) Detector image at 10 K 0 T. Two parallel streaks are observed as expected. (b) Detector image at 10 K 3.4 T. Single vertical streak is observed which passes through the center of the detector image. (c) Detector image at 11 K 3.4 T. Due to insufficient beam time we could not collect enough statistics at this temperature and field. (d) Detector image at 13 K 3.4 T. The vertical streak is still present. The intensity of this streak is lower than at 10 K. 70

6.4 Lorentzian function has been used to fit scattered intensity. (a) scattered intensity $\parallel$ c- axis, $q_{\parallel\text{c}} \simeq 0.1162$. Higher order peaks couldn't be modeled due to poor quality of data. (b) scattered intensity $\perp$ c- axis, $q_{\perp c} \simeq 0.06707$. 71

7.1 A schematic of sample rod which is transferred into the chamber. Samples of different orientations are mounted as shown in the figure. 73

7.2 Sample detector image in ac transmission mode at two different temperatures 10 K (< T_{N}) and 40 K (> T_{N}). A temperature independent diffuse ring is observed which could be likely from ice formed in the chamber. 74

8.1 Magnetization fieldscan profiles across $\mathscr{T}_0$ transition. Around 10 K the transitions are sharp; with increase in temperature they broaden. Above 14 K two metamagnetic transitions occur at symmetric non zero-field. An intermediate phase emerges in-between the two transitions. 75

8.2 Over-plot of magnetization fieldscan and corresponding differential susceptibility across $\mathscr{T}_0$ transition to visualize emergence of intermediate phase. At $T >$ 14 K $\max(\frac{dM}{dB})$ shifts to a non-zero positive field value and an additional peak appears at negative field value in $\frac{dM}{dB}$ profile. The transitions move further away from zero-field with subsequent increase in temperature. 76

8.3 B-T phase diagram of $\mathscr{T}_0$ transition in $Ca_3Co_2O_6$. At low temperatures a single phase boundary separates $\uparrow\downarrow\downarrow$ and $\uparrow\uparrow\downarrow$ spin states. The observed intermediate phase between two phase boundaries is shaded and denoted by IM. The system is in non-equilibrium state during magnetization measurements which has resulted in phase boundaries having an offset in field space. A horizontal dashed line is drawn along zero-field. 76

8.4 Ac susceptibility fieldscans across $\mathscr{T}_0$ transition for T = 10 K, 18 K and 22 K. The individual fieldscans are smoothed using a moving average. At 18 K we can see that at low frequencies fieldscans are skewed depending upon the direction of measurement. However at high frequencies, only one maximum is observed. At 22 K several kinks are distinctly visible denoted using arrows. At different frequencies kinks are observed to happen at slightly different fields. 78

8.5 A standard plot of temperature dependence of specific heat in an insulating magnetic material which orders at T_N. A vertical dashed line is drawn at T_N where C_{total} exhibits a peak or divergence. At low temperatures $C_{lattice}$ obeys T^3 behavior in accordance with Debye model. 79

8.6 Temperature dependence of heat capacity during heating and cooling cycle are shown for selected fields. A peak is observed at T_N indicated in the figure. Thermomagnetic hysteresis is observed at non-zero magnetic fields between ± 0.2 T and ± 0.7 T. 80

8.7 Color plots of specific heat in temperature-field phase space around zero-field. Specific heat measured during heating cycle are displayed on left and cooling cycle on right. Broad features and thermomagnetic hysteresis between heating and cooling cycles are evident from the contour lines. 81

8.8 Taken together the behavior of intermediate phase probed from ac susceptibility and specific heat measurements are summarized in this schematic. The findings related to intermediate phase which exists in the crossover region between two well defined states are mainly focused. 82

8.9 Single component pressure-volume phase diagram. Near the phase boundary liquid, vapor and mixed (liquid-vapor) phases exist as shown in the diagram. The boundary of liquid-vapor region constitutes of saturated liquid and vapor. The region near and above critical point is the supercritical fluid, which in some ways is an arbitrary distinction. Higher temperature isotherms don't indicate a phase change since they are beyond the critical point. In the absence of 'hard' boundary, it may be possible to distinguish phases from a Widom line drawn from response functions, whose local maximum indicates the locus of this line. 83

A.1 Argand diagram, of frequency dependence of susceptibility data for $Ca_3Co_2O_6$ at 15 K and 3.5 T, created using equation A.10. The blue dots are χ" plotted as a function of χ' and the red line is the fit on the data. The black arc is the semi-circle which is expected when the system has single relaxation time. . . . 91

A.2 Frequency dependence of susceptibility with real (a), imaginary (b) parts. Using Cole-Cole equation susceptibility is modeled with $\tau_1/\tau_2 = 100$, plotted for various values of η (in our descriptions we have used the symbol α to quantify 'spread'). This plot is reused with permission from [6]. 92

B.1 As we already know α is a measure of width of Cole-Cole distribution. For different values of α the distribution function is computed. At the lower limit $\alpha \rightarrow 0$, the system is close to having a singe relaxation time. Hence the distribution narrows down. For $\alpha = 0$, the distribution function is a dirac-delta. At the higher limit $\alpha \rightarrow 1$, the system has infinite width due to multiple relaxation times. In this comparison the mean relaxation time (τ_c) is assumed to be around 10^{-4} s. 94

C.1 An example of modeling frequency dependence of susceptibility across $\mathscr{T}_+$ transition in $Ca_3Co_2O_6$. We have considered data at 15 K 3.5 T to show a comparison between different distributions used in generalized Debye model. The real part of susceptibility saturates and low and high frequency limits where as imaginary part displays a bell curve close to the mean relaxation time. (a) A fit was attempted using Debye model (without distribution function). The data can't be fitted using this model due to the existence of multiple relaxation times. Generalized Debye model has been employed to fit the data using (b) Cole-Cole (b) Lognormal and (d) Cauchy-Lorentz distribution functions. All the three distribution functions produce a good fit on the data, however based on goodness-of-fit test Cole-Cole distribution best describes susceptibility data for maximum number of reliable data set. 98

C.2 Comparison of Cole-Cole, Lognormal and Cauchy-Lorentzian distributions in $Ca_3Co_2O_6$ at 15 K 3.5 T. Cole-Cole and Cauchy-Lorentz distribution functions show very similar behavior with smaller width and longer curvatures around the mean relaxation time, compared to Lognormal distribution. 99

1 General Theory

1.1 Phase Transitions

A phase transition is a physical process that takes place when there is singularity in free energy (G) or it's derivatives. An extensive variable that can distinguish between the two phases across a phase transition is termed as order parameter, measures the degree of order and labels the broken symmetry across the phase boundary. When phase transition occurs a non-analytic behavior is observed in free energy for a choice of thermodynamic variable, such that it attains minimum at equilibrium.

A phase boundary in a phase diagram distinguishes two phases at equilibrium. The end point of this phase boundary is the critical point, where the physical properties undergo drastic change. The dynamics slow down, correlation length of fluctuations diverge, and scaling relations of different quantities are described by critical exponents. Using the framework of intuitively appealing although mathematically non-rigorous renormalization theory, behavior of a system at critical region can be systematically investigated at different spatial scales. *Au contraire* correlation length in a first-order transition is finite and universality can't be envisioned [7].

1.1.1 Classification of Phase Transitions

In 1933, Paul Ehrenfest systematized phase transitions based on the behavior of thermodynamic potential with respect to other thermodynamic variables [8]. Prior to this, the concept of a phase transition between phases in homogeneous substances, physical characteristics of critical point, ferromagnetic transition at Curie point etc were already known, but a rigorous classification was yet to be done [9]. In Ehrenfest's classification, the order of phase transition was defined with respect to the lowest derivative of free energy that was discontinuous. This means that for a phase transition to be labeled as n^{th} order, n^{th} derivative of G should be discontinuous, with $(n\text{-}1)^{th}$ derivative being continuous and $(n+1)^{th}$ derivative not defined. According to this scheme, phase transitions of arbitrary integral order could exist. Mathematically, this classification is rigorous and appealing but loses physical significance for an increasing order. Experimentally, it is difficult to measure higher order derivatives of G and corresponding differences between two phases may not be obvious.

At equilibrium, the free energy G of a system can be written with reference to the internal energy U, extensive properties (magnetization M, entropy S) and control parameters (temperature T, magnetic field H) as,

$$G = U - TS + MH + ... \tag{1.1}$$

For example, at the occurrence of a field-induced phase transition, $\left(\partial \Delta G/\partial H\right)_{\mathrm{T,P,...}}$ will yield M which is the order parameter. If M is discontinuous then the phase transition is said to be first-order, otherwise higher-order. In a temperature-induced phase transition, ΔS can't be experimentally measured, instead specific heat C_{p} is used to determine ΔS.

Ehrenfest's classification has certain limitations. It can't explain the order of transition if the derivative of G is continuous but singular. The singularity ensures that next order derivative doesn't exist such that G exhibits non-analytical behavior but no derivative of integer order is discontinuous. This is observed in the case of logarithmically diverging specific heat [10]. Another example would be the existence of metastable states in first-order transitions, which doesn't fit into Ehrenfest theme. Metastable states can influence non-analytical behavior in G without the derivative of G being discontinuous. The conditions for existence of metastable state, limits of metastability, and level of metastability can't be explained from this classification.

In the modern definition phase transitions are classified as either discontinuous (first-order) or continuous (second- and higher order). In first-order transitions the derivative of G is discontinuous for $n = 1$, where as in second-order transitions the derivative of G is continuous for $n = 1$. In latter case, derivative of G with $n = 2$ is either discontinuous or doesn't exist. Higher-order transitions are defined similar to second-order. In first-order transitions phases coexist as a result of latent heat and the correlation length is finite. Neither latent heat nor coexistence of phases is seen in continuous transitions and the transition happens instantaneously, resulting in the associated correlation length diverging to infinity.

1.1.2 Characteristics of First-order Transitions

First-order phase transitions can be mathematically explained from Landau theory where free energy is expanded as a power series on the order parameter field (up to 6^{th} power), by including only those terms that are compatible with the system symmetry [7, 11].

Phase coexistence and latent heat are the elemental features of first-order transition which differentiate it from second-order. For a first-order magnetic phase transition Clausius-Clapeyron equation can be written as,

$$\frac{dH}{dT} = -\frac{L}{T\Delta M} \tag{1.2}$$

where L is latent heat, ΔM is change in magnetization.

Another essential feature of first-order transitions is the existence of metastable states. At critical parameter value both the phases coexist. The free energy of a system has two equal minima, separated by a barrier height that prevents spontaneous transfer from one phase to another. On moving away from critical parameter value, the minima are no longer equivalent such that the absolute minimum corresponds to the stable state and local minimum to metastable. The height of barrier represents the minimum external disturbance required for metastable to stable transformation. Depending upon the direction of phase transition, metastable states allow superheating or supercooling thereby inducing hysteresis across the transition. This confirms that hysteresis is a sufficient but not a necessary condition to determine that phase transition is of first-order. On increasing the parameter value, the barrier height decreases until the local minimum becomes an inflection point. This defines the limit of metastability, beyond which metastable states can't persist. When the system is at the inflection point there is no barrier that prevents the system into stable transformation. This unstable state is a glass state, which is kinetically arrested existing beyond the limits of metastability. Metastable and unstable states can be tuned with an additional control parameter. Absence of latent heat in continuous transitions result in indistinguishable phases at the occurrence of the transition. Therefore the phenomena of metastability and hysteresis are not observed in them [12].

During measurements the observed first-order transitions are not infinitely sharp, instead there exists certain degree of broadness associated with them. For example a transition can spread out over a range of field due to demagnetization effect, where an internal magnetic field is generated by the magnetization in a magnet itself which varies with sample geometry [13]. Consequently the effective field (H_{eff}) acting on the sample is modified, given by

$$H_{\text{eff}} = H - NM \tag{1.3}$$

where H is external field, N is geometry dependent constant, and M is sample magnetization. Due to this effect, the transition is spread out over a range of field. Similar to continuous transitions, finite size effects are observed in first-order transitions, due to which the transition appears to rounded and shifted [14]. Imry and Wortis derived a criterion for rounding of first-order transition due to the presence of quenched impurities, which block the growth of correlations within the system without changing the character of transition [15]. These factors contribute to broadening of the first-order transitions observed in real materials.

There are two major mechanisms which determine the dynamics of first-order transitions in different systems [16]. For metastable systems the dynamics is governed via nucleation and growth, whereas for unstable systems spinodal decomposition is expected, during the process of phase transition. Detailed mathematical description of dynamical aspects are discussed here [7].

1.2 Metamagnetic Phase Transitions

Metamagnetic phase transitions (also known as staircase magnetization) are magnetic field-induced first-order phase transitions between a state with low magnetization (and low susceptibility) and high magnetization (and low susceptibility). In highly anisotropic materials, these transitions are characterized by simple spin reversals along the direction of anisotropy. Earlier researchers claimed two properties to be essential for metamagnetic transitions: presence of strong anisotropy and competing interactions [17]. It has been subsequently found that these transitions are also observed in materials with weak Ising character. Before we get into a thorough analysis of metamagnetic transitions in the upcoming chapters, let us discuss some relevant aspects and related phenomena.

1.2.1 Metastable Plateaus: "Stairway to Saturation"

In magnetic structures, magnetism dictated by correlation between lattice structure and spin coupling can give rise to complex features [18, 19]. One such noticeable feature is the presence of metastable plateaus at rational numbers in units of magnetization at saturation. Quantum or thermal fluctuations are the driving mechanisms for the formation of these plateaus which often represent ground state laying groundwork for emerging dynamics. In these systems translation symmetry is broken when the size of magnetic unit cell is greater than the crystallographic unit cell [20]. An archetypical example of magnetization plateaus is observed in $SrCu_2(BO_3)_2$, which has been in the limelight since 1981 when the exact ground state was calculated by Shastry and Sutherland [21]. In this compound several magnetization plateaus are observed at fractional values of total magnetization (1/8, 1/4, 1/3, ...). Theoretical descriptions has been made on the plateau including topological quantization [22], quantum tunneling of magnetization [23], dimer-monomer model [24] etc. Since the advent of this material, metastable plateaus in frustrated magnets have been one of the prime subjects of interest.

1.2.2 Ising Chains in Co Oxides

Metamagnetic transitions are observed in Ising chains stacked on a 2d lattice with spins pointing parallel or anti-parallel to the easy axis. When magnetic field is applied along the easy axis there is one or multiple spin flips leading to these transitions. Frustrations arise when there is a competition between energies of in-chain and in-plane exchange interactions, shaping the magnetic properties of the material.

Ising chains in ABX_3 family (A alkali metal, B transition metal, X halogen) [25], for example $CsCoCl_3$, $CsCoBr_3$, display partially disordered antiferromagnetic (PDA) state at zero-field with two chains on triangular lattice AF coupled and one chain incoherent [26]. While $A_3A'BO_6$ family are structurally more complex than the former with stacked chain containing face-sharing octahedra and trigonal prism (TP) alternately [27]. Notable examples with the presence of Co in TP are Ca_3CoRhO_6, Ca_3CoMnO_6, $Ca_3Co_2O_6$ etc. Here the in-chain interactions are relatively stronger. $Sr_5Rh_4O_{12}$, although doesn't have a Co ion, is one of the first Ising chain systems in 4d materials with no incomplete 3d electron shell, whose characteristics show similarities and differences with Co- based systems [28]. Magnetism in this compound is due to unpaired electrons in 4d orbitals of Rh^{3+} and Rh^{4+} ions [29]. Kudasov *et al* reviewed experimental data of frustrated Ising chains stacked on triangular lattice with different perpendicular interactions, considering $CsCoCl_3$ (FM nnn), $Ca_3Co_2O_6$ (AFM nn) and $Sr_5Rh_4O_{12}$ (AFM nnn) which belong to different structural families. During the analysis it has been established that due to entropy accumulated in disordered chains there exists a transition to high temperature PDA phase, which is universal for this arrangement [30]. Sr_3HoCrO_6, which belongs to $A_3A'BO_6$ family, is another non-Co material whose magnetic properties are very similar to that of $Ca_3Co_2O_6$. This establishes that the presence of steps in magnetization is not intrinsic to the presence of Co in the Ising chain. In addition this compound exhibits similar unique features found in $Ca_3Co_2O_6$ like giant spins with strong anisotropy and peculiar blend of inter- and intra-chain couplings [31].

$1/3^{rd}$ plateau is also observed in different class of materials with low frustration. α-CoV_2O_6 is an example of such materials where frustration is relaxed due to distorted structure from anisotropic interactions [32]. The magnetic structure consists of FM in-chain interactions with perpendicular AFM bonds. $FeCl_2{\cdot}2H_2O$, $CoBr_2{\cdot}2H_2O$, $CoCl_2{\cdot}2H_2O$ are isomorphous compounds, which have been neglected recently, contain dominant FM chains arranged on two sub-lattice structure. Qualitatively all three materials exhibit similar behavior [17]. Compared to $Ca_3Co_2O_6$ and α-CoV_2O_6 the structure of $CoCl_2{\cdot}2H_2O$ doesn't display any obvious frustration due to its structure [33]. Metamagnetic transitions in these three materials are revealed in figure 1.1. Similar examples of $1/3^{rd}$ plateau have also been found in rare-earth materials EuSe (similar to $Ca_3Co_2O_6$) and CeSb (similar to CoV_2O_6 and $CoCl_2{\cdot}2H_2O$), shown in figure 1.2 [17].

We have focused on triangle based frustrated systems with dominant FM interaction along the chain forming basic magnetic structure. These chains are packed into a 2d lattice in perpendicular plane with weak AFM bonds. In these systems the plateau occurs at $1/3^{rd}$ of the saturation magnetization when the field orients two sub-lattices along its direction while the third sub-lattice lies in the opposite, forming the ferrimagnetic (FiM) phase. The number of plateaus between zero-field and saturated state can depend upon external parameters like time, temperature, pressure etc. Competition between exchange and Zeeman energies decide the field at which the transitions develop in the system.

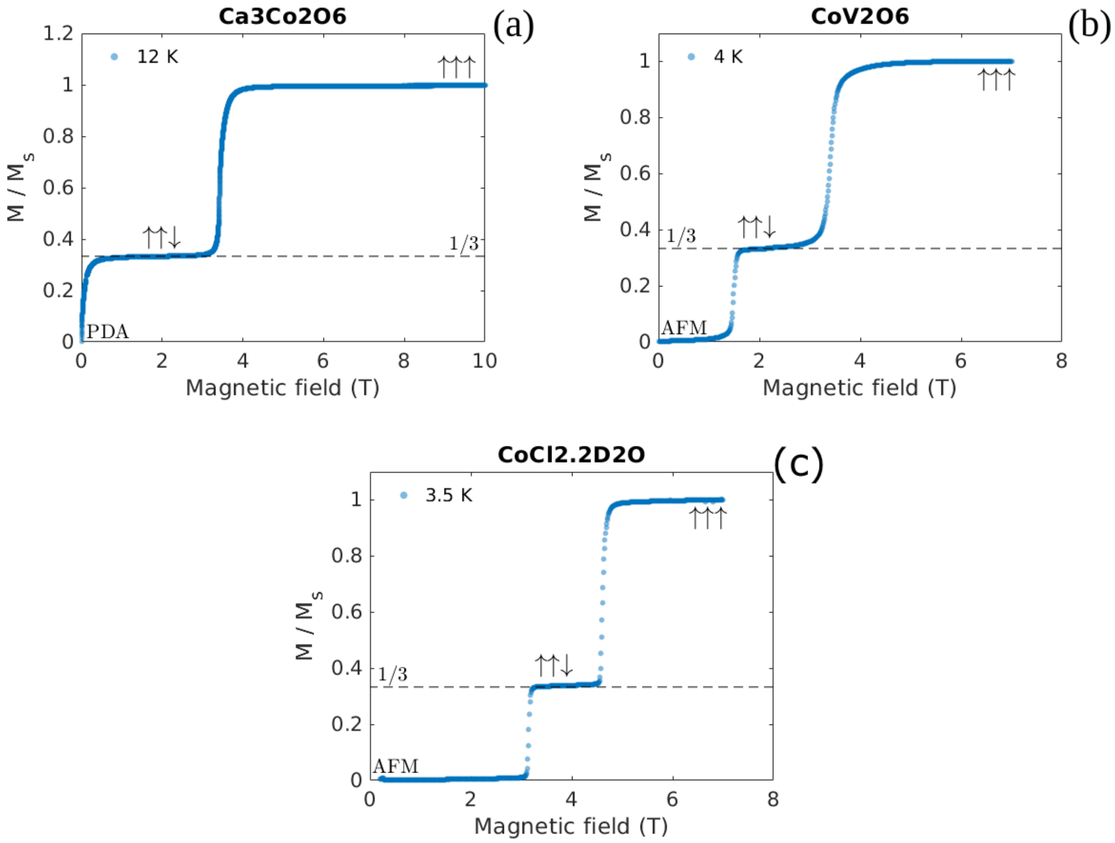

Figure 1.1 – (a) $Ca_3Co_2O_6$, (b) CoV_2O_6 and (c) $CoCl_2 \cdot 2H_2O$ exhibit plateau at $(1/3)^{rd}$ of magnetization at saturation. Despite different origin and behavior at zero-field all three materials display seemingly different ↑↑↓⟷↑↑↑ transition.

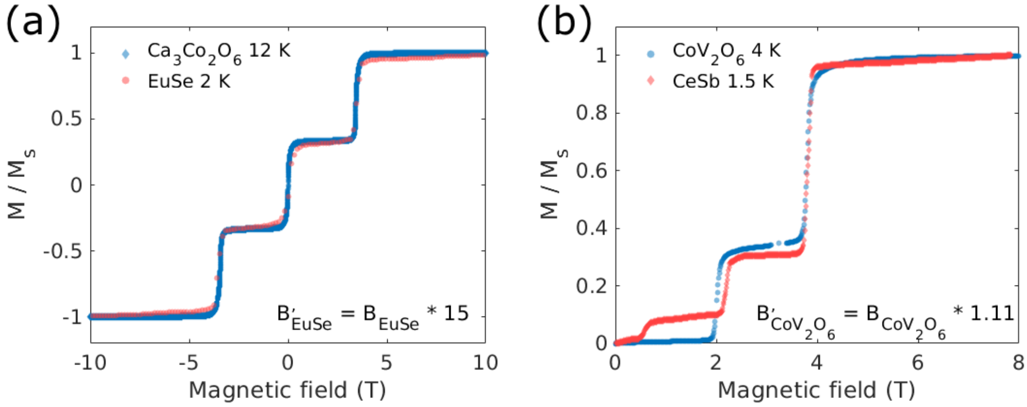

Figure 1.2 – A remarkable collapse of metamagnetic transition between $1/3^{rd}$ plateau and saturation state in materials whose magnetic ions are transition and rare-earth elements. This inspires us to investigate universal aspects of metamagnetic transitions where the phenomena supersedes the inception of magnetic behavior in respective materials. In both figures magnetization is normalized to respective M_s, and magnetic field is scaled.

1.3 Critical Phenomena

Rarely, a physical system has been exactly solved microscopically, except a few known exceptions like hydrogen atom, 2D Ising model, harmonic oscillator etc. On the flip side, it is possible to survey a system from macroscopic standpoint using quantitative theories without involving the complexities of underlying microscopic details [34]. This approach is convenient and practical to study universal behavior in physical systems, for example close to critical point where physical properties exhibit more general and less system specific traits that depend only upon the dimensionality of the system and the symmetry in Hamiltonian [35]. This has been tried in continuous phase transitions where scaling and renormalization techniques have been implemented to study the critical behavior [11].

Scaling can be performed using both scaling laws and data collapse (refer figure 1.4) where different systems are scaled into a single curve and described using scaling laws. When different systems can be scaled with same critical exponents at all length scales, then they are said to be scale invariant and can be assigned to a particular mathematical model called universality class, which represents singular properties of different systems which are alike in the critical region. Eugene Stanley once stated that empirically these universality classes for different critical systems could be assembled into a chart analogous to periodic table [1]. Although studied side-by-side scaling and universality are assumed independently where in many situations only one can hold [35]. At limiting scales, the fluctuations and inhomogeneities of the system are systematically studied in the continuum limit using renormalization.

Modern critical phenomena has been established using all three concepts: scaling, universality and renormalization which form the essential pillars pictured in figure 1.3 [1].

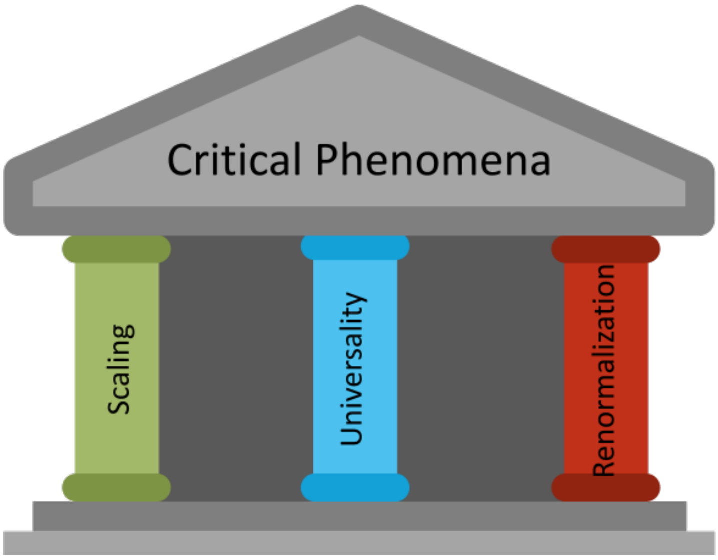

Figure 1.3 – The framework of critical phenomena built using the themes of scaling relations, universality and renormalization.

1.3.1 Universal Behavior in Metamagnetic Transitions

The modern concept of universality using scaling relations in continuous transitions was first introduced by Leo Kadanoff in 1960s. Although no universality is expected in first-order transitions recent theoretical developments attempt to provide a more generalized framework. Previously there have been theoretical investigations to establish universality in systems exhibiting disorder-induced phase transitions. Statistical analysis of magnetic avalanches in these transitions display power law behavior which exhibit universal features resembling equilibrium critical phenomena [36–39]. Another example of seeking universal behavior has been performed theoretically for random first order phase transitions across structural glass transition [40]. An example of scaling for first-order transitions without taking into consideration of renormalization concepts has been theoretically discussed by Fisher and Berker [41].

In our studies we seek to investigate universal aspects of metamagnetic transitions in frustrated Ising chains that display magnetization plateaus. So far most of the research in this domain has been devoted to characterizing and understanding the mechanisms underlying the exact configuration of magnetic moments at metastable plateaus. When multiple configurations produce the same magnetization value at the plateau, questions arise as under which conditions a given configuration is realized. Little attention has been given to the dynamics of phase transition that occur between the plateaus.

A more general question is that how similar are these processes across specific family of materials or all first-order transitions? As discussed earlier, second order transitions show remarkable universality disregarding the microscopic origin of interactions between elements within a system. This has inspired us to look for universal patters in materials that exhibit first-order metamagnetic transitions between the plateaus. We focus our attention to Ising chains in Co oxides where crystal field effects result in strong uniaxial anisotropy. This allows treating magnetic moments in terms of a large g- factor. With higher lying crystal field states not contributing, the magnetic moments can be visualized as effective $S = 1/2$ with a renormalized g-factor at low temperatures. This reduces the number of spin configurations for a given macroscopic state.

On a general note, the theme of universality in critical phenomena has been established on the basis of categorizing different types of critical behavior in separate elements known as universality classes around to the critical region. In our analysis we are investigating similarities in metamagnetic transition away from the critical region at 1/3rd magnetization plateau and saturation region by data collapse, which is a way of establishing scaling. We have chosen $Ca_3Co_2O_6$, CoV_2O_6 and $CoCl_2{\cdot}2H_2O$ for our studies since they exhibit similar features across $\uparrow\uparrow\downarrow\longleftrightarrow\uparrow\uparrow\uparrow$ transition despite different behavior at zero-field (figure 1.1). We aim to understand the process governing these transitions using bulk and microscopic methods.

Figure 1.4 presents establishing similarity from scaling where the order parameter (magnetization M) and the control variable (reduced temperature ϵ) of different materials are 'collapsed'

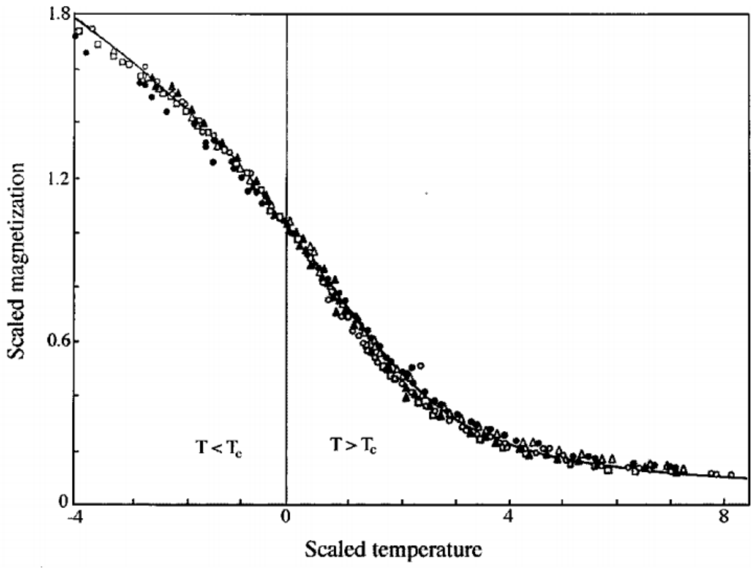

Figure 1.4 – Temperature dependence of reduced magnetization data for five different materials ($CrBr_3$, EuO, Ni, YiG and Pd_3Fe) have been collapsed into a single curve. Not any of these materials are idealized ferromagnet. Despite different individual magnetic properties it has been possible to scale the data using $d = 3$ Heisenberg model. This figure is reused with permission from this article [1]. A metric to quantify data collapse for two thermodynamic parameters from scaling analysis is proposed here [2].

onto a single curve. Prior to scaling, magnetization M has been scaled by dividing with the field H and scaled temperature ϵ is calculated from $\epsilon = \frac{T-T_c}{T_c}$, where T_c is the critical temperature. This curve has a functional form which is calculated for $d = 3$ Heisenberg model.

1.3.2 Supercriticality and Widom lines

Consider the phase diagram (pressure-temperature) of water. The phase boundary between liquid and gas phases also known as coexistence curve ends up with a critical point. Beyond this point the region is supercritical. By textbook definition it is not possible to distinguish between subcritical regions in the supercritical region where both phases possess same symmetry parameters. However, some thermophysical quantities can be extracted from the locus of maximum correlation length which is seen as maxima in response functions separating two subcritical regions. This line is known as Widom line which is seen as a continuation of co-existence curve beyond the critical point.

1.4 Magnetic Relaxation

When magnetic field is applied on a material, the unpaired spins will attain equilibrium after characteristic time τ, known as relaxation time. During relaxation spins exchange energy with other degrees of freedom, often resulting in certain effects like domain wall motion, rotation of magnetic moments etc [42]. Relaxation process provides insight into magnetic structure and spin-lattice interactions in a material [43]. During experiments choosing the right technique is important to determine the range of relaxation times. Experimental frequency range (ν) available for different techniques are shown in figure 1.5.

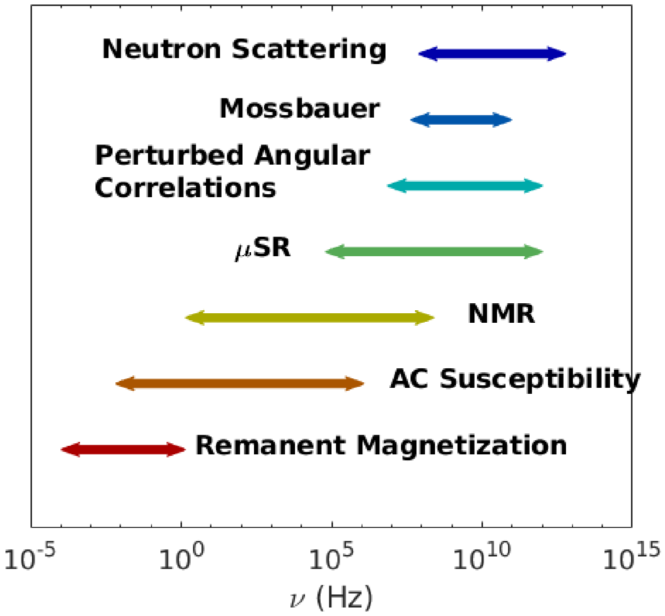

Figure 1.5 – Approximate time-scales of different experimental techniques.

A direct comparison of relative sizes of $\omega(= 2\pi\nu)$ and $1/\tau$ is possible which depends upon the relaxation time of the magnetic moments (τ). This comparison can be classified into characteristic regimes as follows [6]:

1. $\omega \ll 1/\tau$ corresponds to the static equilibrium case where the moments are able to exchange energy with the lattice. This regime is useful when the signal is weak but the dynamics are not important.
2. $\omega \gg 1/\tau$ corresponds to the case when the measurement time window is too quick for the magnetic moments of the system to respond. There will not be enough time for the system to achieve equilibrium and exchange energy with the lattice.
3. $\omega \simeq 1/\tau$ is the transitional regime in which experimental frequency range is comparable to the time scale of the system to react. When the experimental time window is faster or slower than the system a phase lag is created resulting in complex response.

Ideally when choosing an experimental technique to inspect dynamic behavior it is highly recommended that all three characteristic regimes are available.

1.4.1 Slow Dynamics

In classical systems degenerate magnetic moments create a landscape of metastable states which are governed by slow dynamics, whose timescales strongly depend upon external parameters like magnetic field and temperature. Slow dynamics in magnetic nano-particle systems are mainly categorized into two types. The first type is that of non-interacting magnetic moments with significant anisotropy energy barriers which relax individually giving rise to a distribution of relaxation times. In the second type, dense magnetic moments with cooperative effects possess degenerate ground states with no local energy barriers. Attributes of disorder and frustration make them distinct [44]. Usually associated with systems like disordered spin glasses and inherent heterogeneous superparamagnets [45], recently slow dynamics in homogeneous magnetic systems are in considerable attention due to the occurrence of metastable states [46].

Properties of a magnetic nano-particle system can depend upon its size, which was first established from magnetism in single-domain particles. The spins in these particles are in equilibrium with one another and rotate coherently, resulting in the orientation of total magnetic moment to be a relevant degree of freedom. The anisotropy energy (E_a) of these particles can be written as,

$$E_\mathrm{a} = KV\sin^2\theta \tag{1.4}$$

where K is the anisotropy constant, V is the size (or volume) of the particle and θ is the angle between magnetic moment and easy axis. If the size of the particle is lower than $k_\mathrm{B}T$ then the spins can fluctuate like in a paramagnet. To avoid energy cost in domain wall formation, each nano-particle system become single-domain. This assembly of single-domain particles is termed as superparamagnet. The actual magnetic behavior depends upon the measuring time (τ_m) and relaxation time (τ) [47]. This is why the choice of experimental technique is important to study the magnetic relaxation phenomena in these particles. The magnitude of energy barrier and it's dependence on the spin-clusters, domains among others play a vital role in shaping the dynamics of a system [42].

Consider doubly degenerate spin states, a consequence of uniaxial anisotropy, where both spin orientations are equally probable. At finite temperature there exists non-zero probability of spin reversal. The mean relaxation time between spin flips between the two states is temperature-dependent given by Arrhenius law [48],

$$\tau = \tau_0\exp\left(\frac{KV}{k_\mathrm{B}T}\right) \tag{1.5}$$

where τ_0 is the attempt period, which is the average timescale between two consecutive thermal excitations. This law is widely applicable in single domain and superparamagnet particles.

Spin-orbit interaction in materials couple crystal structure with magnetic moments such that energy exchange between these entities happen through phonons and magnons. Since phonon and magnon processes are temperature dependent, spin-lattice relaxation time depends upon temperature. Hence for different magnetic systems relaxation time as a function of temperature can assume different functional forms. In addition to Arrhenius law, relaxation time in different systems are described using Vogel-Fulcher law, critical scaling formula etc [42].

Spin glass behavior is another type of slow relaxation where below certain temperature (freezing temperature T_f) spins encounter random interactions with one another. The spin states below this temperature are irreversible and metastable, which can be characterized by frustration. Above T_f the material behaves like a paramagnet.

Experimentally zero-field-cooled and field-cooled (zfc-fc) magnetization measurements are very useful to identify slow dynamics in materials. At zero net magnetization the moments are at equilibrium. On applying magnetic field (Zeeman energy) the moments are out-of-equilibrium and will attempt to reach equilibrium via relaxation. For isotropic moments no energy barrier is present during spin reversal. The bifurcation of zfc-fc curves occur at the blocking temperature, which is observed as local maximum (blocking temperature T_B) in temperature dependence of magnetization [49].

Slow dynamics can also be visualized from ac susceptibility measurements where Debye-like relaxation is observed in superparamagnets and single-domain particles. This technique is very useful in spin glasses since freezing temperature can't be extracted directly from heat capacity or neutron diffraction [42]. In general one can visualize slow dynamics from ac susceptibility measurements at different frequencies.

Elaborate mathematical analysis of magnetic relaxation phenomena in superparamagnetic systems using phenomenological models is discussed in appendix C.

1.4.2 Energy Barrier: Climbing or Tunneling ?

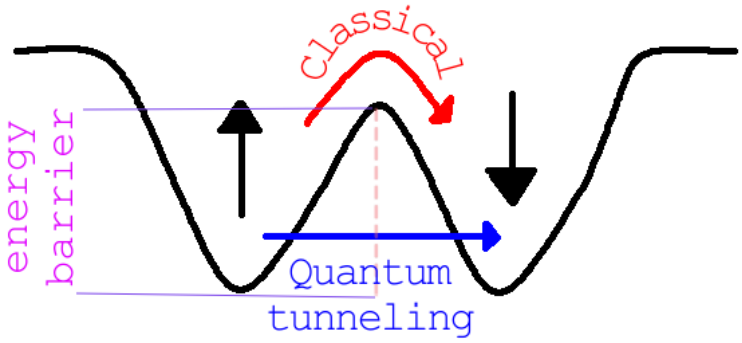

Figure 1.6 – Doubly degenerate spin states. Conventionally spontaneous reversal between the two spin states occur by jumping across the energy barrier. At low temperatures the switching mechanism can happen via quantum tunneling.

The properties of fine particles are understood from their relaxation time, which is known precisely for uniaxial symmetry and approximate forms exist for cubic symmetry [47]. In single-domain particles or superparamagnets due to uniaxial anisotropy at high temperatures the relaxation time can be expressed using equation 1.5. Here the magnetic anisotropy is comparable to thermal energy. In this conventional case the system has to climb the energy barrier to attain magnetization reversal. It is possible to obtain the value of energy barrier and attempt period experimentally.

In case of non-Arrhenius behavior, equation 1.5 can provide physically unfeasible values. For example, fitted attempt period should not be smaller than spin flip time of a single atom (10^{-13} s). Possible factors leading to impractical values are size-distribution and dipole-dipole interaction between the particles [49].

Quantum Tunneling of Magnetization

Macroscopic objects that have two different stable states can be present in only one at a time. Microscopic objects, on the other hand, can be considered as quantum objects and hence it is possible to tunnel and simultaneously exist in both states. At low temperatures magnetization reversal process is dominated by quantum tunneling than conventional Arrhenius behavior. The system exist as superposition of both ↑ and ↓ spin states. Competition between tunnel splitting and interaction between states impacts the probability of tunneling [50].

To understand quantum tunneling of magnetization in detail consider a system with degenerate ground state. Assuming isotropic Heisenberg exchange interaction, for spin S there exists $2S+1$ orientations or macrostates as shown in figure 1.7a. In the absence of anisotropy the energy eigenstates of the system are pure $\mathrm{M_s}$ states. In the presence of anisotropy these states are no longer energy eigenstates (refer figure 1.7b and 1.7c). In a static picture one can state that the eigenstates are superposition of $\mathrm{M_s}$ states on the left and right of the potential energy well. In a dynamic picture one can visualize the system oscillating coherently between the two sides at certain frequency, until the coherence is destroyed. Conventionally for a spin to completely flip to an opposite orientation it has to overcome an energy barrier. This can be achieved from thermal relaxation, or by tunneling. The anisotropy mixes the $\mathrm{M_s}$ levels increasing the possibility of tunneling. This can be clearly seen in figure 1.7, where at zero-field $\mathrm{M_s}$ levels on left and right are in resonance. On applying magnetic field degeneracy between left and right is lifted and resonance is achieved for some values of field.

At crossover temperature (T_c) there is change in the relaxation mechanism. This can be seen in a τ vs $1/T$ plot (refer figure 4 in [52]) where in quantum regime τ remains constant where as in classical regime τ is temperature dependent. Behavior of τ can also change due to presence of defects in the system.

In a nutshell, typically at low temperatures and higher magnetic fields, properties of superparamagnets straddle between two mechanisms, thermal activation and QTM. One fine example

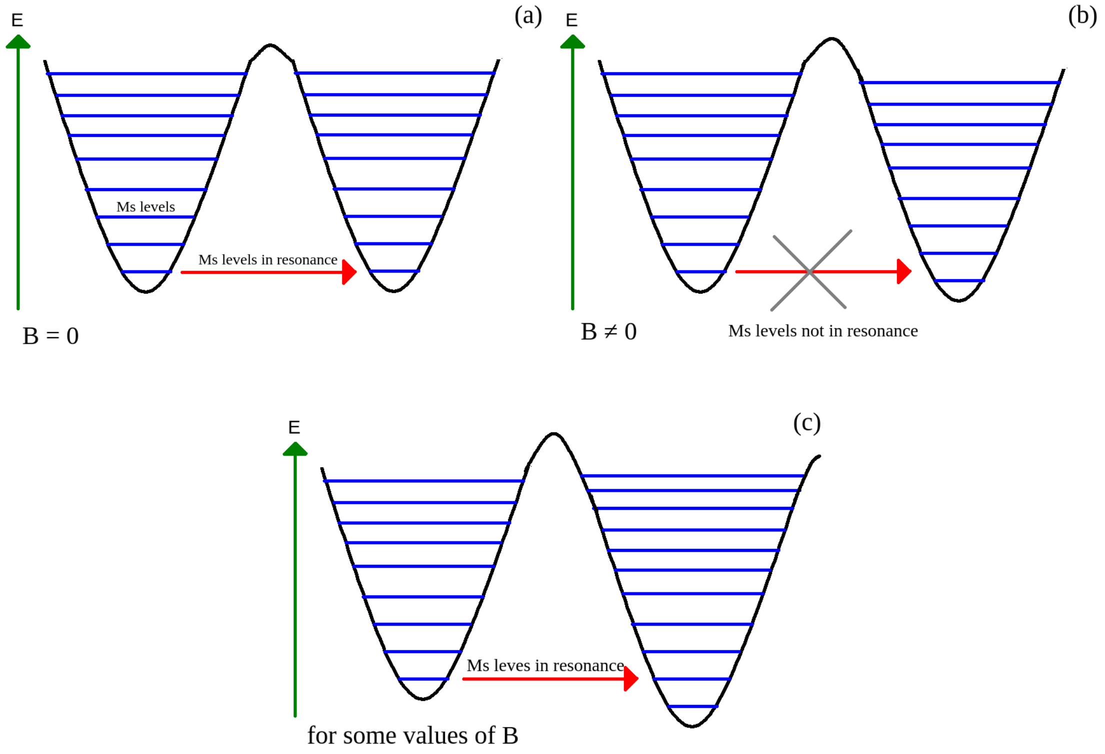
E
(a)
Ms levels
Ms levels in resonance
B = 0
E
(b)
B ≠ 0
Ms levels not in resonance
E
(c)
Ms leves in resonance
for some values of B

Figure 1.7 – A double well picture demonstrating quantum tunneling of magnetization. (a) at zero-field M_s levels on left and right in resonance. (b) at non-zero magnetic field this degeneracy is lifted. (c) for some values of magnetic field M_s levels on left and right are in resonance.

is found in frustrated Ising chains, where the switching of relaxation mechanisms is observed in $Ca_3Co_2O_6$ at zero-field. Around $T \simeq 7$ K there is crossover between temperature dependent Arrhenius behavior and temperature independent QTM [23]. This change of magnetization reversal mechanism is reflected in field-induced magnetization curves, where QTM is believed to be a cause of emergence of multiple plateaus at low temperatures.

2 Samples: Structural and Magnetic Properties

This section is in part extracted from the following publication

- Nagabhushan G. Hegde, Ivana Levatić, Arnaud Magrez, Henrik M. Rønnow, and Ivica Živković, Magnetic dynamics across the in-field transition in $Ca_3Co_2O_6$, Phys. Rev. B **102**, 104418

2.1 $Ca_3Co_2O_6$: Ising Chains on Regular Triangular Lattice

$Ca_3Co_2O_6$ is a well studied but less understood material that has drawn attention due to exotic features like magnetization plateaus [51] and involvement of quantum tunneling processes [52] at low temperatures. However, less emphasis has been given to understand the dynamics of sharp jumps in magnetization between the plateaus which are essentially first-order phase transitions. The magnetization profile shows a complex time and temperature dependence, and hysteresis in the observed plateaus.

$Ca_3Co_2O_6$ crystallizes in $R\bar{3}c$ space group. As shown in figure 2.1 stacked Co^{3+} ions are arranged on a triangular lattice forming chains. However, the adjacent chains are 120 deg out-of-phase with one another resulting in distorted structure. The stacked Co^{3+} ions form a linear chain along *c*- axis which consists face-sharing CoO_6 octahedra and CoO_6 trigonal prisms which alternate throughout the chain. The linear chains are arranged in triangle in *ab*-plane separated by Ca ions.

Magnetic lattice structure is built upon quasi-1d chains along *c*-axis with Ising magnetic moments residing on Co ions [53]. These chains are arranged in a triangular lattice in perpendicular direction (*ab*-plane). Dominant intrachain interactions along *c*-axis are FM in nature with exchange constant $J_1 \simeq 24$ K and inter chain interactions J_2 in *ab*-plane are AFM, which are weaker by an order of magnitude [54]. A relative phase shift of 120^0 results in neighboring chains displaced with one another by $\pm c/3$ and consequently a competition develops between

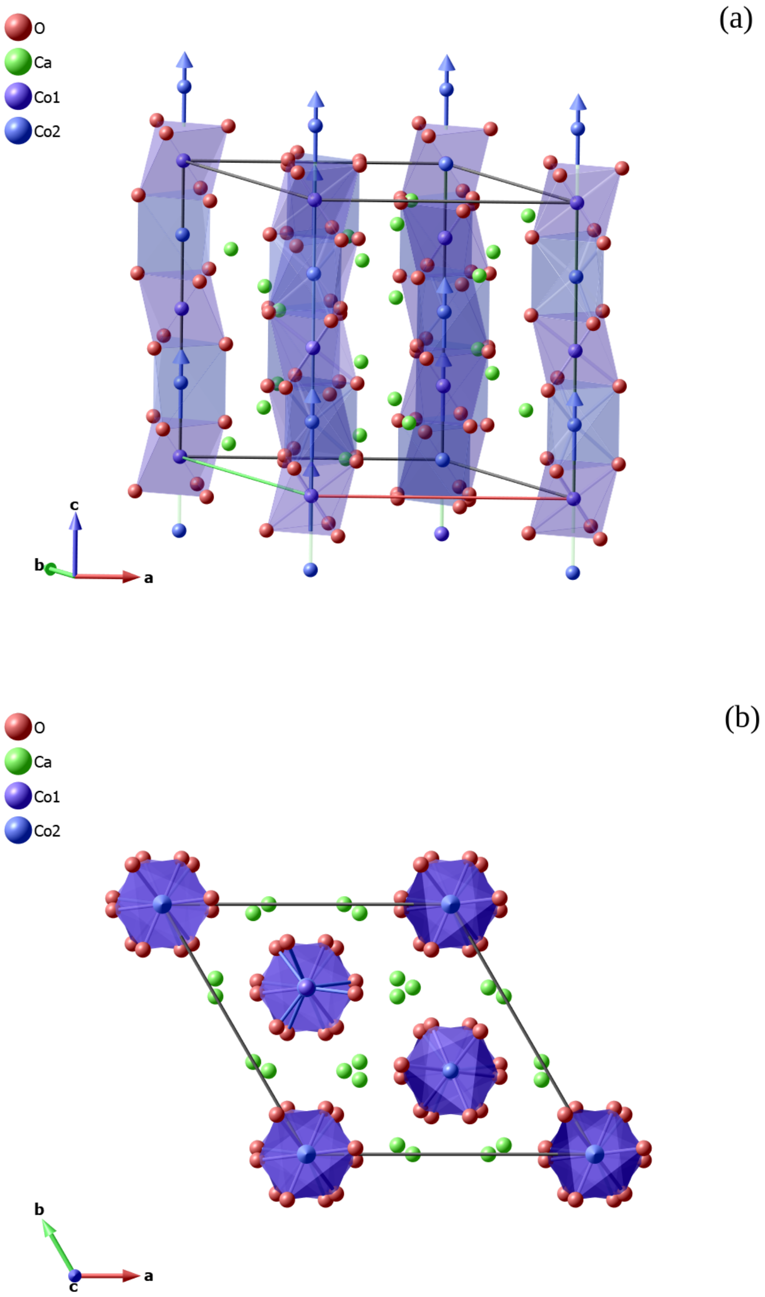

Figure 2.1 – Crystal structure of $Ca_3Co_2O_6$. The structure consists of 1d Ising chains running along *c* axis. In the perpendicular direction these chains are arranged on a triangular lattice in *ab* plane. Non-magnetic Calcium ions occupy the space between chains. Spins are shown pictorially to showcase the easy axis.

J_1 and J_2 influencing the properties of this compound. It has been proven to be incredibly difficult to demonstrate the zero-field magnetic properties of $Ca_3Co_2O_6$.

From neutron diffraction experiments it is evident that below T_N = 25 K an incommensurate, amplitude-modulated spin-density wave (SDW) structure emerges in the system [55]. The periodicity of this SDW structure strongly depends upon field and temperature [56, 57]. On cooling down the system, magnetic Bragg intensities reduce due to the development of short range orders [5, 58, 59]. Below 13 K an additional LRO phase has been identified with wave vector k = (0.5, -0.5, 1) and exceptionally long timescales but demanding only up to 20% of a sample's volume fraction [59]. According to Moyoshi and Motoya [56] the actual modulated structure is of a square-wave type, however, quantum Monte Carlo simulations suggest [60] the formation of a quasi periodic soliton lattice, where the mean separation between solitons determines the periodicity of the observed density wave.

To realize the intricacies of ground state and cause of highly dynamic features the system has to be taken away from zero-field condition. Between 10 K and 15 K field-induced magnetization curves exhibit well defined plateaus at $1/3M_\mathrm{S}$ and at full saturation M_S where the value of M_S = 5.2 μB, is in good agreement with neutron scattering results [56]. There are four steps in total (including -M_S and -$1/3M_\mathrm{S}$) with three transitions between them:

$$\downarrow\downarrow\downarrow\xrightarrow{\mathscr{T}_-}\uparrow\downarrow\downarrow\xrightarrow{\mathscr{T}_0}\uparrow\uparrow\downarrow\xrightarrow{\mathscr{T}_+}\uparrow\uparrow\uparrow \tag{2.1}$$

The $\uparrow\uparrow\downarrow$ and $\uparrow\downarrow\downarrow$ spin configurations constitute average of a large assembly of c-axis chains averaging out the local deviations. From symmetry standpoint, $\mathscr{T}_+$ and $\mathscr{T}_-$ can be considered to be equivalent and hence hereafter we will focus on $\mathscr{T}_0$ and $\mathscr{T}_+$ in upcoming discussions. Looking back at zero-field state, it is exactly in the middle of $\mathscr{T}_0$ transition thereby realizing it is at a particular point in the phase diagram. When magnetic field is ramped from -$1/3M_\mathrm{S}$ plateau across B = 0, it commences a system-wide spin reversal from the $\uparrow\downarrow\downarrow$ to $\uparrow\uparrow\downarrow$ state, where 1 spin out of 3 flips. The exact evolution of this spin reversal has never been thoroughly investigated. It is noticeable that the spin reversal does not occur suddenly, which means that there is a certain broadness associated with the reversal, where we do not see a simultaneous switch of all the spins at once (comparing this to very sharp transitions in single-molecule magnets with avalanche processes occurring during the reversal [61]). Thus, only small segments of each chain undergo spin reversal at a time. Pictorially the $\uparrow\uparrow\downarrow$ state emerges within the $\uparrow\downarrow\downarrow$ state, first as sparsely distributed small droplets which then grow and coalesce as the field is further increased until the system reaches the $1/3M_\mathrm{S}$ plateau. The exactly symmetrical situation occurs on the other side of $\mathscr{T}_0$ when the field is reversed, where small droplets of the $\uparrow\downarrow\downarrow$ state exist and coalesce within an otherwise homogeneous $\uparrow\uparrow\downarrow$ state. This description is equivalent to general concepts applied in first-order phase transitions, where two phases coexist, with latent heat being released or absorbed depending on the direction of the transition process [7].

This illustration agrees with the proposition of magnetic microphases existing in $Ca_3Co_2O_6$ with a finite size distribution [60]. Assuming this premise to be true, the zero-field magnetic state is foreseen to be a highly dynamic ensemble of $\uparrow\downarrow\downarrow$ and $\uparrow\uparrow\downarrow$ states coexisting in all length scales with the exact cluster size distribution of both phases subtly depending upon the exact history path through the field-temperature phase space. The dynamic properties when measured, exhibit complex behavior since both phases contain two spin orientations ($\uparrow$ and $\downarrow$). This results in practical difficulties in differentiating static and dynamic parts or even to mark the boundaries of the phases.

Across $\mathscr{T}_+$ transition segments of $\downarrow$ spins participate in transition dynamics with $\uparrow$ spins in static background. From this viewpoint $\mathscr{T}_+$ transition portrays as simpler version of $\mathscr{T}_0$. This deduction has initiated us to closely inspect temperature, field and frequency dependence of $\mathscr{T}_+$.

2.2 CoV_2O_6: Ising Chains on Distorted Triangular Lattice

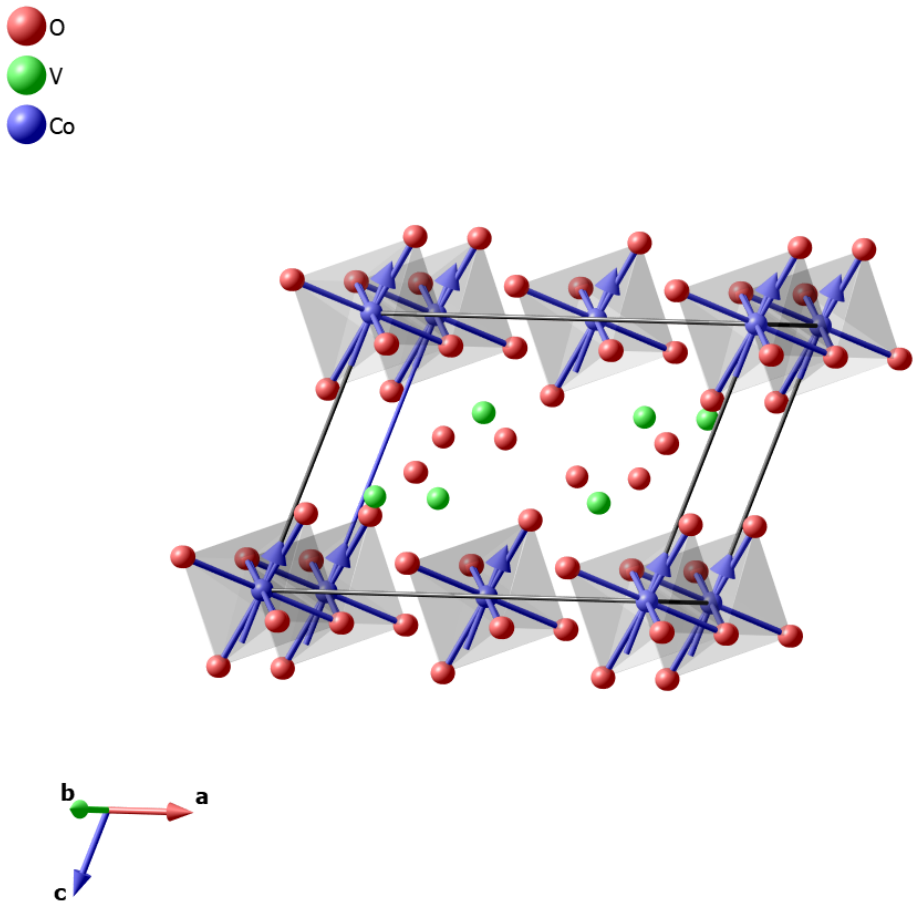

Figure 2.2 – Crystal structure of α-CoV_2O_6. The magnetic ion Co^{2+} forms an octahedra with surrounding O ions. Quasi 1d chains are observed to be along b-direction with ising spins pointing parallel to c-axis.

CoV_2O_6 crystallizes in two polymorphs, monoclinic and triclinic unit cells denominated as α-CoV_2O_6 and γ-CoV_2O_6 respectively. α-CoV_2O_6 possesses only one Co environment, while in γ-CoV_2O_6 there are two Co-environments in a 2:1 ratio. Depending upon how the synthesis is carried out either above 680^0 C or below, α or γ phases can be synthesized respectively.

α-CoV_2O_6 crystallizes in monoclinic structure in space group C 2/m with a = 9.2283(1), b = 3.50167(5), c = 6.5983(1) Å, β = 112.0461(7) deg as shown in figure 2.2. Co^{2+} ions which are magnetic in nature form linear chains containing edge-sharing CoO_6 octahedra and V^{5+} ions which are non-magnetic form zigzag chains with VO_5 square pyramids which share basal edges along b-direction. This results in quasi 1d structure [62]. There are structural differences between α and γ phases. In α phase vanadium chains are connected directly and arranged zigzag in ab-plane. In γ phase vanadium chains are connected through VO_4 polyhedron arranged in zigzag in bc-plane.

Coming back to α-CoV$_2$O$_6$ transverse to the chains in ac-plane the lattice is composed of parallelogram cells. This parallelogram cell can be split into four scalene triangles. The structure in ac-plane is looks like distorted triangular lattice with scalene triangles having non-identical edges as shown in figure 2.3. Anisotropic interchain exchange interactions arise due to anisotropy in structure. Considering 2d ising model in a triangular lattice with anisotropic interactions, this structure can be applied to systematically investigate this magnetic behavior at low temperatures by regarding each single magnetic chain as a rigid spin-chain approximately [32].

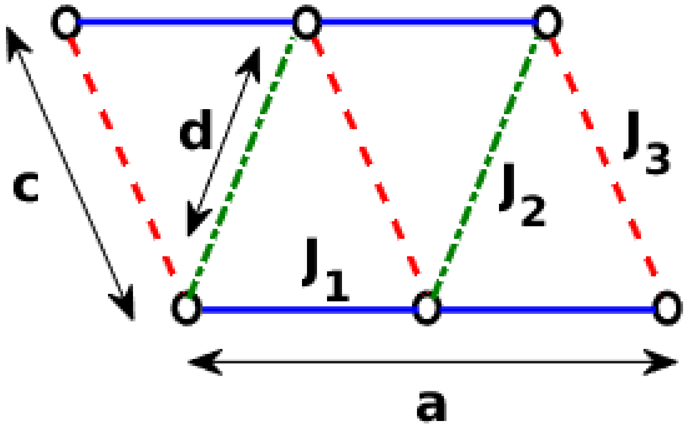

Figure 2.3 – Schematic of parallelogram cell in ac-plane of crystalline α-CoV$_2$O$_6$. Each circle denotes one magnetic chain perpendicular to the plane, and the cell is divided into four scalene triangles with three edges. Each triangle has dimensions of $a/2$, c and d with exchange interactions J_1, J_3 and J_2 respectively.

Strong spin orbit coupling is observed in α-CoV$_2$O$_6$ due to a substantial compression of CoO$_6$ octahedra which have four long and two short Co-O bonds. Zero-field magnetic structure of α-CoV$_2$O$_6$ is AFM with equal numbers of $\uparrow$ and $\downarrow$ chains along b-axis. Every chain is connected to six neighboring chains through Co-O-V-O-Co channel. Four chains at $+a/2$ and $+c$ are antiferromagnetically coupled and two chains at $(+a/2+c)$ are ferromagnetically coupled. These six neighboring chains are arranged in the form of hexagon around each chain and this representation is useful for considering the possible spin order in the 1/3 magnetization plateau phase when moderate non-zero field is applied along easy axis in α-CoV$_2$O$_6$ [63].

Magnetization as a function of temperature reveal AFM ordering at T_N near 15 K. Below 6 K magnetization becomes negligible indicating AFM character [64]. There is large magnetic anisotropy along c-axis. This anisotropy is significant even up to room temperature. Easy axis perpendicular to the chains is unusual. It is believed that competition between AFM interactions between the chains and FM interaction between Co2+ ions within the chain have led to this behavior [64]. In ab-plane adjacent chains are shifted one another by one half of intra chain distance between Co ions forming isosceles triangles. From field-dependent measurements at 5K along a and b axes we observe linear increase in magnetization. On the other hand field-dependent measurements along c-axis display staircase magnetization curve. When measured at 5 K a jump in magnetization is observed around 1.6 T and 3.3 T and saturation is seen around 4 T. $1/3^{rd}$ plateau exists without regular triangles [32] probably due to the unusual competition between interchain AFM and FM on distorted triangular lattice. There is no geometric frustration which is relaxed by anisotropy unlike $Ca_3Co_2O_6$ where different features are observed due to strong frustration. However the height of plateau at $1/3M_s$ remains unchanged. Additional plateaus are observed at lower temperatures with significant hysteresis. Field window between the two transitions decrease on moving away from 5 K suggesting thermally assisted magnetization reversal processes. This thermally assisted character is also evident from strong hysteresis in magnetization loop [64]. Magnetic powder neutron diffraction experiment suggests that $1/3^{rd}$ phase arise from unexpected near equivalence of AFM interchain interaction that results in spin orders typical of a frustrated 2d triangular lattice [63].

In both polymorphs of CoV_2O_6, the cobalt ions are in a 2+ state and they form FM chains separated by non-magnetic vanadium. The long range order sets in at 15 K (α) and 7 K (γ). The 1/3 magnetization step is much more pronounced in α-CoV_2O_6, occurring between 1.5 T and 3.5 T [65], while in γ-CoV_2O_6 it is visible in a narrow field interval near 0.5 T [66]. Magnetic structure of α-CoV_2O_6 in zero field is ferromagnetic along the chains and antiferromagnetic between the chains [64]. Compared to $Ca_3Co_2O_6$, the frustration is relaxed due to the distortion of the triangle and anisotropic exchange interactions [32]. Interestingly, the saturation moment for two polymorphs differs substantially (2.9 μB for γ and 4.5 μB for α), indicating a large orbital contribution in α-CoV_2O_6 [67].

2.3 $CoCl_2{\cdot}2D_2O$: Ising Chains on Two Sub-lattice Structure

$CoCl_2 \cdot 2D_2O$ crystallizes in monoclinic space group C 2/m with unit cell dimensions a = 7.256 Å, b = 8.575 Å, c = 3.554 Å and β = 97.55 deg. Linear chains of Co^{2+} ions are present along *c*-axis with superexchange interaction between them coordinated by four Cl^- ions in *ab*- plane in perfect square planar arrangement and two O^{2-} ions along *b*- axis. These chains are separated by D_2O molecules. The crystal field symmetry at Co^{2+} site is nearly tetragonal and its four fold symmetry axis that coincides with *b*- axis. Base centered structure is formed with identical surroundings of two Co^{2+} sites at (0,0,0) and $(\frac{1}{2},\frac{1}{2},\frac{1}{2})$ per monoclinic unit cell. The crystal structure is shown in figure 2.4.

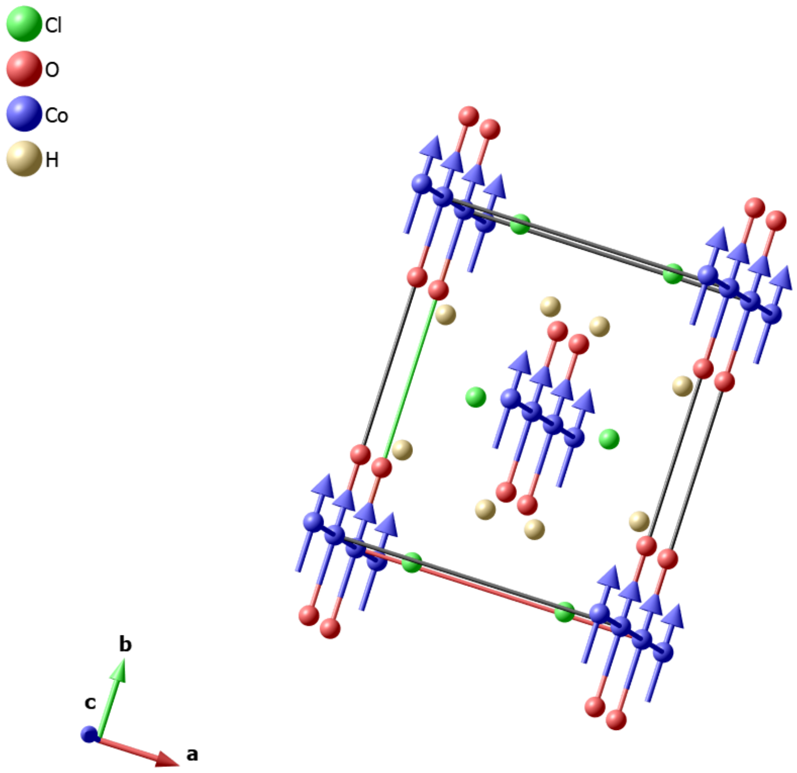

Figure 2.4 – Crystal structure of $CoCl_2 \cdot 2H_2O$. The structure consists of 1d chains along *c* axis. Every Co^{2+} ion is surrounded by two O^{2-} along *b* direction and four Cl^- in *ab* plane. Ising nature of spins is observed parallel to *b* axis which makes it the easy axis.

Temperature scans of magnetization reveal a transition from paramagentic to an ordered antiferromagnetic state at Néel's temperature 17.2 K. At zero field below T_N, linear chains are ferromagnetically ordered, but neighboring chains at (0,0,0) and $(\frac{1}{2},\frac{1}{2},0)$, along *b*- axis are ordered antiferromagnetically [68]. Spins are strongly coupled along the chain indicating one-dimensional character [69] dominated by ferromagnetic interaction. Weaker antiferromagnetic interactions dominate between the chains which tend to make spins in the adjacent chains anti-parallel to one another. The ratio between intra and inter chain couplings are about 0.4 [70].

The ground state of Co^{2+} ion has $L = 3$ and $S = 3/2$. Cl^- and D_2O molecules coordinate and eliminate orbital degeneracy. This leaves L to be non degenerate resulting in strong crystal field. Due to spin-spin coupling, Kramers doublet is formed from four spin states of L which gives rise to an effective spin-1/2 approximation.

Cluster theory reckons for spin waves and spin-cluster excitations with similar set of parameters congruent with paramagentic susceptibility and gives a considerable account of low temperature magnetization curves. This theory predicts that the dynamics of this chain system origins from bound pairs of domain walls [70]. Magnetic resonance experiments suggest that elementary excitations are due to spin clusters. Compared to $Ca_3Co_2O_6$ there is no geometric frustration based on the triangular arrangement of ferromagnetic chains. To the contrary there are 4 nearest neighbors perpendicular to chains coupled with exchange interaction J_1, and 2+2 next-nearest neighbors, coupled with J_2 and J_3, respectively, J_1, J_2, J_3 all being AFM as shown in figure 2.5 [4].

There exists strong anisotropy transverse to the linear chains along *b*- axis resulting in ising like behavior. When large external field is applied along *b*- axis field-dependent magnetization reveal two metamagnetic phase transitions contrary to prevalent spin-flop transitions in usual antiferromagnets. Staircase magnetization is observed from AFM state to FiM state and with further increase in magnetic field there is a subsequent jump from FiM to FM state. This is because the Zeeman energy of a spin becomes comparable to the interchain exchange energies and as a result it becomes energetically favorable for the chains of spins to reorient. Below 9 K, field ramp along easy axis gives rise to AFM to FiM transition at 3.1 T and FiM to FM transition at 4.5 T.

An attempt was made to theoretically study the microscopic dynamics of metamagnetic transitions in $CoCl_2 \cdot 2D_2O$ as early as 1969 [71]. Metamagnetic behavior was investigated from neutron diffraction experiments. What causes the formation of the 1/3 magnetization plateau is the hexagonal arrangement of FM-coupled spins in the ferrimagnetic phase, where the weakest J_3 coupling is left frustrated [33].

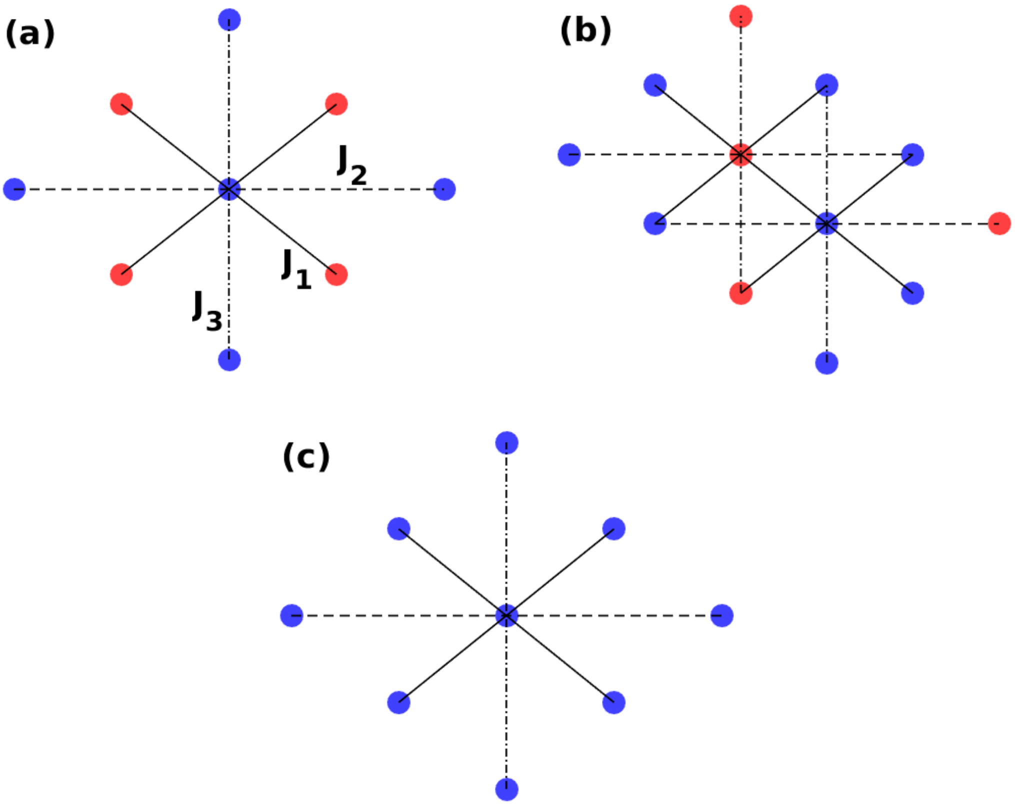

Figure 2.5 – Spin configurations of $CoCl_2 \cdot 2H_2O$. Blue dots indicate ↑ spins and red indicate ↓. (a) AFM (b) FiM and (c) FM spin structures are attained when an external magnetic field is applied parallel to the easy axis. This schematic is cross-section of Ising spin chain coming out-of-plane. J_1 is the nearest neighbor exchange interaction (solid line) where as J_2 (dashed line) and J_3 (dash-dotted line) are next-nearest neighbor interactions. Unlike $Ca_3Co_2O_6$ there is no obvious frustration in spin arrangements [4].

3 Experimental Methods and Instrumentation

3.1 Magnetometry

3.1.1 Magnetization

Magnetization (M) is a vector quantity defined as density of magnetic moments in a sample, which is directly proportional to the rate of variation of free energy with respect to magnetic field (H). Magnetization can be measured in a material as function of external control parameters like temperature, magnetic field etc. Profiles obtained from these measurements provide information on magnetic properties of a material. The experimental time scale of these measurements are relatively slow, which is very useful to study the dynamical aspects of spin-glasses and superparamagnets, often obtained from time-relaxation of magnetization.

Magnetization measurements on our samples were performed using commercial Quantum Design physical property measurement system (PPMS) and Quantum Design magnetic property measurement system (MPMS3). Magnetization measurements in PPMS were carried out in vibrating-sample magnetometer (VSM) mode with the sample cooled from high temperature ($>T_N$) to the desired temperature in zero field followed by fieldscan measurement up to 14 T at sweep rate of 100 Oe/s. On the other hand, in MPMS3 the sample was cooled to desired temperature at 7 T and measurements were conducted in DC mode with field sweep from 7 T down to zero-field.

3.1.2 Susceptibility

Susceptibility (χ) is a response function which is defined as local gradient of magnetization at finite field given by,

$$\chi = \frac{\partial M}{\partial H} \tag{3.1}$$

This quantity is referred as differential susceptibility (or static susceptibility). In ac susceptibility an additional time-dependent excitation field (H_{ac}) is superimposed on static bias field

(H_{dc}) such that,

$$H = H_{\mathrm{dc}} + H_{\mathrm{ac}}\sin(\omega \mathrm{t}) \tag{3.2}$$

where ω is the frequency of ac field. The corresponding magnetization recorded in the presence of oscillating ac field is given by M_{ac}, shown in figure 3.1. Assuming linear response of the system ac susceptibility can be defined as,

$$\chi_{\mathrm{ac}} = \frac{M_{\mathrm{ac}}}{H_{\mathrm{ac}}} \tag{3.3}$$

A typical response of ac susceptibility will comprise of in-phase (real) and out-of-phase (imaginary) parts χ' and χ''. Real component corresponds to the elastic response and imaginary to the dissipation within the system.

This technique serves as a useful tool to probe the collective dynamics in spin clusters than scrutinizing the behavior of a single spin. Hence it is widely used to study domain walls, vortex matter, single-domain particles and superparamagnets, spin-glasses, skyrmions etc. For extensive study of phase transitions and dynamical aspects this technique have proved to be indispensable during experiments. It has been utilized to distinguish different phases, identify the type of phase transition and magnetic ordering, analyze magnetic relaxation, blocking temperatures etc. Several notable examples are discussed here [42].

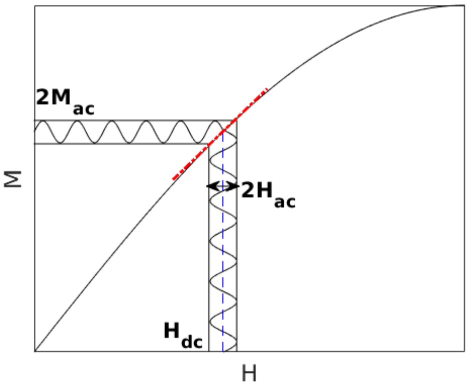

Figure 3.1 – Ac susceptibility demonstrated as gradient of magnetization. The red line is the measure of gradient and blue line is the dc magnetic field applied (H_{dc}). A small excitation field H_{ac}, which is sinusoidal in nature, is superimposed on H_{dc}. Magnetization obtained in the presence of H_{ac} is given by M_{ac}.

3.1.3 Magnetometers

Faraday's Laws of Induction

Induction magnetometers as well as vibrating-sample magnetometers operate on Faraday's laws of induction, in which a changing field induces an electric voltage. The voltage induced will provide information on the magnetic moment of the sample. When magnetic flux enclosed by a resistive coil changes, a voltage is induced across the terminals of the coil. This induced voltage V is given by the rate of variation of magnetic flux ϕ. This can be quantitatively expressed as,

$$\nabla x E = -\frac{\partial B}{\partial t} \tag{3.4}$$

Applying Stokes theorem,

$$\oint E.dl = -\frac{d}{dt}\int B.ds = -\frac{d\phi}{dt} \tag{3.5}$$

For a coil of N turns, the induced voltage is given by,

$$V_{\text{induced}} = -N\frac{d\phi}{dt} \tag{3.6}$$

A typical magnetometer comprises of two distinct set of coils. The primary are used to generate the magnetic field while the pick-up coils to detect the induced signal. In a VSM pick-up coils are connected in opposite polarity to nullify the signal originating from the field to ensure that the signal is measured only from the sample. Whereas in a SQUID magnetometer pickup coils are not counter wound; instead the secondary coils are counter wound with the pickup coils.

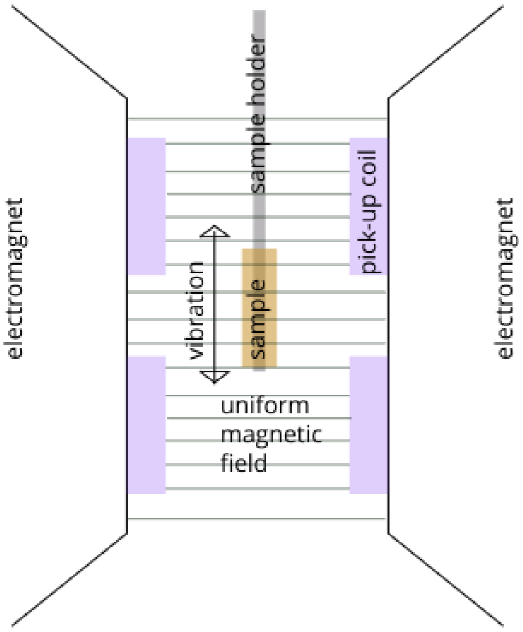

Figure 3.2 – Schematic of VSM. A sample is positioned in the region of uniform magnetic field generated by electromagnets. Using a motor this sample is vibrated and the induced voltage due to change in flux is recorded by the pick-up coils.

Vibrating Sample Magnetometer

In a vibrating sample magnetometer the sample is inserted into the region of uniform magnetic field in the center. Then it is sinusoidally vibrated using a motor. When the sample is vibrated the flux of the sample through the coils change, thereby inducing a voltage. In a dc measurement the sample is physically translated through the pick-up coil using a motor to achieve change in magnetic flux.

Ac Susceptometer

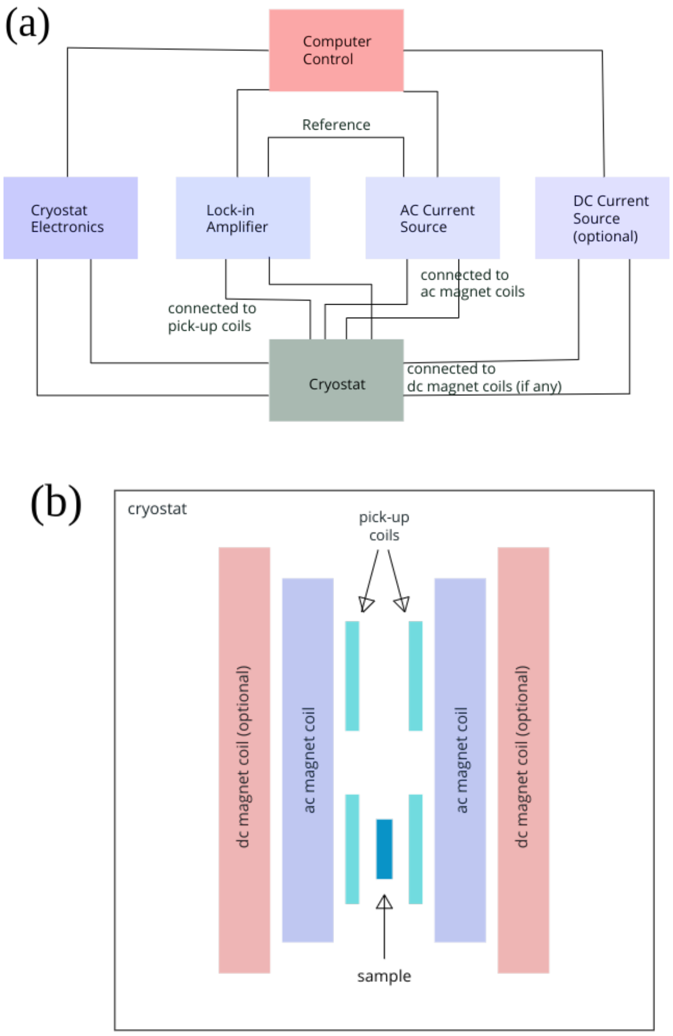
(a)
Computer Control
Reference
Cryostat Electronics
Lock-in Amplifier
AC Current Source
DC Current Source (optional)
connected to ac magnet coils
connected to pick-up coils
Cryostat
connected to dc magnet coils (if any)
(b)
cryostat
pick-up coils
dc magnet coil (optional)
ac magnet coil
ac magnet coil
dc magnet coil (optional)
sample

Figure 3.3 – Schematic of ac susceptometer is shown in (a). Either ac current or voltage source is used to generate ac field. Lock-in amplifiers are used to eliminate noise and extract signal obtained from the pick-up coils. A schematic of cryostat containing ac, dc (optional) and pick-up coils is shown in (b). The sample under study is positioned in the region between a pair of pick-up coils.

Unlike dc measurements where the sample is physically translated through the pick-up coil to achieve change in magnetic flux, ac measurements generate a changing flux from oscillating magnetic field which yields a time dependent response in the sample at rest.

An ac susceptometer contains two distinct set of coils. The primary coils generate ac field also known as excitation field. The secondary coils are a pair of oppositely pick-up (detection) coils connected in opposite polarity measure the signal from the sample. Optional dc coils are sometimes used to generate dc magnetic field which are often referred as bias field.

Taking reference from an ac voltage or current source, lock-in amplifier is used to measure the induced signal allowing real and imaginary components to be detected. Using additional lock-in amplifiers one can measure higher order susceptibilities.

Superconducting quantum interference device (SQUID)

SQUID is formed by when two superconductors are set apart using thin insulating layers which are Josephson junctions. The two parallel junctions allow tunneling of Cooper pairs. SQUID can measure change in magnetic field down to a sensitivity of $< 10^{-14}$ T. Compared to other techniques SQUID is the most sensitive magnetometer which can be used for high resolution magnetization measurements.

A SQUID base measuring instrument contains a superconducting flux transformer which comprises of an input coil and a pick-up loop. A current is generated when the magnetic flux through the pick-up loop changes. This is to ensure flux quantization in superconducting rings. The schematic of superconducting pick-up loop is shown in figure 3.4.

Unlike induction magnetometers in a SQUID magnetometer, when the sample is translated through the superconducting pick-up loop an output voltage is generated as a function of sample position in the form of a flux profile. Induced moment of the sample is deduced by fitting the measured profile to the expected for a point dipole. This flux profile is measured at every temperature and magnetic field.

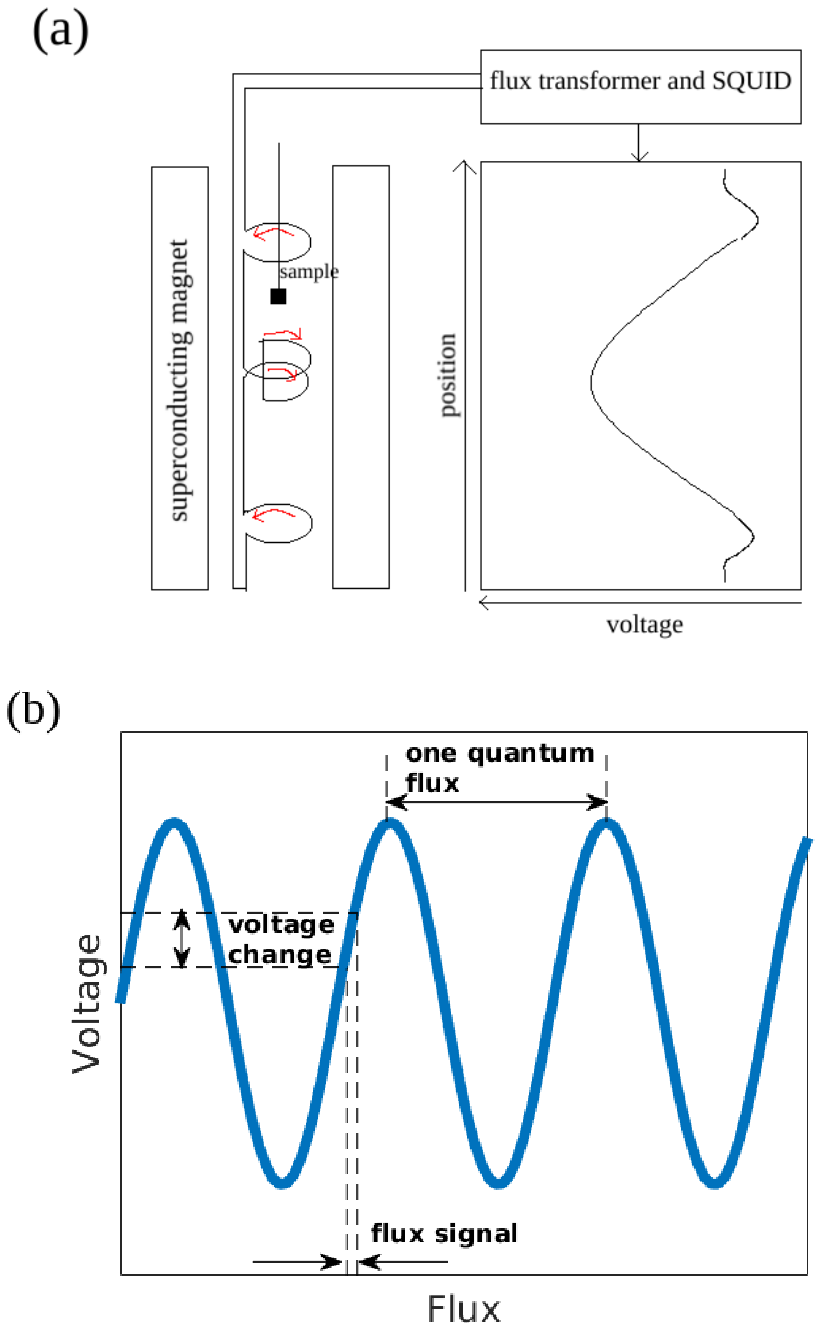
(a)
flux transformer and SQUID
superconducting magnet
sample
position
voltage
(b)
one quantum flux
voltage change
flux signal
Voltage
Flux

Figure 3.4 – Schematic of superconducting pick-up loop in a SQUID is shown in (a). The pick-up and secondary coils are counter wound. (b) Change in flux giving rise to a response in voltage. The periodicity of voltage is one quantum flux.

3.2 Heat capacity

Specific heat measurements in solids provide information on lattice, electronic and magnetic properties of materials. At temperatures sufficiently below Debye temperature it can probe electronic and magnetic energy levels of a material facilitating comparisons between experiment and theory. Total specific heat of a substance is the sum of contributions from lattice, electronic and magnetic specific heat.

$$C_{\text{total}} = C_{\text{lattice}} + C_{\text{electronic}} + C_{\text{magnetic}} \tag{3.7}$$

Experimentally it is easier to measure specific heat under constant pressure conditions. This is expressed as,

$$C_p = \left(\frac{dQ}{dT}\right)_p \tag{3.8}$$

During the measurements a known amount of heat is supplied to the system and the resulting change in temperature is monitored, thereby calculating the specific heat. The sample is fixed to a platform using grease, which is connected to heat source and thermometer.

Simple Model

Elementary study of raw data can be performed using simple model, which assumes good thermal contact between sample and sample platform such that both are in thermal equilibrium throughout the measurement. Total specific heat of the sample and sample platform can

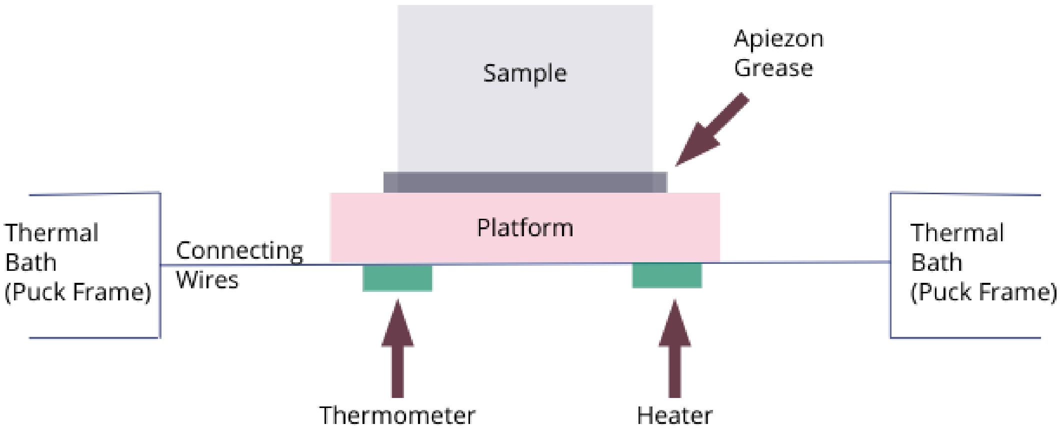

Figure 3.5 – Schematic of thermal connections to sample and platform in specific heat option. Apiezon grease facilitates thermal connection between the sample and platform. A thermometer and heater are placed on the undersurface suspended by platinum wires which are connected to the surrounding thermal bath. Heat capacity measurements were carried out in Quantum Design PPMS HC module.

be extracted using the following equation,

$$C_{\text{total}}\frac{dT}{dt} = -K_{\text{w}}(T - T_b) + P(t) \tag{3.9}$$

where K_{w} is the thermal conductance of the platinum wires, T_{b} thermal bath temperature and $P(t)$ power applied by the heater. During the heating cycle, power $P(t)$ is equal to P_0 and during the cooling cycle, power is zero. This equation can be solved by assuming exponential functions and the characteristic time τ is equal to C_{total}/K.

This model can be used to measure the addenda and most samples. However, more sophisticated two-tau model is implemented when the thermal contact between the sample and platform is poor.

Two-tau Method

Poor thermal conductivity between sample and platform can produce a temperature gradient. The flow of heat between platform and sample as well as platform and puck are simulated using two-tau method. The equations for two-tau models is given below:

$$\begin{aligned} C_{\text{platform}}\frac{dT_{\text{p}}}{dt} &= P(t) - K_{\text{w}}(T_{\text{p}}(t) - T_{\text{b}}) + K_{\text{g}}(T_{\text{s}}(t) - T_{\text{p}}(t)) \\ C_{\text{sample}}\frac{dT_{\text{s}}}{dt} &= -K_{\text{g}}(T_{\text{s}}(t) - T_{\text{p}}(t)) \end{aligned} \tag{3.10}$$

where C_{platform} and C_{sample} are corresponding heat capacity of platform and sample. K_{g} is the thermal conductance between the platform and sample due to apiezon grease, with T_{p} and T_{s} being respective temperatures.

Equivalent Debye Temperature

The sample heat capacity of the material under study can be expressed in terms of equivalent Debye temperature. The lattice heat capacity can be expressed from the following equation,

$$C_{\text{v}} = 3rNk\int_0^{\infty}\left(\frac{h\nu}{2kT}\right)^2 \operatorname{csch}^2\left(\frac{h\nu}{2kT}\right)g(\nu)d\nu \tag{3.11}$$

where r corresponds to number of atoms in a molecule and N to the total number of molecules. The density of phonon modes in the range of frequency between ν and $\nu + d\nu$ is given by $g(\nu)d\nu$. The expression for $g(\nu)$ stands as long as we assume that the propagation of phonons in the crystal lattice is controlled by the similar dispersion relation as linear waves in a continuous isotropic solid. In real solids there exists a threshold frequency ν_{D} above which the mode density function is zero.

$$
\begin{aligned}
g(\nu) &= \frac{3\nu^2}{\nu_{\mathrm{D}}^3}, \nu \leq \nu_{\mathrm{D}} \\
g(\nu) &= 0, \nu > \nu_{\mathrm{D}}
\end{aligned}
\tag{3.12}
$$

ν_{D} in physical terms is the least count of the phonon wavelength that can propagate in a lattice with discrete spacing. Debye temperature is then defined as,

$$h\nu_{\mathrm{D}} = k_{\mathrm{B}}\theta \tag{3.13}$$

Heat capacity can be re-expressed in terms of Debye temperature,

$$C_{\mathrm{v}} = 9rNk(\frac{T}{\theta})^3 \int_0^{\theta/T} \frac{x^4 e^x dx}{(e^x - 1)^2} \tag{3.14}$$

At high temperature,

$$C_{\mathrm{v}} \to 3rNk \tag{3.15}$$

At sufficiently low temperature, heat capacity is familiar with T^3 law

$$C_{\mathrm{v}} \to \frac{12}{5} rNk\pi^4 \left(\frac{T}{\theta}\right)^3 \tag{3.16}$$

θ can be solved numerically but it assumes only the lattice contribution.

3.3 Neutron Experiments

Neutron experiments are useful tools in finding details on the size of particles and local ordering in complicated structures. They provide understanding of spin correlations and fluctuations within a sample. In a neutron diffraction experiment the energies of diffracted neutrons are integrated. This translates to measuring the Fourier transform of instantaneous spatial correlations within the sample. This experiment can be performed at wide range of angles and the size of particles are calculated from the broadened Bragg peaks. Detailed information on the structre can be extracted from measurements at small angles using SANS technique. On the other hand in an inelastic neutron scattering experiment Fourier transform of time-dependent correlations are measured from analyzing energy at the neutron cross section [47].

Experiments using neutrons are expensive but they provide inherent advantages over x-ray counterparts for multiple reasons. Neutrons can penetrate deeper inside materials and measurements are non-destructive while x-ray measurements can cause fatal damage to some samples from radiation. The source of scattering in neutrons correspond to scattering length density, which varies in a random fashion throughout the periodic table as well as within same elements between different isotopes. Scattering in x-rays is proportional to electronic density and hence lighter elements go undetected. Another advantage of using neutrons is that due to non-zero magnetic moment of neutrons, in ordered magnetic lattices magnetic neutron scattering is possible from unpaired electrons. The differential scattering cross section from magnetic scattering is expressed as,

$$\frac{d\sigma}{d\Omega}(q) = \frac{D_{\mathrm{M}}^2}{N}|\mu_0 M_{\perp}^2(q)| \tag{3.17}$$

where $M_{\perp}$ is the component of magnetization transverse to q.

In general during a neutron scattering experiment change in wave-vector and change in energy before and after scattering can be expressed as, $q = k_{\mathrm{i}} - k_{\mathrm{f}}$ and $\hbar\omega = E_{\mathrm{i}} - E_{\mathrm{f}}$. During the measurement the detector measures the number of neutrons as a function of ω and q. Intensity of scattering as a function of q can reveal correlations in space, while intensity of scattering as a function of ω can provide information on correlations in time. The scattered beam intensity is proportional to the square of structure factor. The scattering length (b) of an isotope depends upon many factors like initial energy state, incident neutron energy, energy exchange and spin interactions between neutrons and nucleus, nuclear resonance states. This leads to scattering and absorption, corresponding to real and imaginary component of b respectively. A neutron scattering length consists of,

$$b = b_{\mathrm{p}} + b_{\mathrm{s}} \tag{3.18}$$

where b_{p} is the probabilistic interaction of neutron with a nuclear potential and b_{s} is the interaction with nuclear spin. In SANS experiment the real part of b_{p} is crucial since it induces elastic coherent scattering. When it is impossible to resolve individual atoms, scattering length density ρ is used instead of discrete atomic scattering length b.

3.3.1 Magnetic Small Angle Neutron Scattering

Magnetic small angle neutron scattering (Magnetic SANS) is an useful technique for microstructure determination in both coherent and incoherent structures. Information complementary to other real space and surface sensitive techniques can be obtained. Typical length scale that can be probed varies from 1 nm to 300 nm, thereby providing an inherent and unique advantage to use this method. The superiority of SANS over other techniques is visible when it can be performed under adaptable environments like temperature, magnetic field etc.

A general description of SANS process can be obtained from scattering theory. According to

Bragg's law, diffraction from a structure at small angles has large lattice spacing,

$$d = \frac{\lambda}{2\,\sin(\theta)} \tag{3.19}$$

where θ is the angle of diffraction, d is the lattice spacing. SANS technique can be used to obtain diffraction pattern at small angles thereby one can obtain information on large structures.

A typical SANS setup is performed under two scattering geometries, with external magnetic field applied either parallel or perpendicular to the neutron beam. The source of neutron beam is either a reactor or a spallation source. The wavelength band of the incoming neutron beam is selected using a velocity selector or chopper. The neutrons are sent through a collimation chamber to control the angular divergence of the beam that comes out of the chopper. The typical size of sample which can be irradiated is approximately 1 cm^2.

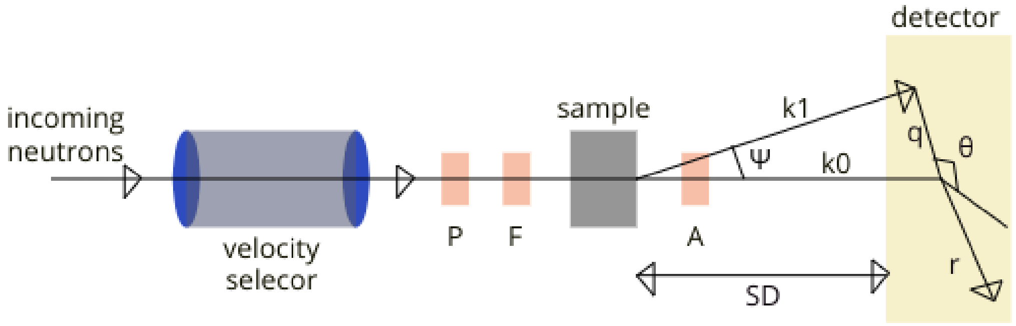

Figure 3.6 – Schematic of SANS experimental setup. Using a velocity selector or chopper incident neutrons of a band of wavelengths are filtered out. Devices like polarizer (P), spin-flipper (F) and analyzer (A) are optionally used in the setup. The sample is placed between velocity selector and detector. Neutrons (of wave vector $k0$) are incident of the sample and scattered neutrons $k1$ are detected on the detector. q is the scattering vector, which depend on neutron wavelength λ and scattering angle ψ. SD is the distance between sample and detector. On the detector image angular anisotropy is given by θ, and r is the radial distance from the beam center.

In a SANS experiment the sample whose excitations are to be probed is placed in between a cold neutron beam and a detector. The scattered neutrons are recorded by a 2D position-sensitive detector placed at a distance $\simeq$ 1-40 m from the sample. The data acquisition is performed for time scales ranging from a few minutes to hours. Several corrections are performed on the recorded neutron beam related to detector dead time, dark current and efficiency. Planar geometry of the sample is corrected using solid-angle correction. Optional optical devices like polarizer, spin-flipper, or analyzer can be used. Spin analyzer will be useful to distinguish neutron spin state before and after interacting with the sample. To maintain polarization between polarizer and spin filter magnetic guide fields are installed. Schematic of

SANS is shown in figure 3.6. The binned data contains information on differential cross section $\frac{d\Sigma}{d\Omega}$ of the sample in absolute units as a function of magnitude and direction of scattering vector q.

3.3.2 Sample Preparation

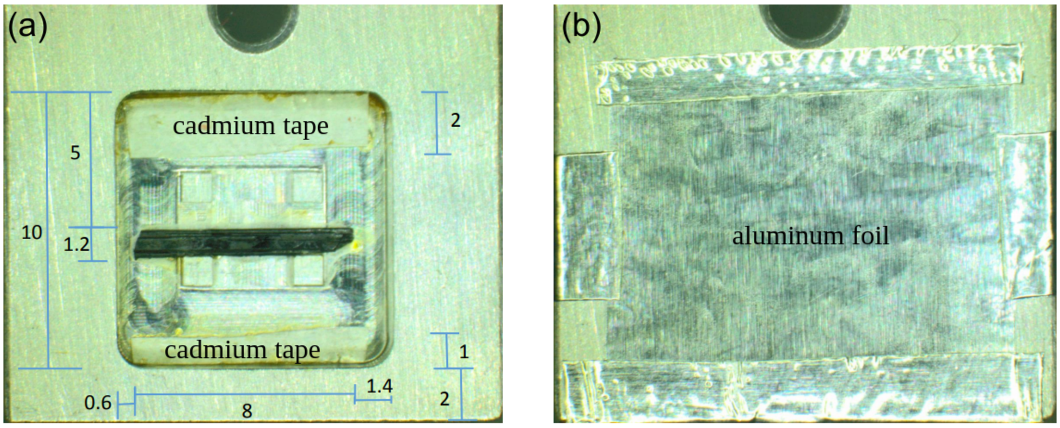

Figure 3.7 – Sample holder for SANS experiment. (a) Sample is glued horizontally in the middle of the holder. (b) Aluminum foil wrapped to on the whole plate

The sample holder for SANS experiment was prepared as shown in figure 3.7. A single crystal of mass 15 mg was glued with the right alignment in the middle, with the smallest quantity of varnish that could be used. Cadmium tape was used on top and bottom of the plate to facilitate spotting the sample area. Aluminum foil was wrapped on the whole plate to prevent loosing the crystal if it gets unglued. Horizontal alignment of the sample was to ensure that magnetic field is parallel to c- axis of the sample (the direction of Ising magnetic moments) since a horizontal magnet was used during the experiment.

3.4 X-ray Experiments

Since X-rays are electromagnetic radiations they can be used to study magnetism by studying the magnetization density in structures. When the incident photon energy is comparable to binding energy of the magnetic ion resonance enhancement is observed in scattered intensities. Although magnetic scattering cross section for x-rays is smaller than neutrons it is possible to obtain against the background of charge scattering from interference between the two [72]. Hence, to enhance the information from magnetic information in x-ray experiments advanced beamline setups with specific polarization characteristics are necessary [73].

In general, magnetic scattering of x-rays can be used to study long wavelength modulated structures, identify differences between orbital and spin magnetization density, coherence between charge and magnetic scattering etc. Resonance is observed when moments of outer electrons exchange-split the core electron levels, which is energetically favorable. This is observed as anomalous dispersion in reciprocal space with additional magnetic peaks [72].

Usually x-ray reflections are observed only when identical atoms occupy equivalent sites. In case of defects, impurities etc if equivalent sites are different then it can give rise to forbidden reflections which are enunciated in resonant scattering symmetry properties of electronic and magnetic structure are affected by virtual excitations [74].

3.4.1 Coherent Soft X-ray Scattering

When a wave is able to interfere with itself, this property is known as coherence. Based on this ability phase relationships can be established between two points in the same wave front and successive wave fronts which are known as spatially and temporal coherence respectively. Coherent x-rays of longer wavelength, often termed as soft x-rays serve as useful tool to study magnetic orders due to higher critical angle of total reflection, weak penetration and resonance with L_2 (low energy) and L_3 (high energy) edges in 3d transition metals [75]. These characteristics can be utilized to interpret dynamic phenomena in phase transitions, grain boundaries, transport etc in magnetically ordered materials [76].

In incoherent x-ray scattering continuous diffraction pattern is observed which only depends upon the wavelength (λ) and distance between object and detector (d). On the other hand coherent scattering produces speckled diffraction pattern which can be used to reconstruct the structure of object since the pattern depends on one additional parameter, size of illuminated area (a) [77].

A coherent x-ray beam on scattering from an object will enable interference effects such that phase difference between wave points at different parts of the object will result in phase contrast. These interference patters are often referred as speckles and provide information on shape and internal structure of the object under study [77]. Since x-rays probe structure in Fourier space, the real space image of the object is then recovered from phase retrieval algorithm iterated at least few hundred times to obtain exact phase information [76, 78].

3.4.2 Sample Preparation using Focused Ion Beam

$Ca_3Co_2O_6$ sample for the experiment was prepared using focused ion beam technique. Focused ion beam (or simply FIB) is similar to scanning electron microscope where instead of electrons a finely assembled ion beam (usually Ga) is incident on sample surface such that a small quantity of material sputters and exits in the form of neutral atoms or secondary ions which are collected in form of image. FIB is operated at low currents for imaging and at high currents for milling or sputtering.

$Ca_3Co_2O_6$ lamellas were FIB'ed for two different orientations as shown in figure 3.8. Holes were milled into gold-coated substrate, and lamellas were transferred onto them. Final cleaning step was carried out in O_2 plasma cleaner.

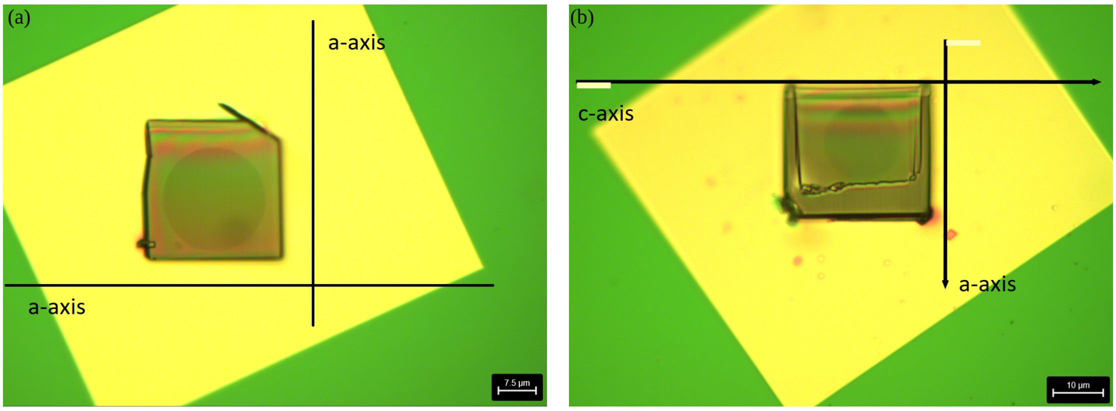
(a)
a-axis
a-axis
7.5 µm
(b)
c-axis
a-axis
10 µm

Figure 3.8 – Prethinned samples of $Ca_3Co_2O_6$ were prepared using focused ion beam in two different orientations for measurements in reflection and transmission mode.

4 Similarity Prospects for Staircase Magnetization

This chapter is in part extracted from the following publication

- Nagabhushan G. Hegde, Ivana Levatić, Arnaud Magrez, Henrik M. Rønnow, and Ivica Živković, Magnetic dynamics across the in-field transition in $Ca_3Co_2O_6$, Phys. Rev. B **102**, 104418

4.1 Inspection of Field-induced Magnetization across $\uparrow\uparrow\downarrow \longleftrightarrow \uparrow\uparrow\uparrow$ Transition

4.1.1 Case 1: $Ca_3Co_2O_6$

Field-induced magnetization data is presented in figure 4.1. Around 10 K $Ca_3Co_2O_6$ exhibits clear-cut plateaus at $1/3^{rd}$ of saturation magnetization and the $\mathscr{T}_+$ transition exhibits sharp jump. With increase in temperature towards T_N the plateaus get smeared out and $\mathscr{T}_+$ becomes broader with less sharp jump in magnetization.

At temperatures around 20 K, a kink is observed within the transition. This kink is simply an alteration of curvature in magnetization observed at lower temperatures. The mechanism of this transformation is yet to be understood. Lowering temperature below 10 K will incite hysteretic effects, and additional plateaus are seen. Strong temperature and time dependence in magnetization curves is also observed at these temperatures. Here we focus our attention for $T > 10$ K to avoid the issues of hysteresis and strong time and temperature dependence.

Fieldscan profiles were inspected at individual temperatures to understand how thermal fluctuations affect spin flip experimentally. The temperature range was selected in a way such that at minimum temperature no hysteresis is observed and at higher temperatures some spins flip up and down due to thermal agitation. One can notice that in the individual fieldscans at higher fields ($B >> B_c$, where B_c is the transition field) all the moments have

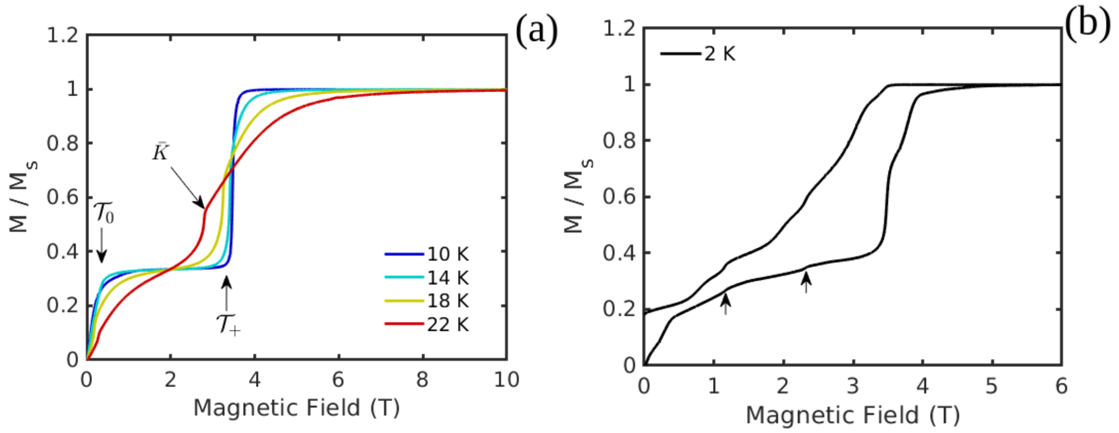

Figure 4.1 – Field-induced magnetization profile of $Ca_3Co_2O_6$ for $T \geq 10$ K. Metamagnetic transitions $\mathscr{T}_0$ and $\mathscr{T}_+$, and kink ($\bar{K}$) developed at high temperatures are denoted using arrows. Magnetization fieldscan at $T = 2$ K with significant hysteretic effects. Additional steps are highlighted with arrows.

occupied ↑↑↑ state. On lowering the field ($B < B_c$) a system wide spin reversal is initiated to achieve ↑↑↓ state, where on an average one spin out of three changes its orientation. The ↑↑↑ and ↑↑↓ configurations represent an average of large assembly along c-axis such that the local deviations averaged out. This mechanism of spin reversal between ↑↑↑ and ↑↑↓ states also applies to other two samples where these initial and final configurations are preserved across this transition despite different internal mechanisms being involved during spin flip.

Pictorially this spin flip with field can be visualized as shown in figure 4.2, where at large fields all spins are polarized (This state is realized for any material where at sufficiently large fields, moments attain saturation). On decreasing the field a single spin flip occurs. Since $B >> B_c$ is very ordered state, this single spin flip relative to uniformly polarized background of all ↑ spins

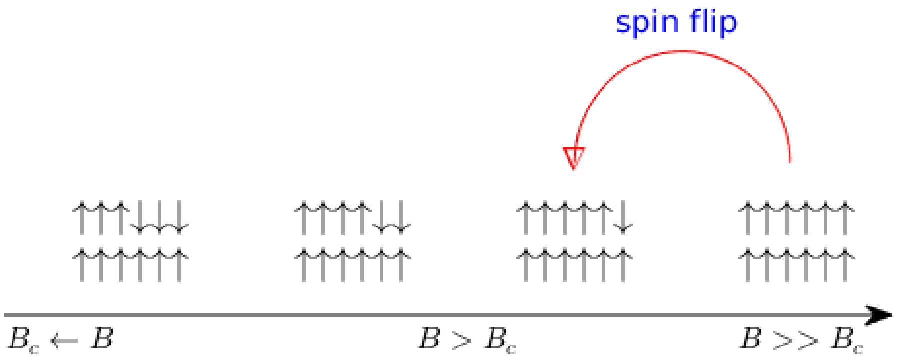

Figure 4.2 – A cluster spins completely polarized at higher magnetic fields ($B >> B_c$). On decreasing the field an excitation occurs, followed by consecutive spin flips on further decreasing the field approaching B_c.

can be considered an excitation. Further decrease in the field approaching B_c results in more spin flips. This observation is analogous to high-temperature Curie behavior in paramagnets. In any material despite the nature of ordered state, at high temperatures in paramagnetic state the spins are highly disordered with net moment close to zero. Curie behavior in PMs is observed as straight line in $1/\chi$ vs T plot. In this state when a small magnetic field is applied, something similar to an excitation is created out of the total magnetization (which is zero) resulting in a small non-zero moment. At this non-zero magnetic field, decrease in temperature approaching T_c (ordering temperature) will result in spins becoming more and more polarized.

Hence, when analyzing magnetization profiles at higher field one can make an analogy with high temperature Curie behavior ($T > T_\mathrm{c}$) in classical renormalization approach [11], to polarized spin state at higher field ($B > B_\mathrm{c}$) with high-field magnetization fieldscan profiles incorporating same shape. This universal observation has already been briefly shown in figures 1.1 and 1.2. A detailed qualitative comparison is performed in section 4.2.

It makes a case for us to compare how all three samples behave at higher fields. Due to many unknowns, and lack of theoretical framework in the first place, we resort to carry out a pure geometric comparison of individual transitions. Here we calculated 1^{st} and 2^{nd} derivatives of magnetization with respect to magnetic field as shown in figure 4.3. Analyzing magnetization profiles from differential susceptibility ($\frac{dM}{dB}$) provides information on sharpness (maximum of $\frac{dM}{dB}$), width (fwhm of $\frac{dM}{dB}$) and position of the transition (magnetic field corresponding to maximum of $\frac{dM}{dB}$). In addition $\frac{d^2M}{dB^2}$ serves as a useful entity to measure asymmetry of the transition, which can be deciphered from this metric $\max(\frac{d^2M}{dB^2})/\min(\frac{d^2M}{dB^2})$. The kink observed in $\mathscr{T}_+$ transition occurs at magnetic field corresponding to $\min(\frac{d^2M}{dB^2})$. Asymmetric broadening of $\mathscr{T}_+$ transition at high temperatures towards ↑↑↑ state resembles the standard behavior of a ferromagnet, where in a typical ferromagnet thermal fluctuations influence rounding of

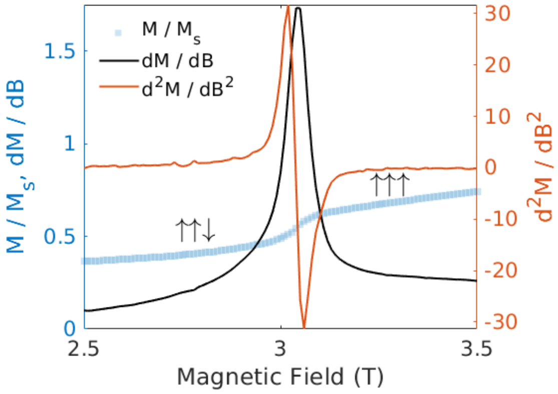

Figure 4.3 – Field-induced magnetization at 20 K, and derivatives. $\frac{dM}{dB}$ exhibits a maximum across in-field transition. $\frac{d^2M}{dB^2}$ across in-field transition has an inflection point at magnetic field corresponding to $\max(\frac{dM}{dB})$.

magnetization curves approaching saturation. The reason behind asymmetry in $\mathscr{T}_+$ transition is not known which makes a case for us to investigate this quantity $\frac{d^2M}{dB^2}$ during geometrical analysis.

A schematic B-T phase diagram of $Ca_3Co_2O_6$ is presented in figure 4.4. The zero-field region is characterized by a complicated magnetic structure, which is suggested to be a temperature- and time-dependent mixture of SDW and a commensurate AFM [59]. Above 25 K the ordered state breaks down and the system enters paramagnetic state. A horizontal dashed line is drawn at 10 K to indicate different behavior above and below this temperature. When magnetic field is applied with $T < 10$ K, a particular configuration of ↑ and ↓ spins on a triangular lattice is locked down, resulting in formation of plateaus. Vertical dashed lines at 1.2 T and 2.4 T indicate additional plateaus below 10 K. At low temperatures these plateaus are strongly pronounced and they vanish approaching 10 K. For $T > 10$ K a single ↑↑↓ configuration exists, which is also referred to as $1/3\ M_s$ plateau. Due to thermal fluctuations $1/3\ M_s$ plateau disappears beyond 18 K. Subsequent increment of field at the plateau results in a first-order transition into a fully polarized ↑↑↑ state.

$\max(\frac{dM}{dB})$ decreases strongly below 10 K, which indicates the emergence of a different magnetic behavior, which will not be dealt with in our analysis (refer figure 4.5). This is similar to what has been deduced for the $\mathscr{T}_0$ transition. One can speculate that this sudden decrease of $\max(\frac{dM}{dB})$ below might be correlated with the formation of multiple plateaus whose dynamics are governed by quantum tunneling processes rather than conventional Arrhenius law.

Temperature dependence of relative moment at the occurrence of kink is shown in figure 4.6. At temperatures close to 10 K the kink can't be easily recognized and the relative moment corresponding to $\min(\frac{d^2M}{dB^2})$ saturates to 2/3. Despite the kink is not obvious at this temperature, one can conjecture a possible configuration like 5 ↑ and 1 ↓ spins in a supercell. Another

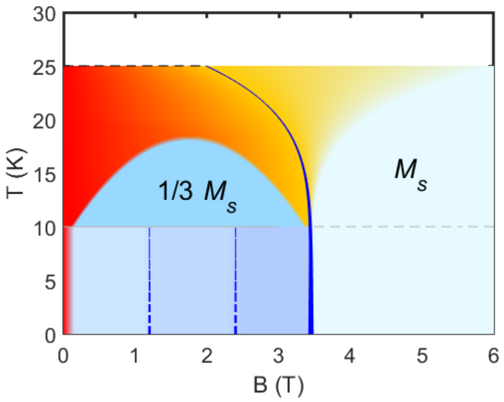

Figure 4.4 – B-T field phase diagram of $Ca_3Co_2O_6$. The plateaus at $1/3M_s$ and M_s are approximately shaded. A line is drawn at 10 K below which hysteretic behavior emerges. Dashed lines indicate appearance of additional steps at low temperatures. The ordered state breaks down at 25 K where the system enter paramagnetic state.

possibility would be the spins on average attaining 2 ↑ and 1 partially disordered state. With increase in temperature this kink in the transition becomes more apparent and close to T_N the relative moment is dropped to 1/3.

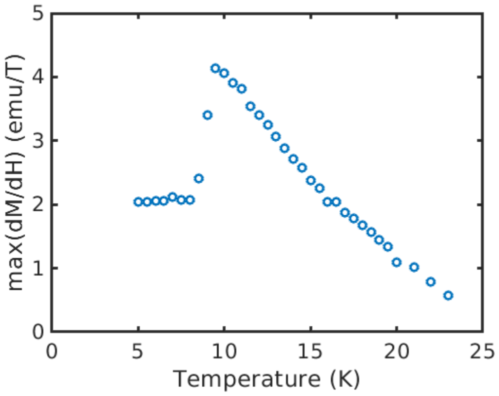

Figure 4.5 – Temperature dependence of the max($\frac{dM}{dB}$) across the $\mathcal{T}_+$ transition. A sudden drop is observed below 10 K which indicates appearance of different magnetic behavior.

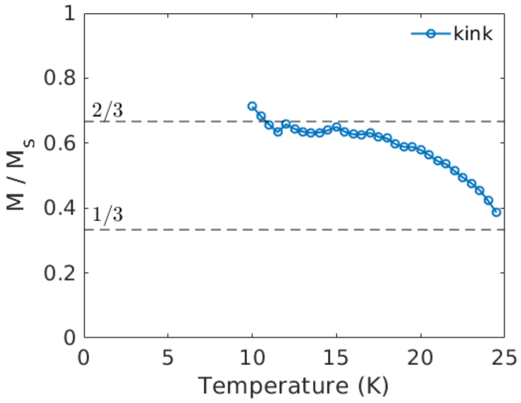

Figure 4.6 – Temperature dependence of $\frac{M}{M_s}$ at the kink, which saturates to 2/3 approaching 10 K. A possible configuration at the kink at low temperatures could be 5 ↑ and 1 ↓ state or 2 ↑ and 1 partially disordered state. Near T_N the spin configuration at the kink could be 2 ↑ and 1 ↓ state.

The occurrence of kink in the $\mathcal{T}_+$ transition is a novel feature in $Ca_3Co_2O_6$ whose origin is not properly understood. Approaching 10 K $\mathcal{T}_+$ is relatively sharp with weak curvatures approaching $M_s/3$ and M_s states, and the kink is indistinct. With increase in temperature the transition becomes broader and the curvature leading to M_s develops a sharp kink which becomes more apparent at higher temperatures. At higher magnetic fields beyond this kink magnetization curves approach moderately towards saturation. One possible explanation for the observed temperature dependence of the kink could be that with increase in temperature thermal fluctuations tend to destroy the ordered states.

4.1.2 Case 2: CoV_2O_6

As we know in $Ca_3Co_2O_6$ we had observed metamagnetic transition ($\mathscr{T}_0$) between $\uparrow\downarrow\downarrow$ and $\uparrow\uparrow\downarrow$ states through zero-field. In CoV_2O_6 a plateau is observed at $\uparrow\uparrow\downarrow$ state ($M_s/3$) however due to distorted triangular structure (refer figure 2.3) instead of $\mathscr{T}_0$, we witness $\mathscr{T}_\mathrm{I}$ transition between AFM state and $M_s/3$ plateau at non-zero field. From Wang-Landau simulation it has been understood that the exchange interactions of distorted triangle (J_1, J_2 and J_3) influence the position of $\mathscr{T}_\mathrm{I}$ transition. Under $J_1 = J_2 = J_3$ condition regular triangular structure is attained with a $\mathscr{T}_0$ transition similar to that in $Ca_3Co_2O_6$ [32].

Field-induced magnetization measurements of CoV_2O_6 are presented in figure 4.7. The profile is very similar to that in $CoCl_2{\cdot}2D_2O$ (refer figure 4.11). Unlike $Ca_3Co_2O_6$, in CoV_2O_6 at high temperatures the kink is simply $\mathscr{T}_\mathrm{I}$ transition which is less pronounced and intrinsic disorder could be one possible reason. $\mathscr{T}_\mathrm{II}$ transition terminates at $T > 10.4$ K. This is easily evident from $\frac{dM}{dB}$ which flattens out at 10.6 K as shown in figure 4.8.

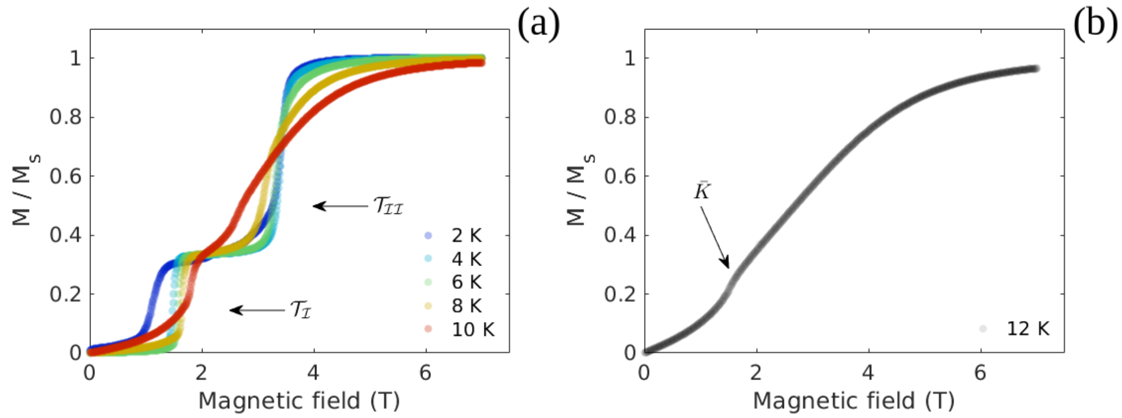

Figure 4.7 – Field-induced magnetization curves in CoV_2O_6 at temperatures where the metamagnetic transitions are apparent. In-field transitions $\mathscr{T}_\mathrm{I}$ and $\mathscr{T}_\mathrm{II}$ are indicated with arrows. The kink $\bar{K}$ in CoV_2O_6 is less pronounced compared to other two samples. Also the kink here is developed in $\mathscr{T}_\mathrm{I}$ transition.

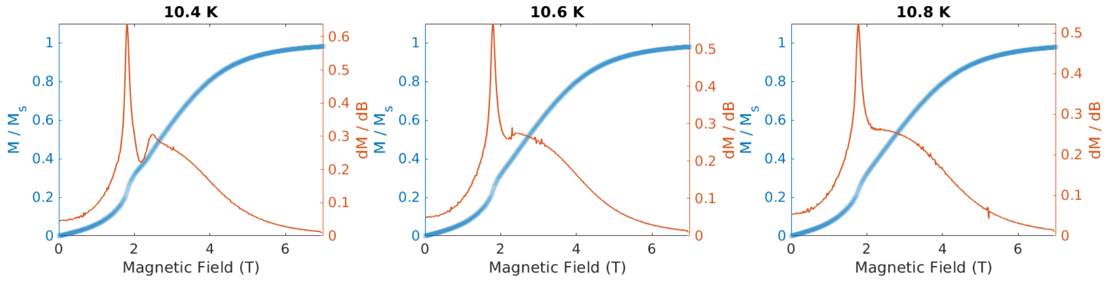

Figure 4.8 – Field-induced magnetization and corresponding $\frac{dM}{dB}$ close to T_c. One can notice that for $T > 10$ K $\mathscr{T}_\mathrm{II}$ transition becomes wider and eventually terminates at 10.4 K. $\mathscr{T}_\mathrm{I}$ transition is observed beyond T_c until the ordering is suppressed at T_N.

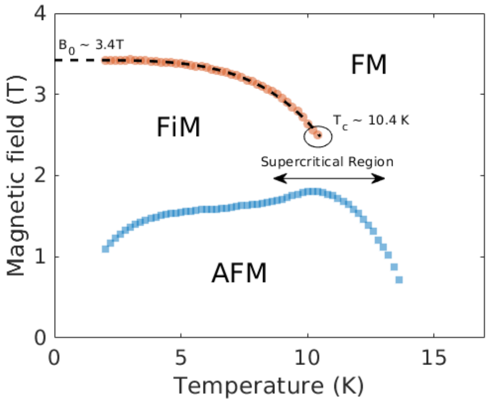

Figure 4.9 – B - T phase diagram of CoV_2O_6. Phase boundary corresponding to $\mathscr{T}_{\mathrm{II}}$ terminates at a crossover temperature T_{c}, leading to the existence of a supercritical region.

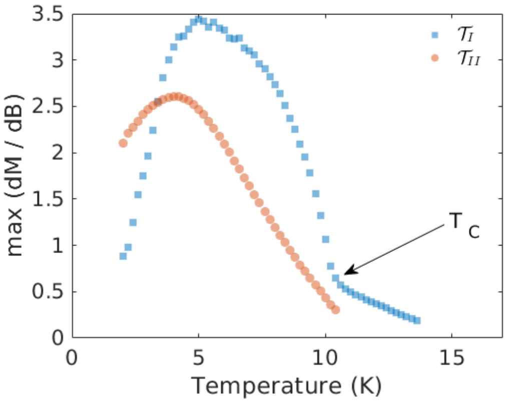

Figure 4.10 – Temperature dependence of max($\frac{dM}{dB}$) in CoV_2O_6. At crossover temperature the trajectory of max($\frac{dM}{dB}$) for $\mathscr{T}_{\mathrm{I}}$ undergoes a major deviation. At low temperatures another energy scale develops which results in decline of max($\frac{dM}{dB}$) for both transitions.

B - T phase diagram of CoV_2O_6 is shown in figure 4.9. Phase boundary corresponding to $\mathscr{T}_{\mathrm{II}}$ can be modeled to obtain the saturation field at low temperatures, however, $\mathscr{T}_{\mathrm{I}}$ exhibits different behavior. Beyond 10.4 K phase boundary of $\mathscr{T}_{\mathrm{II}}$ transition terminates at a crossover temperature T_{c}. Unlike in $CoCl_2{\cdot}2D_2O$, there is no indication of a multicritical point (refer figure 4.13). One can notice in figure 4.9, beyond T_{c} a supercritical region exists where ↑↑↓ and ↑↑↑ phases become indistinguishable.

Temperature dependence of max($\frac{dM}{dB}$) exhibit perplexing behavior (figure 4.10). For $T < T_{\mathrm{c}}$ there is uniform increase in max($\frac{dM}{dB}$) corresponding to $\mathscr{T}_{\mathrm{II}}$ down to $\simeq 4$ K. max($\frac{dM}{dB}$) corresponding to $\mathscr{T}_{\mathrm{I}}$ increases monotonously with decrease in temperature down to 5 K. Non-analytic behavior at T_{c} suggests change of character in $\mathscr{T}_{\mathrm{I}}$ below and above T_{c}. At low temperatures max($\frac{dM}{dB}$) corresponding to both $\mathscr{T}_{\mathrm{I}}$ and $\mathscr{T}_{\mathrm{II}}$ decrease indicating the emergence of a novel energy scale.

One could argue that intrinsic disorder could be play a role in suppressing $\mathscr{T}_{\mathrm{II}}$ transition "prematurely" and there might exist a multicritical point linking the phase boundaries. However, the presence of T_c in phase boundary across $\mathscr{T}_{\mathrm{II}}$ is correlated with a sudden change in the behavior of max($\frac{dM}{dB}$) corresponding to $\mathscr{T}_{\mathrm{I}}$. The effect of T_c observed in max($\frac{dM}{dB}$) corresponding to $\mathscr{T}_{\mathrm{I}}$ implies that the two field-driven transitions are convoluted with a distinct correlation.

4.1.3 Case 3: $CoCl_2{\cdot}2D_2O$

Metamagnetic transitions in $CoCl_2{\cdot}2D_2O$ closely resemble to that in CoV_2O_6 where two field-induced transitions $\mathscr{T}_{\mathrm{I}}$ and $\mathscr{T}_{\mathrm{II}}$ are observed. However, the mechanism of these transitions are different. In $CoCl_2{\cdot}2D_2O$ during $\mathscr{T}_{\mathrm{I}}$ transition, two Ising chains flip from ↓ to ↑ and one from ↑ to ↓. And in succession in the course of $\mathscr{T}_{\mathrm{II}}$ transition all the ↓ spins flip to ↑ which is relatively simple process compared to the former. A schematic of Ising chain cross section at zero-field, $M_s/3$ and saturation is presented in figure 2.5. Magnetization profiles of $CoCl_2{\cdot}2D_2O$ are shown in figure 4.11.

Around 4 K $CoCl_2{\cdot}2D_2O$ displays two field-driven transitions with obvious plateaus. With increase in temperature the plateaus are smeared out and transitions become weaker and broader. $\mathscr{T}_{\mathrm{I}}$ transition is shifted towards higher magnetic fields while the opposite is seen for $\mathscr{T}_{\mathrm{II}}$. $\mathscr{T}_{\mathrm{I}}$ and $\mathscr{T}_{\mathrm{II}}$ transitions terminate around 9.4 K with the appearance of a multicritical point (T_{MC}).

Beyond 9.4 K only one transition exists, which we shall denote as $\mathscr{T}_{\mathrm{III}}$. A noticeable feature in $\mathscr{T}_{\mathrm{III}}$ transition is the development of a kink similar to $Ca_3Co_2O_6$, which becomes more pronounced with increase in temperature until the transition is concealed close to T_N. The geometry of field-induced magnetization and corresponding $\frac{dM}{dB}$ around T_{MC} are shown in figure 4.12.

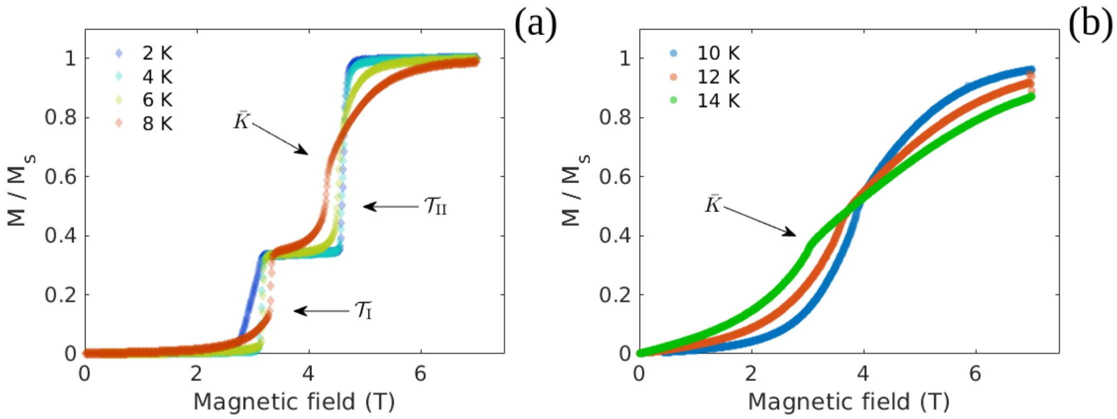

Figure 4.11 – Magnetization fieldscan profile of $CoCl_2{\cdot}2D_2O$. Metamagnetic transitions $\mathscr{T}_{\mathrm{I}}$ and $\mathscr{T}_{\mathrm{II}}$, and kink $\bar{K}$ are indicated using arrows. At higher temperatures (T>T_{MC}) a kink ($\bar{K}$) is observed which itself is the transition ($\mathscr{T}_{\mathrm{III}}$).

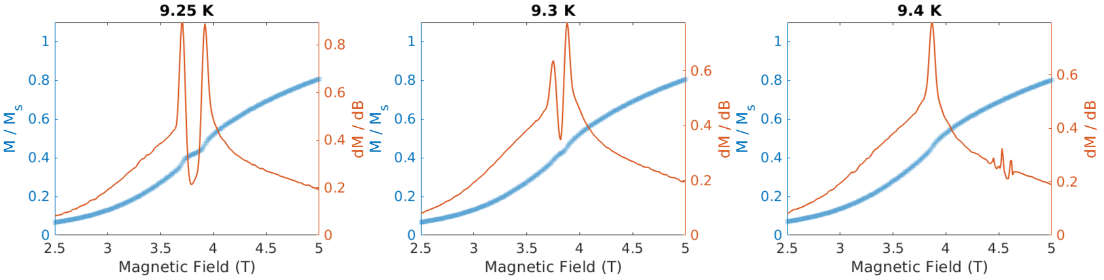

Figure 4.12 – $\frac{dM}{dB}$ of magnetization curves have been used to inspect the termination of $\mathscr{T}_\text{I}$ and $\mathscr{T}_\text{II}$ close to T_MC. Beyond 9.4 K only $\mathscr{T}_\text{III}$ exists.

The phase diagram in B - T plane is shown in figure 4.13. Phase boundaries across $\mathscr{T}_\text{I}$ and $\mathscr{T}_\text{II}$ meet at T_MC. Beyond T_MC the field-induced transition occurs between AFM and FM phase

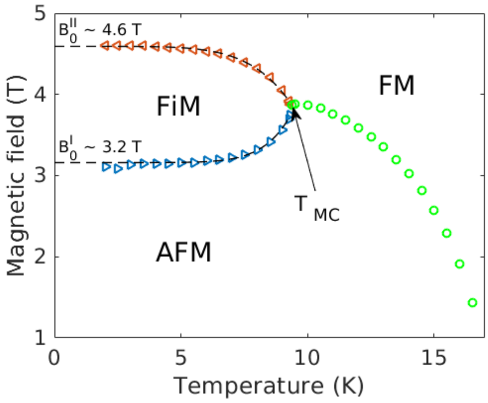

Figure 4.13 – B-T phase diagram of $CoCl_2{\cdot}2D_2O$. A multicritical point is observed close to 9.4 K, denoted using an arrow. B_0^I and B_0^II indicate magnetic fields at which phase boundaries saturate at low temperatures.

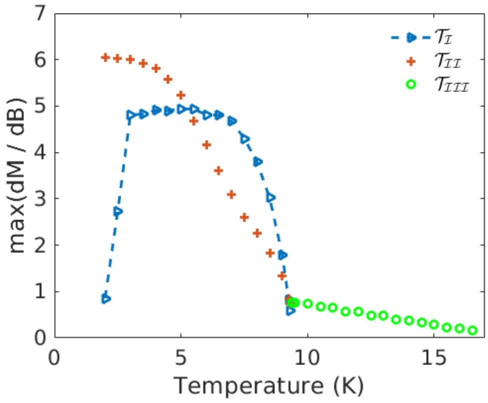

Figure 4.14 – Temperature dependence of max($\frac{dM}{dB}$) in $CoCl_2{\cdot}2D_2O$. Notice the sudden drop in max($\frac{dM}{dB}$) of $\mathscr{T}_\text{I}$ below 3 K due to a different energy scale which doesn't affect $\mathscr{T}_\text{II}$.

without the intermediate FiM phase.

max($\frac{dM}{dB}$) in $CoCl_2{\cdot}2D_2O$ not only displays some unusual features, but also well distinguishes the inherent behavioral differences between the transitions. $\mathcal{T}_{\mathrm{III}}$ is significantly less sharper than $\mathcal{T}_{\mathrm{I}}$ and $\mathcal{T}_{\mathrm{II}}$, well distinguished at T_{MC}. Thermal fluctuations would be the most likely reason behind the monotonous decrease of max($\frac{dM}{dB}$) beyond T_{MC}. Below T_{MC}, max($\frac{dM}{dB}$) for $\mathcal{T}_{\mathrm{I}}$ transition grows sharper abruptly compared to $\mathcal{T}_{\mathrm{II}}$, but remains temperature invariant between 3K to 8 K where the exchange interactions are much stronger than thermal fluctuations. Below 3 K max($\frac{dM}{dB}$) drops suddenly indicating emergence of a novel energy scale, which has not been reported so far. This sudden drop in max($\frac{dM}{dB}$) is only observed in $\mathcal{T}_{\mathrm{I}}$ and surprisingly doesn't affect $\mathcal{T}_{\mathrm{II}}$ which is indeed puzzling.

4.2 Disparate Origin and Similarity

4.2.1 Data Collapse

In all the three sample that we have studied so far, at high magnetic fields all moments are parallel (↑↑↑ configuration), which is a well defined state. When field is lowered one spin out of three flips down (↑↑↑→↑↑↓ transition). This observation is universal to all the samples despite different ground states.

Here we propose data collapse of individual magnetization curves of all three samples at different temperatures and aim to establish a scaling diagram. Individual fieldscans of different samples were normalized to their respective saturation value. We chose to fix a fieldscan of one sample at a particular temperature and then compare the fieldscans of another at few adjacent temperatures.

For example, fieldscan of $Ca_3Co_2O_6$ at 18.5 K has been compared with that of CoV_2O_6 at different temperatures as shown in figure 4.15. At higher field values fieldscan profile of $Ca_3Co_2O_6$ agrees the best with CoV_2O_6 at 7.6 K (figure 4.15b). Similar comparison has been performed for a range of temperatures from 15 K to 25 K of $Ca_3Co_2O_6$. Below 15 K the proportion of overlapping region at higher fields tend to decrease making the analysis obsolete.

Taking into account that both samples undergo in-field transition from a common spin configuration (↑↑↓), data collapse has also been attempted at the 1/3rd plateau. One can notice that at the plateau $Ca_3Co_2O_6$ 18.5 K has good agreement with CoV_2O_6 at 8 K (figure 4.16b) instead of 7.6 K (figure 4.16a). In $Ca_3Co_2O_6$ for $T > 20$ K the plateau gets smeared out completely and hence beyond this temperature comparison with CoV_2O_6 at ↑↑↓ configuration is implausible. In these analysis no prefactor has been multiplied and surprisingly the in-field transitions in both the samples occur at close by field values at comparable temperatures.

Field-driven transitions in $CoCl_2{\cdot}2D_2O$ occur at higher magnetic fields compared to CoV_2O_6 possibly due to stronger exchange interactions. Hence, a prefactor has been multiplied in

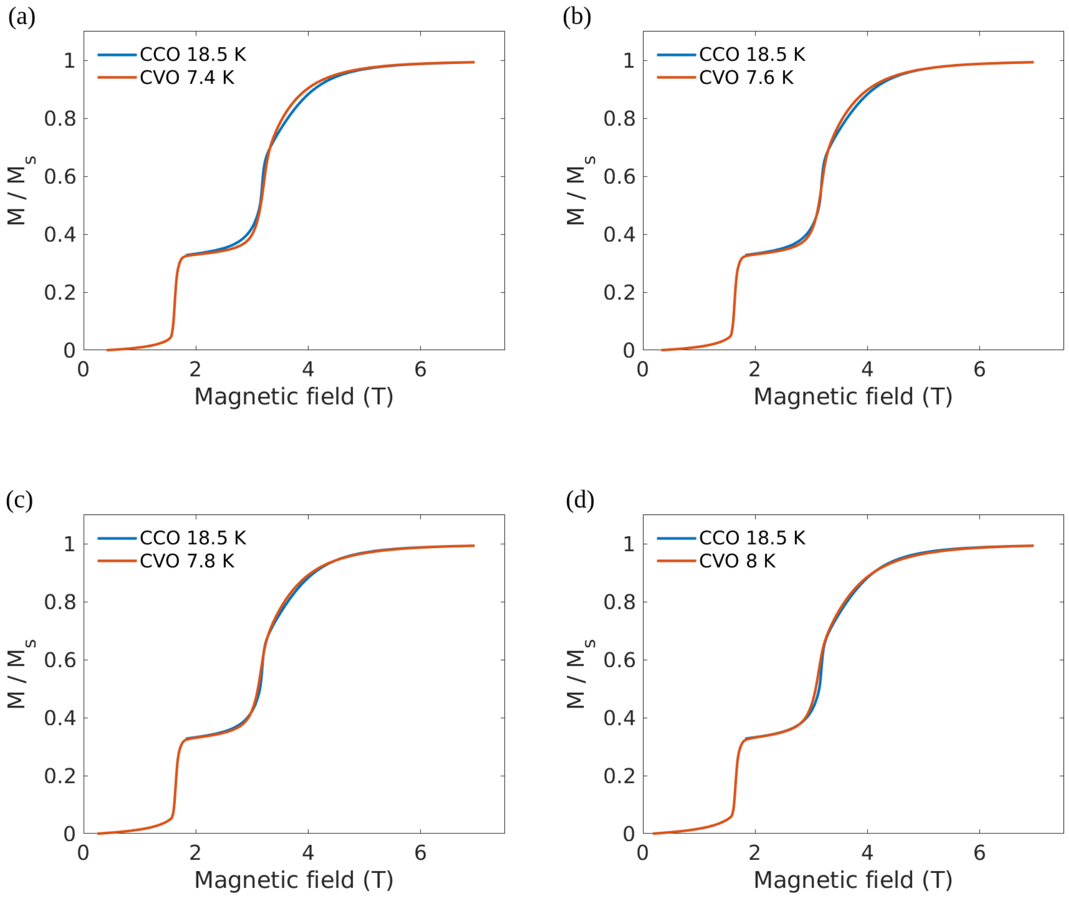

Figure 4.15 – Comparison of $Ca_3Co_2O_6$ fieldscan at 18.5 K with several fieldscans of CoV_2O_6. Best overlap of fieldscan profiles is observed in (b). In (a), (c) and (d) the profiles appears to overlap well yet there exists slight mismatch at higher fields. These comparisons are observational and are not statistically analyzed.

order to make a direct comparison possible as shown in figure 4.17b. The value of prefactor is not constant and differs slightly for different temperatures. Likewise, a prefactor has been multiplied during comparison of $Ca_3Co_2O_6$ and $CoCl_2{\cdot}2D_2O$ fieldscans as shown in figure 4.18.

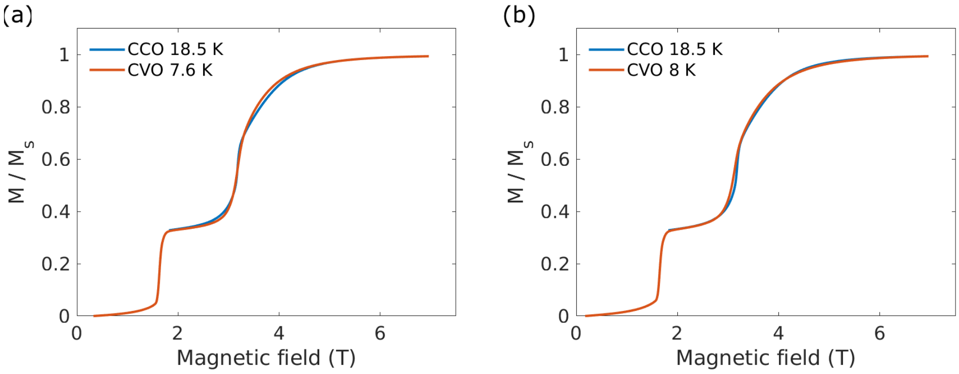

Figure 4.16 – Comparison of $Ca_3Co_2O_6$ fieldscan at 18.5 K with fieldscans of CoV_2O_6 at 7.6 K (a) and 8 K (b). The former plot showcases data collapse close to saturation (↑↑↑), and the latter one at the plateau (↑↑↓).

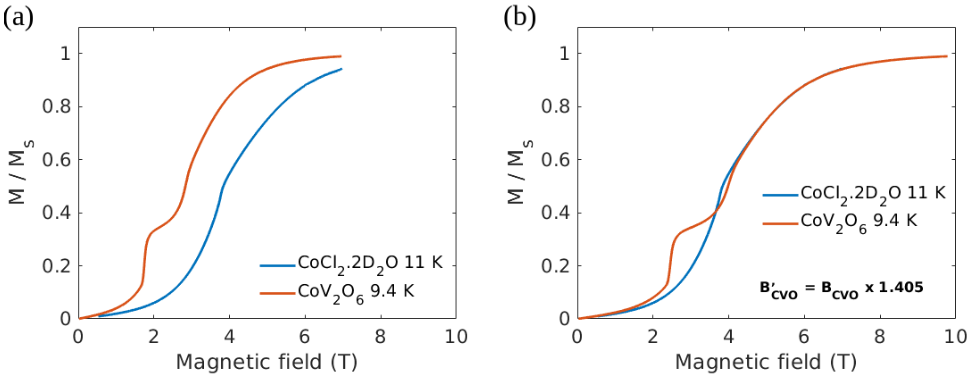

Figure 4.17 – Re-scaling magnetic field (x-axis) of CoV_2O_6 in order to make a comparison with that of $CoCl_2{\cdot}2D_2O$ (a) Original data of individual magnetization profiles (b) A prefactor of 1.405 has been multiplied for comparison.

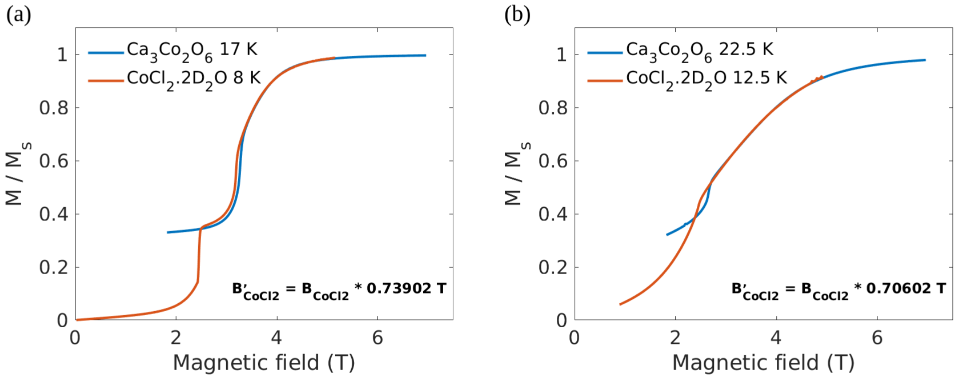

Figure 4.18 – Re-scaling magnetic field (x-axis) of $CoCl_2{\cdot}2D_2O$ to compare with $Ca_3Co_2O_6$. Comparisons at different temperatures are shown in (a) and (b).

4.2.2 Scaling Diagram

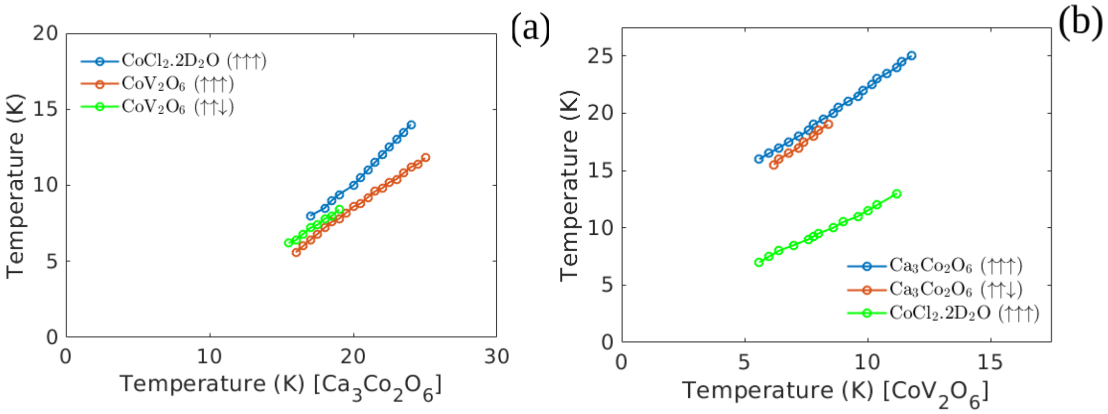

Figure 4.19 – Scaling diagram depicting the scaling behavior of magnetization curves at saturation and $1/3^{\text{rd}}$ plateau.

Considering the best case, a scaling diagram has been created (figure 4.19) where temperature of compared profiles are plotted with one as a function of another. In figure 4.19a $Ca_3Co_2O_6$ is fixed and temperatures of CoV_2O_6 and $CoCl_2{\cdot}2D_2O$ are over-plotted. Likewise in figure 4.19b CoV_2O_6 is compared with $CoCl_2{\cdot}2D_2O$ and $Ca_3Co_2O_6$.

Scaling diagram provides us insight on how seemingly different magnetization profiles can be wrapped in a unique framework. $Ca_3Co_2O_6$, CoV_2O_6 and $CoCl_2{\cdot}2D_2O$ profiles agree well with one another close to $\uparrow\uparrow\uparrow$ spin state at several temperatures. There is a linear correlation with this agreement. $Ca_3Co_2O_6$ and CoV_2O_6 were also compared at $\uparrow\uparrow\downarrow$ spin state, which coincidentally is also linear but remains distinct from the interrelationship at $\uparrow\uparrow\uparrow$ spin state. This provides an indirect reference to the fact that $\mathscr{T}_+$ transitions of $Ca_3Co_2O_6$ are broader than $\mathscr{T}_{\text{II}}$ of CoV_2O_6. The correlation of $Ca_3Co_2O_6$ with $CoCl_2{\cdot}2D_2O$ is spread over larger range of temperatures since T_{N} of $CoCl_2{\cdot}2D_2O$ is observed to be at higher temperature than CoV_2O_6.

The interrelationship between all three samples is observed to be linear. Regardless of the dynamics within the transition and innate ground state of individual systems, the trajectory of magnetization curves close to initial and final state of the three samples are analogous. This provides us with the first-step in establishing a similarity in $\uparrow\uparrow\downarrow \longleftrightarrow \uparrow\uparrow\uparrow$ transition.

4.3 Conclusion

Field-induced metamagnetic phase transitions in Ising chains were studied in three samples.

Highly frustrated $Ca_3Co_2O_6$ exhibit two metamagnetic transitions $\mathscr{T}_0$ and $\mathscr{T}_+$ at zero-field and non zero-field respectively. $\mathscr{T}_0$ is highly dynamic where $\uparrow\downarrow\downarrow$ and $\uparrow\downarrow\downarrow$ phases coexist at all spatial scales. Since both the phases contain both orientations of spins, it is practically impossible to distinguish dynamic and static part. Contrarily $\mathscr{T}_+$ is a simpler version where the dynamic part is carried by segments of $\downarrow$ spins, while the static background contains only $\uparrow$ spins. From this perspective, $\mathscr{T}_+$ represents a somewhat simpler version of $\mathscr{T}_0$.

In CoV_2O_6 and $CoCl_2{\cdot}2D_2O$, unlike $Ca_3Co_2O_6$, no $\mathscr{T}_0$ transition is seen here, instead there are two in-field transitions $\mathscr{T}_\mathrm{I}$ (AFM-FiM) and $\mathscr{T}_\mathrm{II}$ (FiM-FM). Qualitatively transitions in both the samples behave similar, however, in CoV_2O_6 the kink in transition at high temperatures is not obvious likely due to intrinsic disorder. However, disparity in character between two samples arise due to the presence of T_MC in $CoCl_2{\cdot}2D_2O$ and supercritical region in CoV_2O_6.

From the field-induced magnetization measurements we have strove to establish similarity in the magnetization profiles and beyond. Our initial approach entailed overlapping magnetization profiles where we have discovered that for a range of temperatures the profiles display analogous behavior as shown in figure 4.19.

To understand the dynamical aspects of $\uparrow\uparrow\downarrow\longleftrightarrow\uparrow\uparrow\uparrow$ transition, ac susceptibility measurements were carried out. Additional survey of universal features from dynamical viewpoint is discussed in upcoming chapters.

5 Dynamical Aspects of Metamagnetic Transitions

This chapter is in part extracted from the following publication

- Nagabhushan G. Hegde, Ivana Levatić, Arnaud Magrez, Henrik M. Rønnow, and Ivica Živković, Magnetic dynamics across the in-field transition in $Ca_3Co_2O_6$, Phys. Rev. B **102**, 104418

Ac susceptibility is an excellent tool to probe magnetic structures that exhibit slow dynamics. There are two components in ac susceptibility measurement, in-phase χ' and out-of-phase χ'', often referred as real and imaginary components respectively. At lower frequency limit χ' can be associated with differential susceptibility $\frac{dM}{dB}$. χ' is the elastic part, and χ'' is the dissipative part containing information on the density of states that take part in dissipative processes during a single cycle of magnetic field. Using this technique here we seek to understand the dynamical characteristics of $\mathscr{T}_+$ transitions.

5.1 Near Identical Superparamagnet-like Behavior in $\mathscr{T}_0$ and $\mathscr{T}_+$ Transitions

Specific features of magnetic structure in a single chain can be highlighted by analyzing the temperature dependence of the magnetic susceptibility χ'(T). Typical behavior observed in case of Ising model would be that the longitudinal susceptibility diverges exponentially with decreasing temperature while the transverse susceptibility remains constant and much smaller than the former. Longitudinal susceptibility here can be affiliated with Arrhenius equation [30].

Ac susceptibility was measured as a function of temperature from 5 K to T_N at constant magnetic field at several frequencies ranging from 10 Hz up to 10k Hz. We measured temperature dependence at three characteristic fields as follows: (i) $B = 0$ (middle of $\mathscr{T}_0$), (ii) $B = 1.85$ T (middle of $1/3M_\mathrm{S}$ plateau), and (iii) $B = 3.5$ T (middle of $\mathscr{T}_+$) as shown in figure 5.1.

Previously neutron diffraction [58] and specific heat measurements [79] at zero-field indicated the occurrence of long range ordering (LRO) at T_{N}. On the other hand in ac susceptibility there is no signature of this transition at T_{N} where temperature scans at all measured frequencies don't show any feature around this temperature. max($\chi_{,}$) that observed below T_{N} is strongly dependent on frequency [$\Delta T_{\mathrm{M}} / (T_{\mathrm{M}} \Delta\omega) \simeq 0.15$], mimicking the behavior observed in superparamagnetic systems [45]. Near the middle region of $1/3M_{\mathrm{s}}$ plateau a clear kink is observed in susceptibility which slowly drops to practically zero value with decrease in temperature. Compared to the highly dynamic case of $B = 0$, no quantifiable frequency dependence is seen indicating a robust $\uparrow\uparrow\downarrow$ state. With further increase in magnetic field into the middle of $\mathscr{T}_+$ transition once again a frequency dependent dynamics is observed similar to zero-field case. Comparing to zero-field in this case the width of the dynamic region is moderately narrower at every frequency and the amplitude of χ' is reduced a bit. At $T < 10$ K the signal is in effect zero at all frequencies in contrast to the presence of rich and significant dynamics at low temperatures. The similarity in the overall appearance with respect to zero-field case provides reliance to establish a common dynamical framework in $\mathrm{Ca_3Co_2O_6}$.

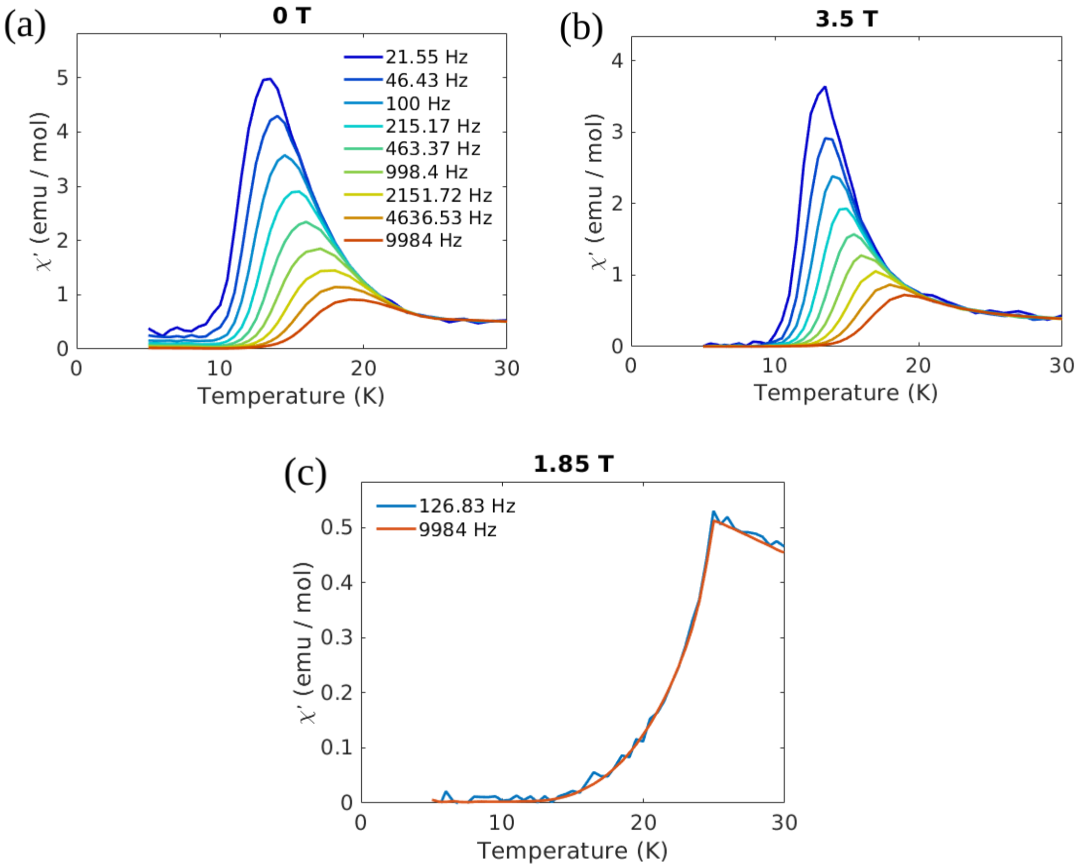

Figure 5.1 – Temperature dependence of ac susceptibility in $\mathrm{Ca_3Co_2O_6}$ for $B = 0$ T, 3.5 T and 1.85 T. Qualitatively temperature scans of susceptibility in the middle of $\mathscr{T}_0$ and $\mathscr{T}_+$ transitions are alike with no features around T_{N}. Measurements at the $1/3^{\mathrm{rd}}$ plateau reveal a sharp feature at T_{N} and a drop in the values to zero at low temperatures.

5.2 Investigation of Slow Dynamics across $\mathscr{T}_+$ transition in $Ca_3Co_2O_6$

For ac susceptibility field scans were measured between 3.3 T and 3.7 T, enclosing most of the $\mathscr{T}_+$ transition. Amplitude of the ac magnetic field was set to 5 Oe for all frequencies in the range of 10 Hz to 10 kHz.

The field dependence of ac susceptibility across $\mathscr{T}_+$ transition was measured at several temperatures as shown in figure 5.2, and respective $\frac{dM}{dB}$ has been included for comparison. $\frac{dM}{dB}$ displays a single maximum at B_{dc}, which shifts to lower fields with increase in temperature. This corresponds to a shift of sharp jump in magnetization as observed in figure 4.1. The behavior of ac susceptibility is complicating and exhibits an unusual frequency dependence, with two characteristic features emerging. The first feature is dependent on temperature, and following the same trend as B_{dc}. This indicates that low frequency fieldscans reflect a behavior characteristic of low frequencies. The second feature is independent of temperature and centered at $B_\infty = 3.49$ T. The observed behavior is independent of the sweep direction of magnetic field.

It is worth noting that qualitatively both χ' and χ'' demonstrate similar behavior, but there are some differences that can be noticed. At all measured temperatures B_∞ peak is very wide, spreading out across the transition. Whereas, B_{DC} peak associated with the dc regime appears to display smaller width and getting more pronounced in the imaginary component.

Colorplots of imaginary component were plotted to for better visualization of temperature, magnetic field, and frequency dependence of the two characteristic features as presented in figure 5.3. Taking into account the several orders of magnitude difference in the values of susceptibility measured at different frequencies used in this study, each fieldscan has been normalized at the given frequency to its maximum value. This allows us to inspect several important details of the $\mathscr{T}_+$ transition. With two well-defined characteristic features, there is a crossover region in frequency where both these features are present. At high temperatures, where the separation between features is considerable compared to the width of peaks, there are indeed two maxima in χ'' at a given frequency (for example, $\nu = 2333$ Hz at $T = 15$ K). At lower temperatures the crossover shifts to lower frequencies, and the separation between the two features becomes smaller, making it difficult to differentiate in fieldscans for a single frequency. Approaching $T = 10$ K, the crossover frequency drops below 10 Hz (the lower limit of our measurements) while at the same time it becomes in effect impossible to distinguish B_{dc} and B_∞.

The temperature dependence of the crossover frequency is plotted in figure 5.4. It traverses three orders of magnitude in a relatively narrow temperature window. At higher temperatures a weak curvature is present, indicating a possible saturation. We need ac susceptibility experimental setups allowing measurements at high frequency range to investigate such development towards T_{N} [80]. At lower temperatures one would also profit from the extension to lower frequencies with a caution that the shrinking difference between B_{dc} and B_∞ will make the identification of the crossover frequency equivocal.

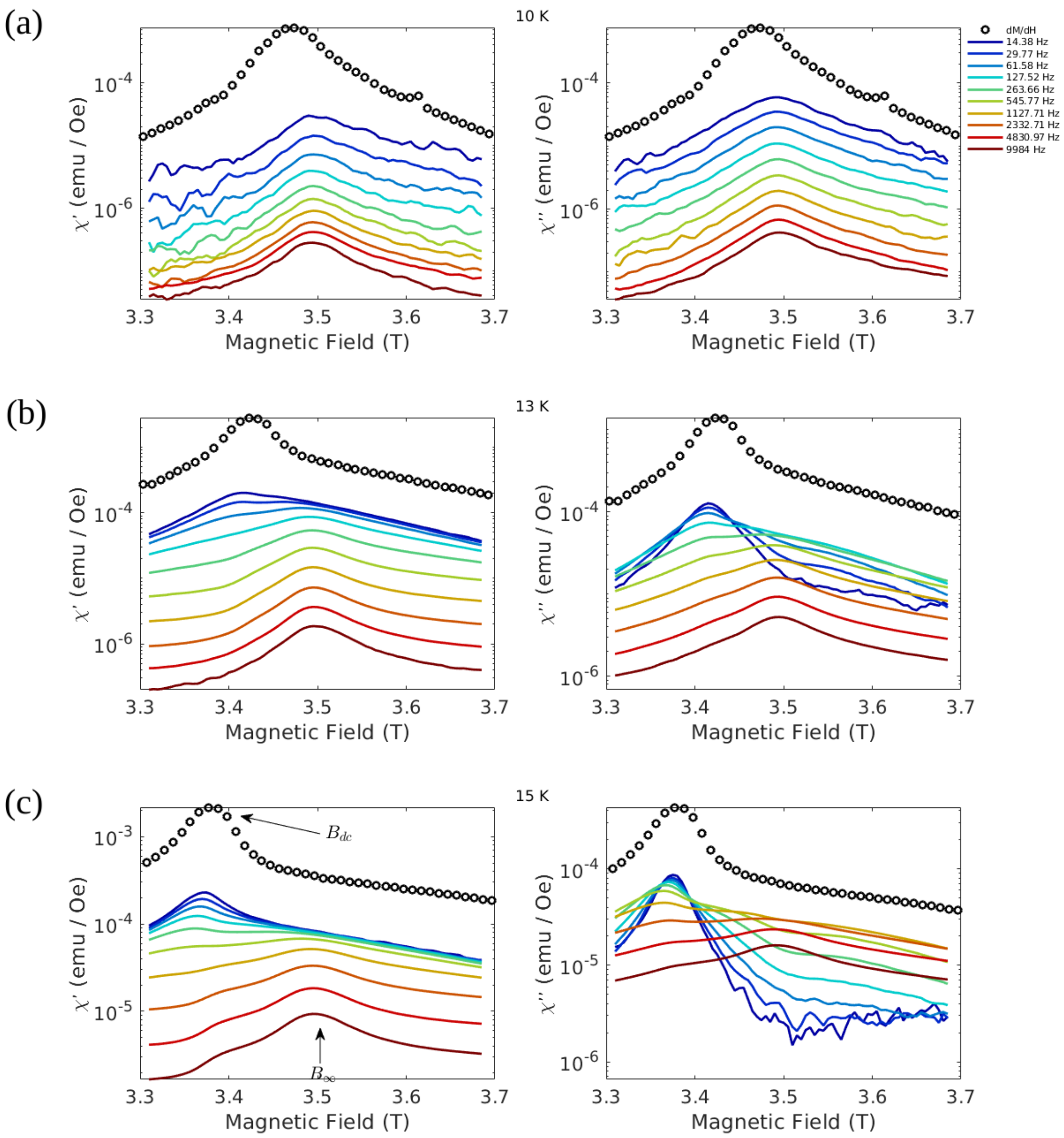

Figure 5.2 – Ac susceptibility across $\mathscr{T}_+$ transition for $T = 10$ K. The individual fieldscans are smoothed using a moving average. Real component is presented on the left subplot and imaginary on the right. B_{DC} and B_∞ are indicated using arrows.

It is informative to look more carefully into the frequency dependence of the susceptibility. At 10 K the values of χ'' monotonically increase with decreasing frequency in the whole field range investigated. On the other hand χ'' at 13 K and 15 K show a strong non-monotonic behavior. The typical frequency dependence of both χ' and χ'' is plotted in figure 5.5, at $T =$ 15 K and several values of field. χ' displays a saturation at low frequencies and tends to zero at high frequencies, while χ'' exhibits a bell-shaped curve with the maximum observed at the inflection point of χ' . All these features are characteristic of a system whose relaxation

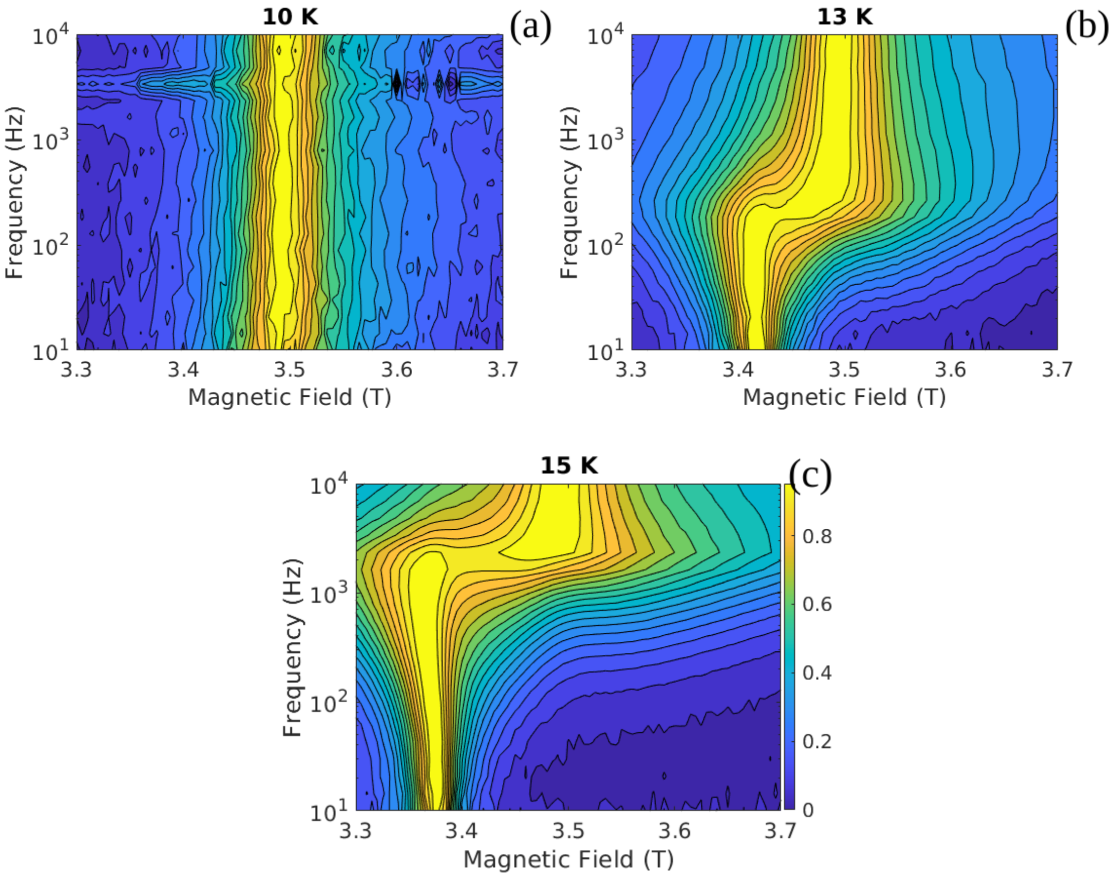

Figure 5.3 – Color maps of the imaginary component where the maximum amplitude of each frequency profile is normalized to unity

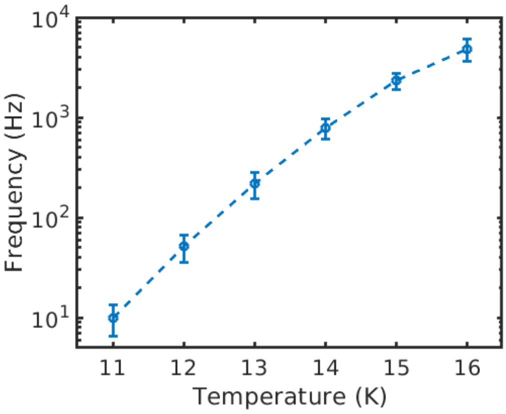

Figure 5.4 – Temperature dependence of the crossover frequency

time $\tau = 1/(2\pi f_{\max})$, with $f_{\max}$ being the value of frequency where the maximum in χ'' occurs. Typically, $f_{\max}$ is found to be below 10 kHz in superparamagnets and spin glasses [45]. As stated before, the temperature dependence of the maximum in susceptibility firmly indicates superparamagnetic like behavior in this compound, in strong agreement with previous reports [52, 81].

5.2.1 Implementation of Cole-Cole Model

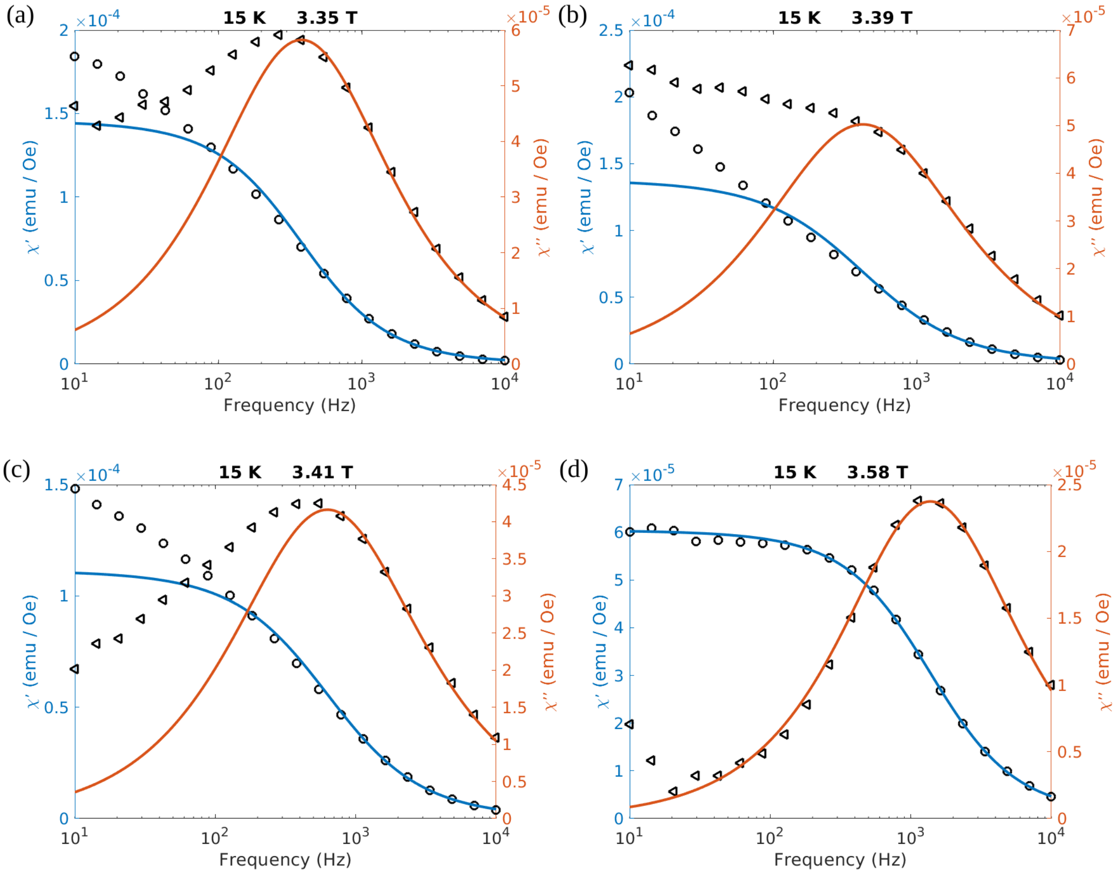

Figure 5.5 – Frequency dependence of susceptibility at T = 15 K for several values of B. Circles represent χ', and triangles show χ''.

In any real material rarely a single relaxation time is observed. Often there exists a distribution of relaxation times. In case of superparamagnets or single domain particles this distribution of relaxation times arise from nonuniform size and/or shape distribution. In addition, the environment can also influence how the particles respond to external field. Here we fit the frequency scans using Cole-Cole model which comes under the category of generalized Debye models, where the distribution of relaxation times is phenomenologically accounted for by introducing the parameter α. The equation of Cole-Cole model is given below:

$$\chi(\omega) = \chi_\infty + \frac{\chi_0 - \chi_\infty}{1 + (i\omega\tau)^{1-\alpha}} \tag{5.1}$$

which leads to the following expressions for χ' and χ'':

$$\begin{aligned}\chi'(\omega) &= \frac{1}{2}(\chi_0 - \chi_\infty)\left\{1 - \frac{\sinh[(1-\alpha)\mathbf{x}]}{\cosh[(1-\alpha)\mathbf{x}] + \sin(\alpha\pi/2)}\right\} + \chi_\infty \\ \chi''(\omega) &= \frac{1}{2}(\chi_0 - \chi_\infty)\left\{\frac{\cos[(\alpha\pi/2)]}{\cosh[(1-\alpha)\mathbf{x}] + \sin(\alpha\pi/2)}\right\}\end{aligned} \tag{5.2}$$

where $\mathbf{x} = \ln(\omega\tau)$, χ_0 and χ_∞ are susceptibilities in the zero and infinite limits, respectively. α = 0 corresponds to a single characteristic time in which case equation 5.1 reduces to Debye model. The distribution function of Cole-Cole model can be derived mathematically, further discussed in appendix B.

This phenomenological approach applied on our measured data is shown in figure 5.5 for several characteristic fields at T = 15 K. Above B_∞ the entire frequency range could be well described with equation 5.2. Below B_∞ a systematic increase of the low frequency region can be noticed, which results in an asymmetric frequency profile of the χ''. In such case we chose to use only the high-frequency side for the fit. On further decreasing magnetic field and approaching B_{dc}, the low-frequency side becomes dominant, with the former maximum becoming a pronounced shoulder. For these values of magnetic field, determining the high-frequency range used for the fit becomes rather unequivocal, and the extracted values should be considered to be only an estimate. On the lower side of B_{dc} the low frequency contribution reduces again, with a maximum in χ'' reappearing in the same frequency window around 400 Hz.

5.2.2 Relaxation Time and Energy Barrier

The temperature and field dependence of extracted parameters are studied here. In figure 5.6 field dependency of f_{max} and α are shown separately for a range of temperatures. In addition to the overall shift in frequency with temperature, one can observe that extracted parameters at all chosen temperatures follow somewhat uniform behavior. For $B > B_\infty$, f_{max} is relatively constant with slight curvature at higher temperatures producing a shallow minimum around 3.6 T. At the same time α values are observed in the range 0.1 - 0.25, much lower than the value found from a similar analysis at zero field and T = 2 K ($\alpha \simeq 0.55$ in reference [52]).

For $B < B_\infty$ there is an obvious tendency of f_{max} decreasing along with an adjacent linear relationship between $\log_{10}(f_{\mathrm{max}})$ and B. Close to the region around B_{dc} a minimum of f_{max} is observed and below this field the trend reverses (marked by a thick dotted line).

In the same range of field range α was extracted whose value remains around 0.25 or below. An unusual inversion with respect to $B > B_\infty$ has been observed where α for T = 13 K values decrease and T = 16 K increase. At T = 12 K the projected behavior is attributed to the fact where f_{max} values are low and can't be deconvoluted from the upturn seen at low frequencies. Too much emphasis should not be given for the extracted values of α since only half of the

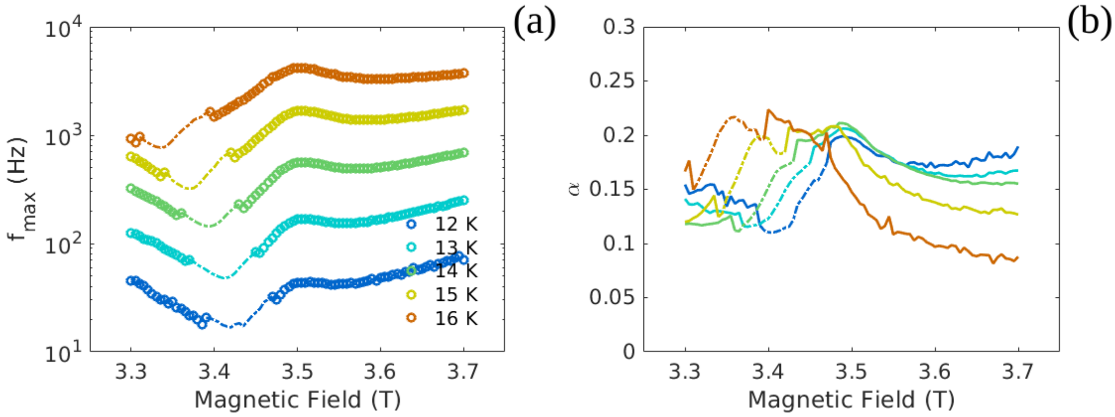

Figure 5.6 – Magnetic field and temperature dependence of the frequency f_{max} and width α where χ" exhibits a maximum.

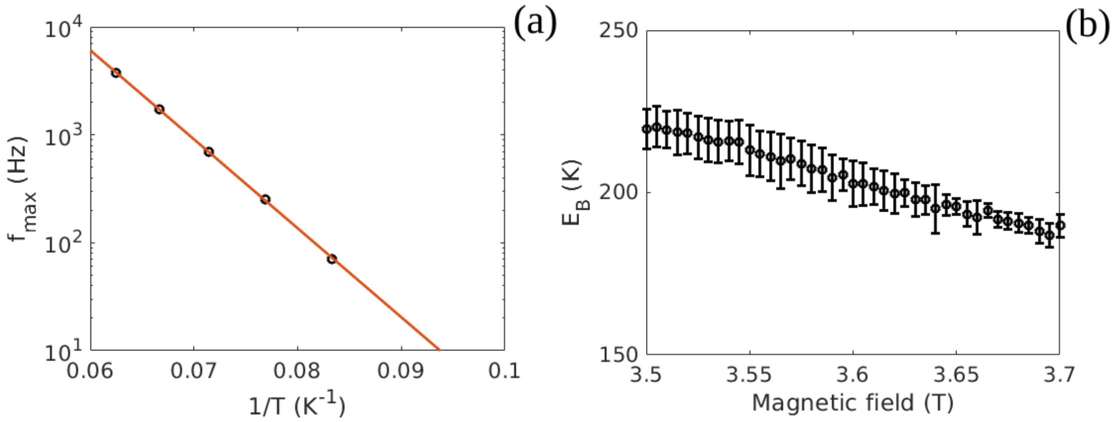

Figure 5.7 – Temperature dependence of the characteristic frequency at B = 3.58 T. The solid line is a fit following the Arrhenius law described in equation 5.3. E_{B} above B_∞.

frequency profile has been utilized during the fit. Measurements at low frequency range is necessary, which include upturn at low frequencies, to obtain a reliable set of extracted parameters.

Close to the minimum of f_{max} the extracted parameters determined from the fit are highly uncertain in their values and hence they are represented using thick dotted lines in our plot differentiating rest of data where symbols (f_{max})) and solid lines (α) are used. Yet it has been clear that there must be a minimum in f_{max} vs B since on both at both higher and lower field sides the reliable set of data shows a (quasi)linear behavior with opposite slopes. In addition, the region where low frequency contribution is dominant is somewhat limited (except at T = 12 K), such that different methods would not make a significant difference in the values of minima. In our approach the minimum of f_{max} is observed at B = 3.37 T close to B_{dc} = 3.36 T for T = 15 K firmly indicating the common underlying process in the two features.

A somewhat uniform behavior in f_{max} beyond B_{dc} has simplified to quantify the temperature dependence shown in figure 5.6, where the data is extracted for $B = 3.58$ T. Further this figure includes a fit to generate a simple activation energy dependence using the below equation:

$$f_{\text{max}} = f_0 \exp(-\frac{E_{\text{B}}}{k_{\text{B}} T}) \tag{5.3}$$

In this equation k_{B} is the Boltzmann constant, f_0 is the attempt frequency given by the number of attempts per second by thermal fluctuations where the magnetic moment attempts to reverse it's spin against the energy barrier, and E_{B} is the energy barrier indicating energy needed for a correlated spin cluster of moments to flip its direction. In figure 5.7 energy barrier $E_{\text{B}}(B)$ is plotted to show that a very weak field dependence, with values nearly ranging between 190 K and 220 K. This can be compared with previous result extracted by Hardy *et al* at $T = 2$ K, $B = 0$ is 135 K [52]. f_0 values extracted were in the order of 10^9 Hz. It is assumed that Zeeman energy only affects the energy barrier and not the switching rate across the transition, and hence the value of f_0 was fixed during the fitting of energy barrier.

5.2.3 Discussion

The peculiarities of zero-field state [81], extreme long time scales attributed to different spin configurations [59], and perplexing dynamics [52] have influenced in focusing the research in $Ca_3Co_2O_6$ at zero-field state for a long time. Similar to the usual approach taken for investigating magnetic properties in materials, the objective was to look for equilibrium state. In recent years, there has been increasing attention towards comprehending non-equilibrium phenomena, its core principles and application to individual systems [82]. Since the zero-field state of $Ca_3Co_2O_6$ is right in the middle of $\mathscr{T}_0$ transition, to understand the dynamics of internal processes field-induced non-equilibrium measurements need to be well understood.

Since at low temperatures $T < 10$ K results in complications involving hysteresis, multiple plateaus and extreme long timescales, we shall focus $\mathscr{T}_+$ transition for $T > 10$ K. Across $\mathscr{T}_+$ transition application of field will result in certain number of spin reversal inducing M. The timescale associated with this transition can be studied using Arrhenius law since the spin reversal is related to the energy barrier E_{B}. Obviously, beyond 3.5 T where most of the spins are pointing up, the cluster spin reversal is straightforward where energy barrier is practically independent of field. The range of α lies between 0.1 and 0.2, which are extracted from the individual fits (figure 5.6). They are compared to previously reported values by Hardy at $T = 2$ K and $B = 0$ T which was found to be $\alpha \simeq 0.55$ [52]. As we know longer time scales are observed in systems that exhibit sloe dynamics like superparamagnets and spin glasses. One can mention examples of archetypal spin glasses like $(Eu_{0.4}Sr_{[}0.6])S$ and CuMn (5 at. %) where α decreases monotonously from 1 (infinite width) at lowest measured temperature down to 0.2 at $2T_{\text{f}}$, where T_{f} is the freezing temperature of a spin-glass system [83]. In the same article it has also been mentioned on superparamagnetic systems to encounter α between 0.5 and 0.7, independent of temperature. On inspecting figure 5.6 where temperature dependence of

α beyond 3.5 T provides a hint of single relaxation time at temperatures around 20 K where $\alpha \rightarrow 0$. If this conjecture is true then it will open up new pathways to characterize the sample from microscopic methods and obtain understanding of smallest dynamic unit in $Ca_3Co_2O_6$.

The energy barrier value calculated from our analysis is a bit higher than the previously reported one [52] although at different field and temperature. Inelastic neutron scattering experiments have revealed large spin gap of ≃27 meV (= 313 K) characterizing magnon dispersion in $Ca_3Co_2O_6$, associated with large single-ion anisotropy [84]. If one follows the idea put forward through Monte Carlo simulations [60], a simple flipping process would be ascribed to a soliton being moved along the chain direction. A soliton is a domain wall boundary between uniformly magnetized chain segments, and its lattice has been determined to be entropy driven, giving rise to incommensurate diffraction peaks in the SDW phase [55].

An additional energy scale is observed at low frequencies below 3.5 T indicating change in behavior. The contribution from this additional scale is very obvious around B_{dc} where to understand from quantitative viewpoint additional low frequency measurements and analysis are required. Where as the field dependence of $f_{\max}$ can still be tracked which is observed as a shoulder in every frequency scans and developing a minimum at B_{dc}. Presence of two energy scales could be related with in-chain (intrachain) and in-plane (interchain) correlations. The in-chain correlations form large percolating clusters with characteristic frequencies considerably smaller than the in-plane ones.The individual fingerprint of in-chain correlated clusters are observed at higher frequencies due to week interchain couplings.

Currently it is not explicit on the nature of processes which impact the appearance of temperature independent dissipation maximum at B_∞. Since χ_0 is equation 5.1 also displays a maximum at this field (not shown), we can conjecture that B_∞ may simply reflect the maximum in the total number of dynamic clusters. Although the unusual frequency dependence with crossover from dynamic to static regime indicated by B_{dc} remains perplexing. Hence, it would be compulsive to measure at higher frequencies beyond 10k Hz limit where the temperature dependence of crossover frequency (figure 5.4) might exhibit a possible saturation at higher temperatures. In addition both $B = 0$ and $B = 3.5$ T susceptibilities are somewhat impermeable to the occurrence of LRO at T_{N} (figures 5.1), suggesting that the dynamic part is expanding into the paramagnetic regime. In principle, this may not be coincidental at all considering that the core of magnetic clusters is made out of single-chain segments which show intrachain correlations well above T_{N} [84–86].

5.3 Synonymous Slow Dynamics in CoCl$_2$·2D$_2$O and CoV$_2$O$_6$

Ac susceptibility measurements of CoCl$_2$·2D$_2$O and CoV$_2$O$_6$ were carried out using a commercial Quantum Design MPMS3 AC option. In both samples ac fieldscans were performed across $\mathscr{T}_{\text{II}}$ transition at different temperatures, with ac frequencies ranging from 0.9 to 991 Hz equally spaced in log scale. Every fieldscan has been smoothed using a moving average. Using a piece-wise polynomial fit differential susceptibility $\frac{dM}{dB}$ has been calculated at respective temperatures to compare with ac fieldscans as zero frequency limit.

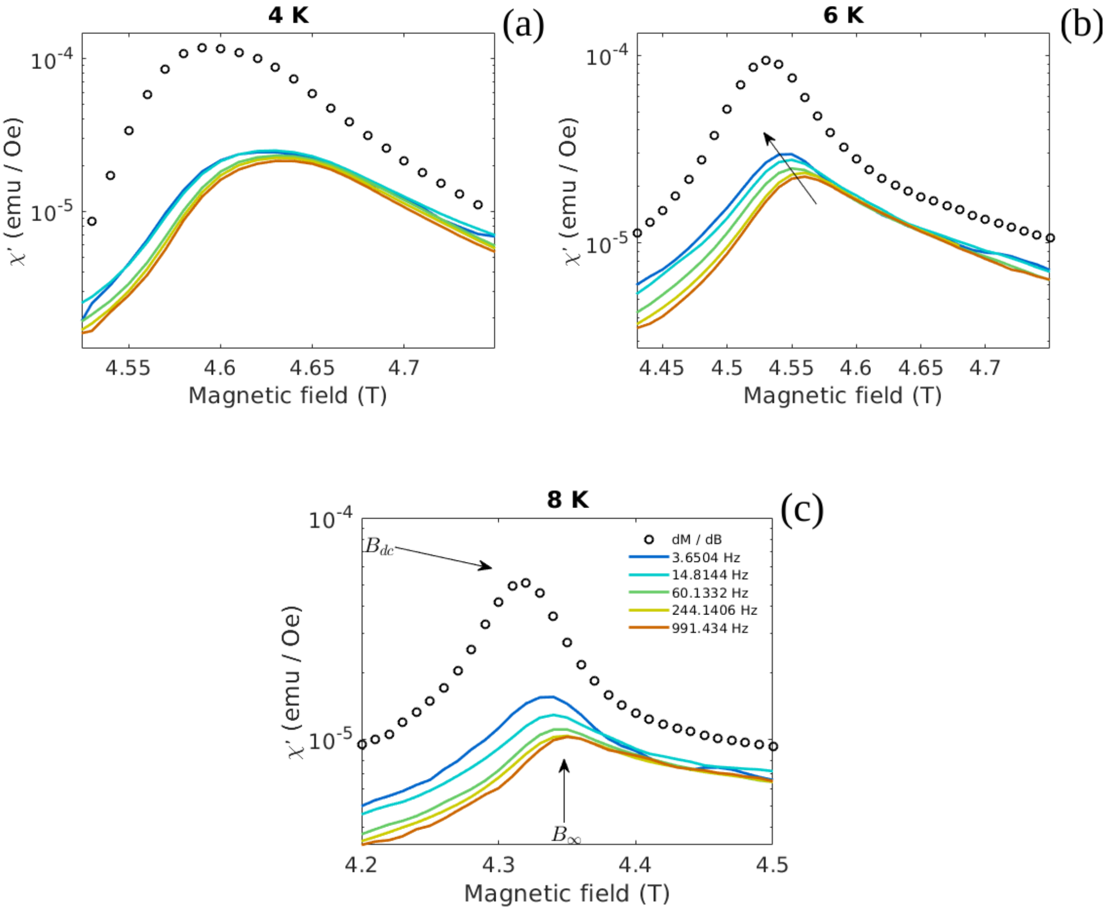

Figure 5.8 – Magnetic field dependence of ac susceptibility across $\mathscr{T}_{\text{II}}$ transition in CoCl$_2$·2D$_2$O. As opposed to Ca$_3$Co$_2$O$_6$, signatures of crossover region in frequency are not obvious in the measurement range. [left] χ' vs B at 4 K [middle] χ' vs B at 6 K. The arrow indicates drift of max(χ') towards lower fields with change in frequency [right] χ' vs B at 8 K. Characteristic features are denoted using arrows.

Field dependence of susceptibility in CoCl$_2$·2D$_2$O exhibit bell shaped curve skewed towards lower field region with a longer tail on the high field side. Unlike Ca$_3$Co$_2$O$_6$, the characteristic features observed are not that well-defined. Nonetheless one can denominate B_{dc} to max($\frac{dM}{dB}$) and B_∞ to max(χ') at 991 Hz, as shown in figure 5.8. With change in frequency a gradual trend is observed in shifting of max(χ') from B_∞ to B_{dc} without any evidence of a crossover region (figure 5.3). With change in temperature both B_{dc} as well as B_∞ shift towards lower fields. These attributes produce a major difference in the nature of susceptibility across $\mathscr{T}_{\text{II}}$ transition compared to $Ca_3Co_2O_6$.

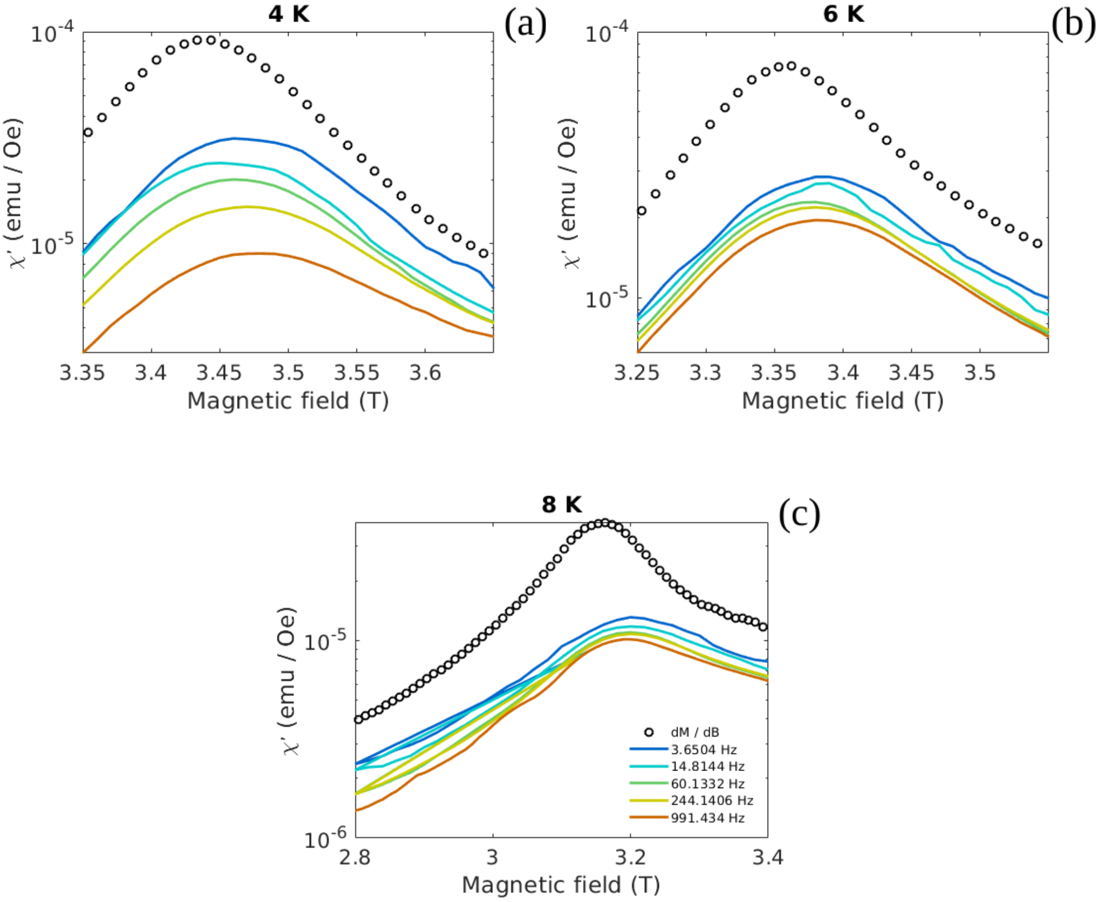

Figure 5.9 – Magnetic field dependence of ac susceptibility across $\mathscr{T}_{\text{II}}$ transition in CoV_2O_6. At all measured temperatures, with change in frequency, max(χ') doesn't alter away from B_∞.

Susceptibility across $\mathscr{T}_{\text{II}}$ transition in CoV_2O_6 exhibits similar behavior like in $CoCl_2{\cdot}2D_2O$. B_{dc} and B_∞ are observed to be distinct with a small separation. The position of max(χ') remains unaltered at B_∞ for a range of frequencies suggesting the possibility of a crossover region at low frequencies. Based on these observations one can conjecture that crossover region at low frequencies exist only in CoV_2O_6 and not $CoCl_2{\cdot}2D_2O$. Even so additional measurements at frequencies below 1 Hz are imperative to conclude this speculation.

5.4 Comparison and Conclusion

Field-induced susceptibility measurements across $\mathscr{T}_{\mathrm{II}}$ transition in $CoCl_2 \cdot 2D_2O$ and CoV_2O_6 produce geometrically similar profile yet qualitatively different results compared to $\mathscr{T}_+$ transition in $Ca_3Co_2O_6$. In all the three samples position of $\max(\chi')$ shifts with frequency, which can be interpreted as a manifestation of slow dynamics. The major difference in character is seen when B_∞ remains constant and B_{dc} varies with temperature in $Ca_3Co_2O_6$. An immediate impact of this behavior can be visualized in figure 5.4 where crossover frequency spans three orders of magnitude for a relatively narrow temperature window. Where as in $CoCl_2 \cdot 2D_2O$ and CoV_2O_6 both the characteristic features remain temperature dependent.

In $Ca_3Co_2O_6$ superparamagnetic behavior is already established from previous experiments. Temperature dependence of susceptibility in the middle of $\mathscr{T}_0$ (zero-field) and $\mathscr{T}_+$ transitions provide sufficient evidence for this behavior. Magnetic relaxation of CoV_2O_6 nano crystals at 2K is observed to be spin-glass like freezing due to no geometrical frustration [87]. However, not much information is available on magnetic relaxation for CoV_2O_6 single crystals.

In $CoCl_2 \cdot 2H_2O$, thermoremanent magnetization measurements suggest spin-glass behavior with $\tau \simeq 210$ s, where a stretched exponential has been used to fit the time dependence [88]. Alternately, relaxation time has also been obtained from susceptibility measurements [89] which provides us with conflicting results. Debye-like function has been assumed and the relaxation time is estimated to be $\tau_{\mathrm{I}} > 10^{-3}$s and $\tau_{\mathrm{II}} \simeq 10^{-5}$s corresponding to $\mathscr{T}_{\mathrm{I}}$ and $\mathscr{T}_{\mathrm{II}}$ transitions respectively. The relaxation function at $\mathscr{T}_{\mathrm{I}}$ transition is assumed to be a generalized Debye function with a distribution of relaxation times. On the contrary, relaxation at $\mathscr{T}_{\mathrm{II}}$ transition has been described using a single Debye function. Debye-like behavior in this sample is observed at frequencies beyond 1 kHz.

Based on the available information, one can claim that the slow dynamics in CoV_2O_6 and $CoCl_2 \cdot 2H_2O$ are similar with possible spin-glass behavior. On contrary, superparamagnetic behavior is already well established in $Ca_3Co_2O_6$.

6 Endeavor for Microstructure Determination using Magnetic SANS

Magnetic SANS experiment was proposed on $Ca_3Co_2O_6$ in order to investigate the microscopic behavior observed in ac susceptibility measurements. Previously SANS measurements were carried out at zero-field to look for magnetic inhomogeneities at zero-field essentially in the middle of $\mathscr{T}_0$ transition [5].

6.1 Origin of Ferrimagnetic Nano-fluctuations at Zero-field

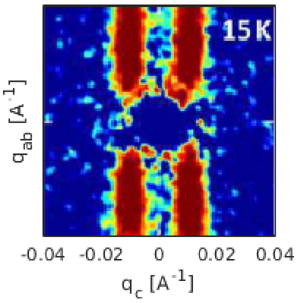

Figure 6.1 – SANS detector image obtained at zero-field. [Reused with permission from [5]].

In this section we shall briefly discuss the results and implications of the precursor experiment. The central idea was to uncover FiM nano fluctuations embedded inside SDW state at $T < T_N \simeq 25$ K. During the experiment, neutron beam was incident perpendicular to the *c*- axis of the crystal. For $T < T_N$, two parallel streaks running perpendicular to *c*- axis were observed as shown in figure 6.1. The scattering pattern remains unchanged on rotating the *c*- axis of the sample, implying isotropic correlations in *ab*- plane. On separating in-plane (q_{ab}) and along chain (q_c) components, the scattered neutron intensity $I(q)$ can be described as:

$$I(q) \propto \delta\left(q_c \pm \frac{2\pi}{d}\right)\frac{q_{ab}^2}{q_c^2}\int_0^\infty C_{ab}(r)\, J_0\,(q_{ab}r)r\,dr \tag{6.1}$$

where C_{ab} is the in-plane spin-spin correlation function. Purely exponential function $C_{ab}(r) \simeq \exp(-r/\zeta_{ab})$ was used to extract the temperature dependence of correlation length ζ_{ab}. Temperature dependence of correlation length deduced in *ab*- plane as well as along *c*- axis at different temperatures are shown in figure 6.2.

Qualitatively temperature dependence of ζ_c and ζ_{ab} show similar behavior. At 15 K the FiM regions extend $\simeq$ 5 inter-atomic distance in *ab*- plane and $\simeq$ 90 inter-atomic distances along *c*- axis. PDA phase is well ordered over long range whereas FiM nanofluctuations exhibit broad features and are distinct from the former. Temperature dependence of integrated intensities

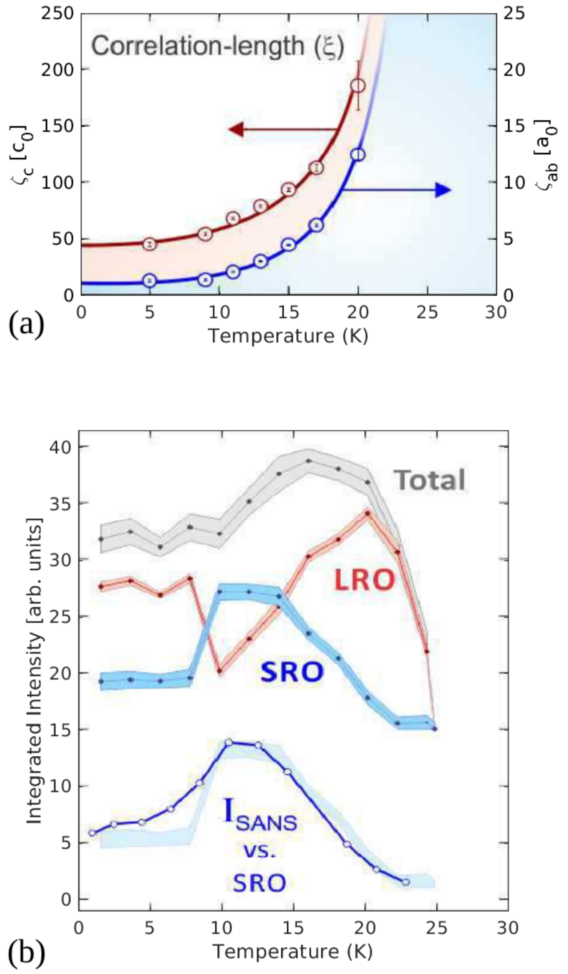

Figure 6.2 – Correlation lengths of SANS scattering ζ_{ab} and ζ_c. Neutron diffraction intensity of long-range order and short-range correlations. The short-range order in diffraction has a comparable T- dependence to the SANS intensity. [Reused with permission from [5]].

reveal competition between the two components, since FiM nanofluctuations exist at the expense of PDA state. Further, SANS intensity resembles susceptibility curves (figure 5.1a) substantiating superparamagnetic behavior [52].

6.2 Nano-phase Characteristics across $\mathscr{T}_+$ Transition

Here we describe the results of SANS measurements performed at non-zero field, which was carried out to investigate embedded phases across $\mathscr{T}_+$ transition.

6.2.1 Detector Images

Prior to the planned measurements, an experiment was carried out at 10 K 0 T to corroborate previous findings at this condition (figure 6.3a). Two parallel streaks have been observed perpendicular to the c- axis. Intensity of the streaks are not sharp as observed in figure 6.1. Measurements at 3.4 T (middle of $\mathscr{T}_+$ transition) generate single vertical streak passing through the center of the detector. Without altering the field, on increase in temperature single vertical streak is also observed at 11.5 K and 13 K with intensity diminishing considerably. At 16 K 3.4 T no considerable intensity was observed along the vertical streak and hence this data was used as background in our analysis.

Double lobbed profile characteristics in the horizontal direction away from center are due to dipolar interactions between neutrons and atomic moments. The center of detector image is mostly influenced by the direct beam. The horizontal streaks close to the center are due to reflections from aluminum cans and cryostat [90]. We have carefully excluded these background data during the analysis of scattered intensity.

6.2.2 Analysis of Scattered Intensity

Data from the detector images were binned to obtain the characteristic scattering profile along and perpendicular to the streaks. These profiles can be fitted with an appropriate model to extract the correlation length of nano-clusters along c- axis and in ab- plane. Lorentzian function was chosen to model the scattering profiles, whose functional form is given below,

$$I = I_0 + \frac{I_\mathrm{q}}{[(x - q_0)^2 + q^2]} \tag{6.2}$$

where q gives information on the width of distribution.

Data at 10 K 3.4 T could be described using equation 6.2 as shown in figure 6.4. Data at other temperatures lack intensity and need to be re-measured for sufficient statistics.

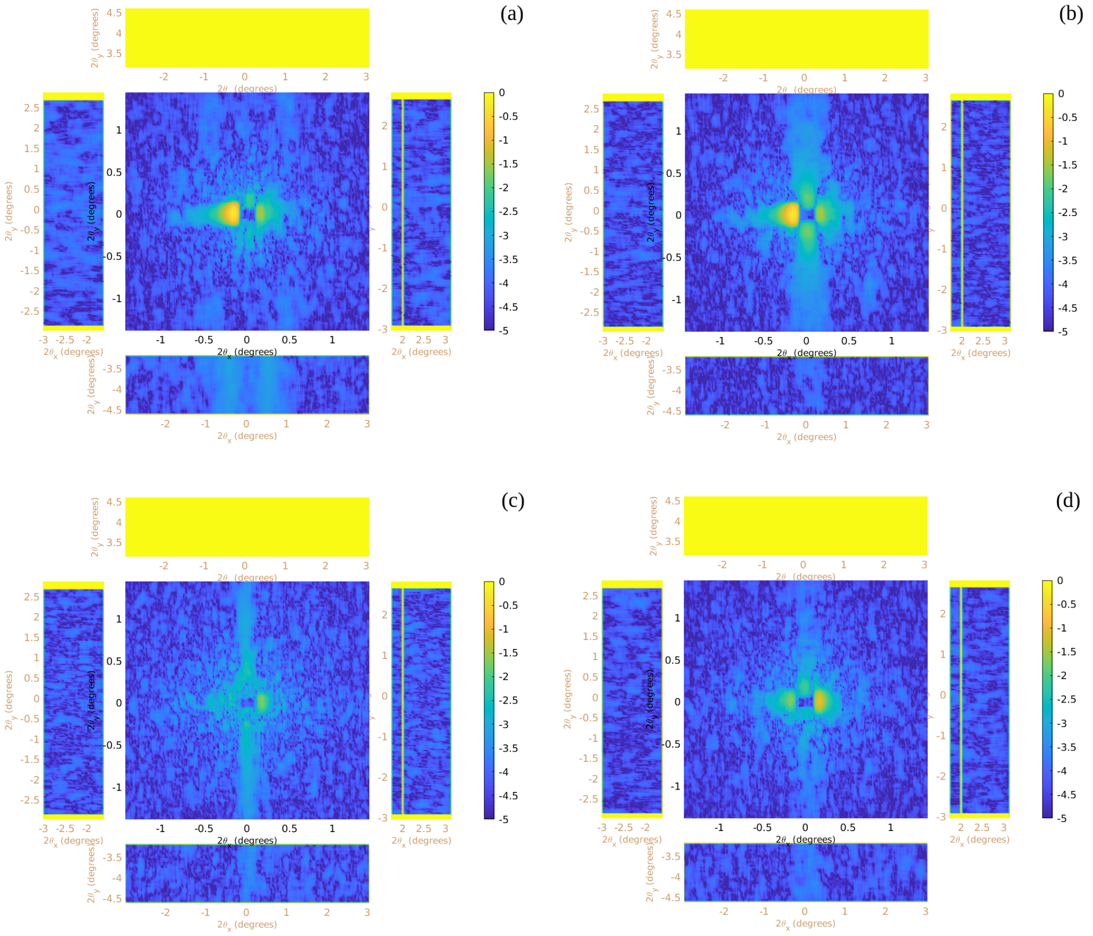

Figure 6.3 – SANS detector images obtained at different temperatures and magnetic fields (a) Detector image at 10 K 0 T. Two parallel streaks are observed as expected. (b) Detector image at 10 K 3.4 T. Single vertical streak is observed which passes through the center of the detector image. (c) Detector image at 11 K 3.4 T. Due to insufficient beam time we could not collect enough statistics at this temperature and field. (d) Detector image at 13 K 3.4 T. The vertical streak is still present. The intensity of this streak is lower than at 10 K.

6.3 Discussion and Conclusion

From this experiment our venture to determine $Ca_3Co_2O_6$ microstructure across $\mathscr{T}_+$ transition has not been fruitful due to insufficient statistics. Nonetheless, the available detector images have been utilized for qualitative comparison with the zero-field counterpart.

At zero field, two parallel streaks are observed perpendicular to c- axis, whereas at 3.4 T only a single streak is observed. With increase in temperature from 10 K to 13 K intensity of this streak decreases. At 10 K span of the streak along q_c is narrower close to the center of the detector. Away from the center, at higher q_ab the streak becomes wider (figure 6.4b). However, at 11.5 K and 13 K the streak appears to maintain constant width throughout q_ab.

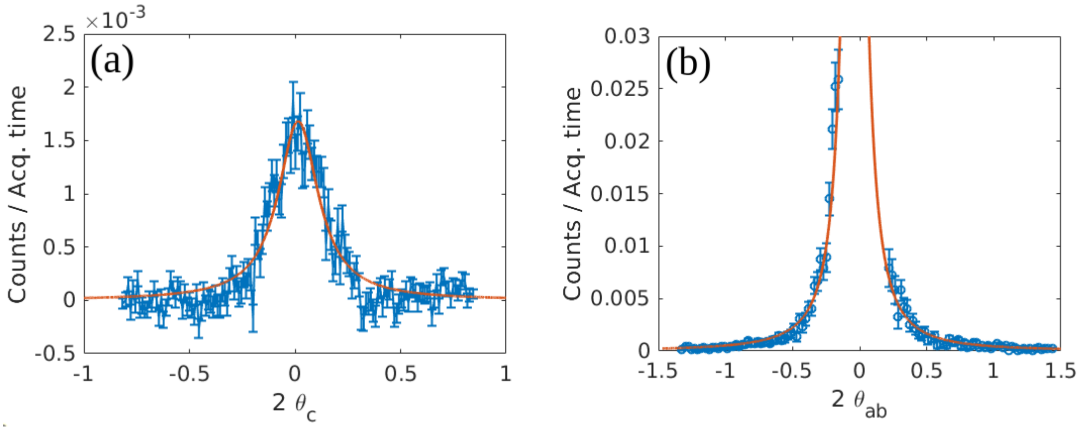

Figure 6.4 – Lorentzian function has been used to fit scattered intensity. (a) scattered intensity $\parallel c$- axis, $q_{\parallel c} \simeq 0.1162$. Higher order peaks couldn't be modeled due to poor quality of data. (b) scattered intensity $\perp c$- axis, $q_{\perp c} \simeq 0.06707$.

Scattered intensity along and perpendicular to the streak have been fitted using equation 6.2. From $\zeta \propto 1/d$ one can estimate that the nano-clusters expand $\simeq$ 8.5 interatomic distances along c directions and $\simeq$15 interatomic distances in ab- plane.

Unlike at zero-field, the occurrence of single vertical streak in the middle of $\mathscr{T}_+$ transition signifies the presence of only one phase without any competing components. Further, presence of two parallel streaks at zero-field suggests incommensurate structure where as in the middle of $\mathscr{T}_+$ there is only one streak implying a commensurate structure. From these viewpoints $\mathscr{T}_+$ can be regarded to be simpler than $\mathscr{T}_0$.

7 Search for Nano-fluctuations using Coherent Soft X-ray Scattering

Coherent soft x-rays can provide insights on magnetic order in materials. A perfectly ordered sample would produce well defined Bragg peaks. On the contrary a completely disordered structure would produce speckles between adjacent peaks. In an imperfect order speckles are observed between two well defined peaks. Analysis of speckle pattern will yield magnetic properties of the sample under study [75]. An example of calculating inter particle magnetic correlations in single domain Co nano particle system using resonant soft x-rays is discussed here [91].

Previously resonant x-ray scattering experiment on $Ca_3Co_2O_6$ was carried out by Mazzoli *et al* at non-zero field who had observed non trivial phase transition between iPDA and FiM states [92].

7.1 Experimental Details

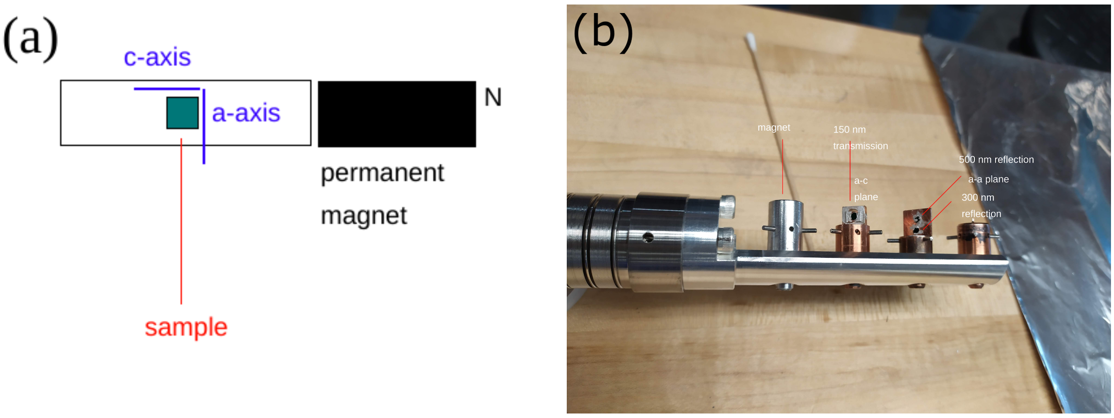
(a)
c-axis
a-axis
N
permanent magnet
sample
(b)
magnet
150 nm transmission
a-c plane
500 nm reflection
a-a plane
300 nm reflection

Figure 7.1 – A schematic of sample rod which is transferred into the chamber. Samples of different orientations are mounted as shown in the figure.

The aim of this experiment was to find diffuse scattering at different temperatures as well as obtain characteristics time scales. Also this would be a novel experiment on Ising-type systems, which hasn't performed before. A similar experiment (in reflection mode) on spiral AFM system has been previously performed by Chen *et al* [93].

The experiment was planned to be carried out in two modes, reflection in a-a plane and transmission through a-c plane with an objective to seek explanations behind origin of nano-fluctuations and coexistence of short and long range ordering previously reported in magnetic SANS experiments (refer figure 6.2) [5].

Due to experimental difficulties we could not obtain fruitful information from the experiment. As shown in figure 7.2 the observed temperature independent diffuse ring was likely due to ice formed in the chamber and magnetic component from L_3 edge was not evident in the detector image. No clear speckles were observed to reveal more information on the magnetic order in this material. The data hasn't be further analyzed.

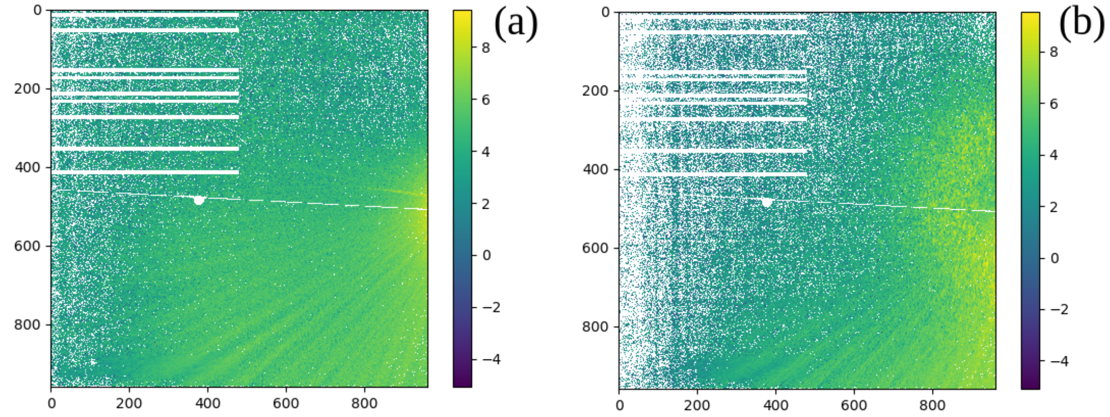

Figure 7.2 – Sample detector image in ac transmission mode at two different temperatures 10 K (< T_N) and 40 K (> T_N). A temperature independent diffuse ring is observed which could be likely from ice formed in the chamber.

8 Emergence of New Phase over $\mathscr{T}_0$ Transition in $Ca_3Co_2O_6$

The innate complexities in zero-field state of $Ca_3Co_2O_6$ has been well known over the past two decades from various experiments. Our current analysis on $\mathscr{T}_0$ transition provides more insight into the dynamics of the transition rather than the zero-field state itself, thereby shedding light on unexplored territory of the field-temperature phase space.

8.1 Initial Observations from Magnetization Measurements

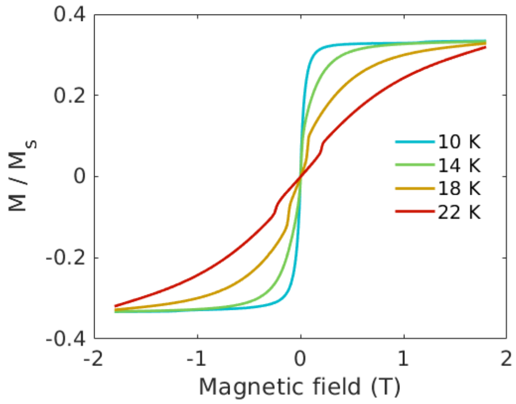

Figure 8.1 – Magnetization fieldscan profiles across $\mathscr{T}_0$ transition. Around 10 K the transitions are sharp; with increase in temperature they broaden. Above 14 K two metamagnetic transitions occur at symmetric non zero-field. An intermediate phase emerges in-between the two transitions.

Field-induced magnetization measurements were carried out across $\mathscr{T}_0$ transition as shown in figure 8.1. Around 10 K metamagnetic transitions occur with a spin flip between ↑↓↓ and ↑↑↓ states. For $T > 14$ K $\mathscr{T}_0$ transition is dissected into two transitions above and below zero-field creating an intermediate phase in-between. This can be schematically presented as,

$$\uparrow\uparrow\downarrow \longrightarrow \text{intermediate phase} \longrightarrow \uparrow\downarrow\downarrow \tag{8.1}$$

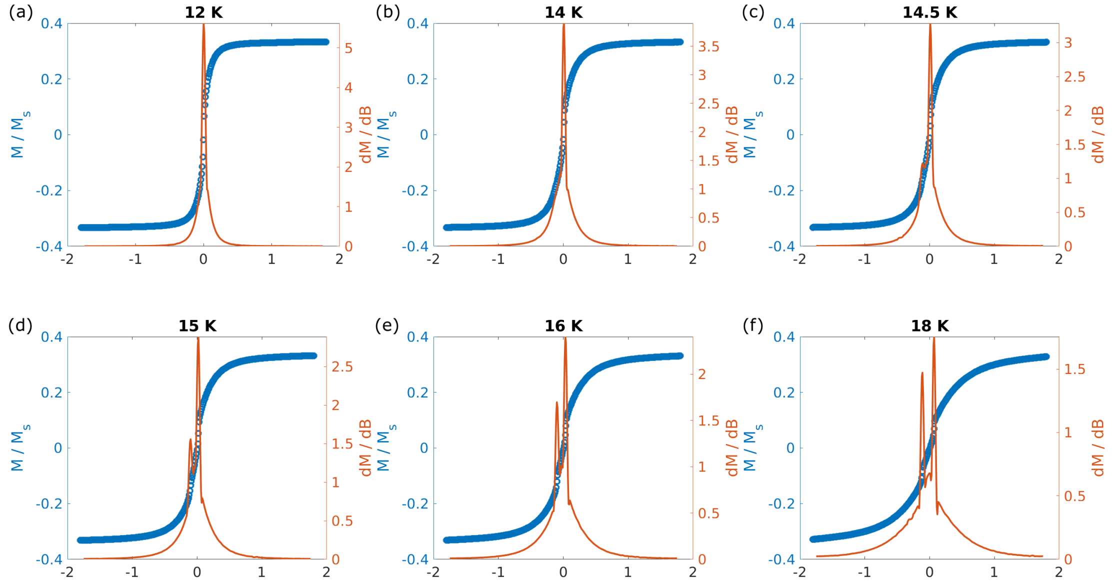

Figure 8.2 – Over-plot of magnetization fieldscan and corresponding differential susceptibility across $\mathscr{T}_0$ transition to visualize emergence of intermediate phase. At $T > 14$ K max($\frac{dM}{dB}$) shifts to a non-zero positive field value and an additional peak appears at negative field value in $\frac{dM}{dB}$ profile. The transitions move further away from zero-field with subsequent increase in temperature.

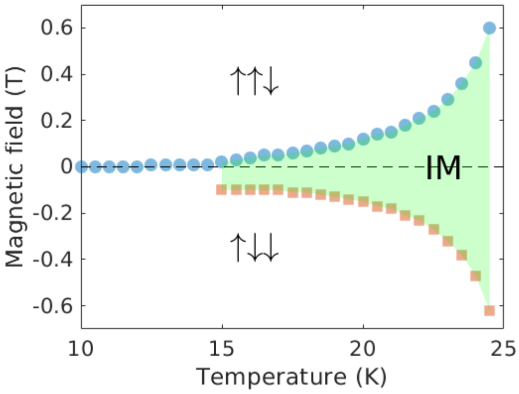

Figure 8.3 – B-T phase diagram of $\mathscr{T}_0$ transition in $\mathrm{Ca_3Co_2O_6}$. At low temperatures a single phase boundary separates ↑↓↓ and ↑↑↓ spin states. The observed intermediate phase between two phase boundaries is shaded and denoted by IM. The system is in non-equilibrium state during magnetization measurements which has resulted in phase boundaries having an offset in field space. A horizontal dashed line is drawn along zero-field.

Our measurements were carried out with field sweep from +1.8 T to -1.8 T in DC mode. Due to long relaxation time, magnetization measurements capture the system in non-equilibrium state. With measurement time window being shorter than the relaxation time, the particles in intermediate phase are magnetically blocked. This results in lateral shift in the position of peaks in field space. This non-equilibrium effect was ensured from measurements carried out at higher sweep rate (10 Oe / sec and 100 Oe / sec) where shift in position of peaks were observed.

A B-T phase diagram is created, shown in figure 8.3. Reversing the field sweep during measurements would interchange the position of phase boundaries in the B-T phase diagram. If the measurements are performed slower than the relaxation time of the system, then the phase boundaries above and below zero-field would be symmetric and the multicritical point around 14 K could be accurately established.

8.2 Distinct Dynamic Features of Intermediate Phase

Ac susceptibility measurements were carried out to explore the dynamical characteristics of $\mathscr{T}_0$ transition as shown in in 8.4. From the dc fieldscan measurements we had encountered the emergence of an intermediate phase around 14 K.

At T = 10 K ac fieldscans exhibit single maximum at all frequencies. At highest measured frequency of 10^4 Hz, χ' exhibits a dip on either side of zero-field. With decrease in frequency this drop off seems less apparent.

At temperatures around 18 K high frequency measurements display atypical behavior. At this temperature the intermediate phase is already established in dc measurements. In ac fieldscans at high frequencies only one maximum is observed in χ' where as χ'' exhibits two maxima. The location of maxima in χ'' is concurrent to that of $\frac{dM}{dB}$. The nature of χ'' profile is unusual making it unclear to determine if this intermediate phase is an actual phase or a crossover. Bigger spin-clusters probed at low frequencies show wide features indicating crossover between ↑↓↓ (or ↑↑↓) and intermediate phase, where as smaller spin-clusters probed at high frequencies do not enter the intermediate phase, instead undergo ↑↓↓↔↑↑↓ transition.

With further increase in temperature to 22 K, the geometrical nature of χ' as well as χ'' appear more symmetric where spins are closer to equilibrium state compared to 18 K. At high frequencies numerous kinks are observed across χ' and χ'' exhibits wide features suggesting short range ordering.

The dynamics causing these unusual features are yet to be understood. Frequency dependent intermediate phase formation implies the presence of non-equilibrium states across $\mathscr{T}_0$ transition. In each plot $\frac{dM}{dB}$ has been included as low frequency equivalent for comparison.

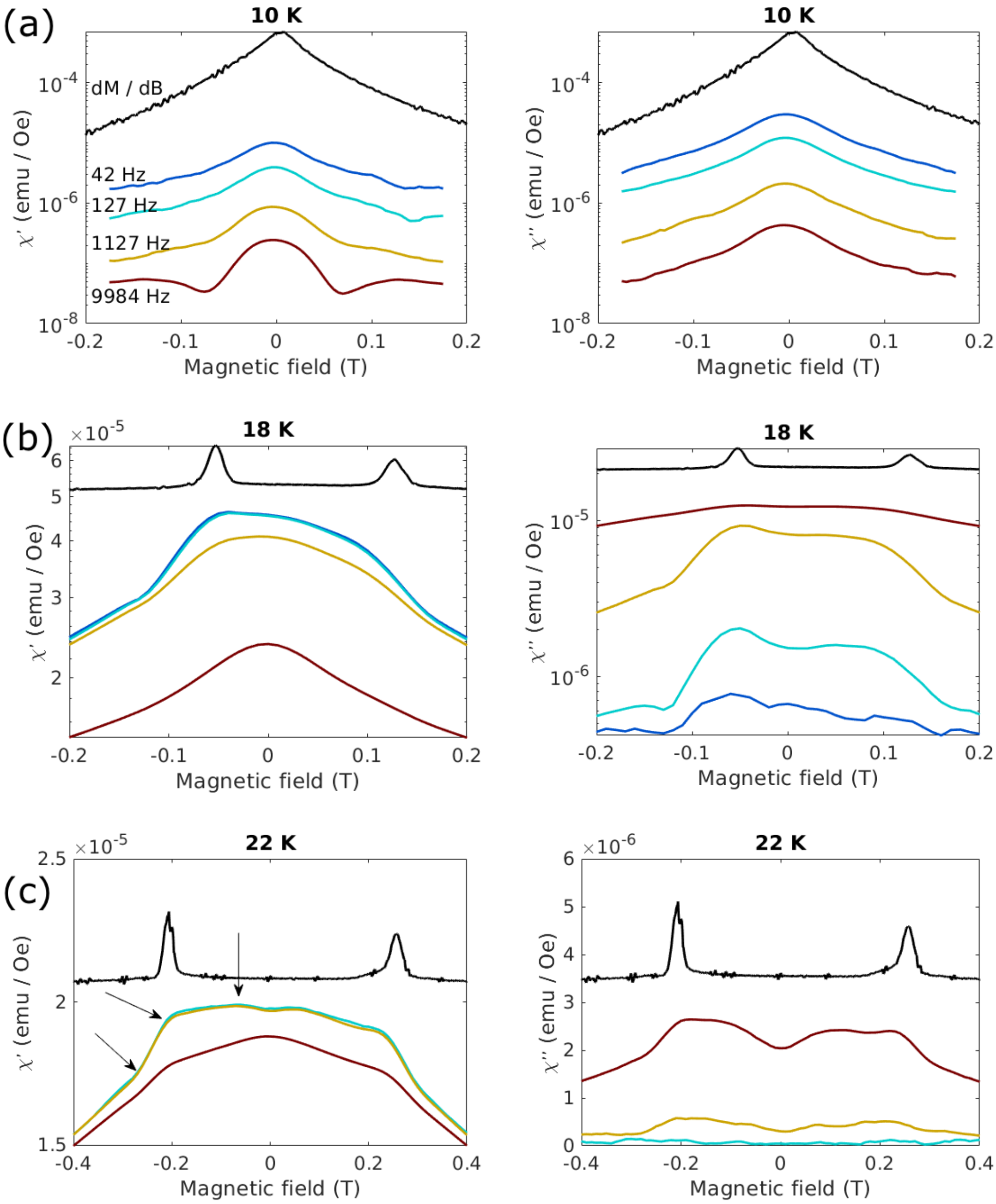

Figure 8.4 – Ac susceptibility fieldscans across $\mathscr{T}_0$ transition for T = 10 K, 18 K and 22 K. The individual fieldscans are smoothed using a moving average. At 18 K we can see that at low frequencies fieldscans are skewed depending upon the direction of measurement. However at high frequencies, only one maximum is observed. At 22 K several kinks are distinctly visible denoted using arrows. At different frequencies kinks are observed to happen at slightly different fields.

8.3 Thermomagnetic Hysteresis

Specific heat measurements were employed to investigate thermal effects and probe energy scales across $\mathscr{T}_0$ transition. As we already know the total specific heat (C_{total}) in a material includes contributions from lattice (C_{lattice}), electronic ($C_{\text{electronic}}$) and magnetic (C_{magnetic}) components. For a magnetic material C_{magnetic} is the quantity of greater significance which is obtained by taking the difference between C_{total} and C_{lattice}. By taking this difference, contributions from magnetic phases can be directly visualized. A standard plot of specific heat in an insulating magnetic material with ordering temperature T_N is shown in figure 8.5. Near T_N the trajectory of C_{magnetic} is usually an asymmetric peak (λ-type) for a continuous transition and delta function for a first-order. Logarithmic divergence has also been observed in many cases. Sample impurities or disorder can broaden the peak observed in C_{magnetic}.

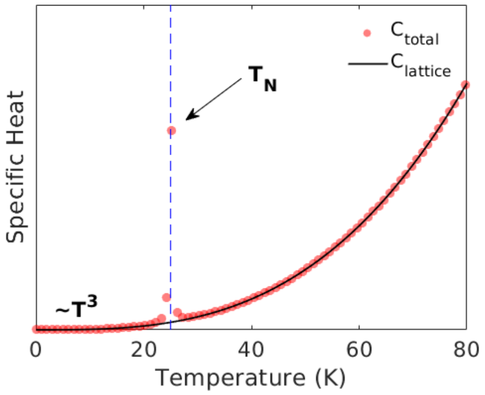

Figure 8.5 – A standard plot of temperature dependence of specific heat in an insulating magnetic material which orders at T_N. A vertical dashed line is drawn at T_N where C_{total} exhibits a peak or divergence. At low temperatures C_{lattice} obeys T^3 behavior in accordance with Debye model.

During measurements the sample was cooled down at -2 T (corresponding to -$M_s/3$) and temperature dependence of heat capacity was measured at different magnetic fields from -1 T to +1 T (every 0.02 T step). At every measurement, heat capacity was measured using long heat pulses of 50-80% which is at least five time rapid and more sensitive to first-order phase transitions [94]. Hysteretic behavior has been observed manifesting non-equilibrium states in the system.

At zero-field, temperature dependence of heat capacity exhibits a maximum at 24 K (T_N) indicating the origin of long-range ordering. With increase in magnetic field to 0.2 T, a shoulder is developed in heating cycle, and no such feature during cooling until 0.3 T. With increase in magnetic field, this feature propagates towards T_N. The difference in propagation of this feature in heating and cooling cycles is the primary evidence for thermomagnetic hysteresis. At higher fields the peak height of this broad feature is greater than the existing peak at T_N. Beyond 0.7 T this feature tends to merge with the peak at T_N in both heating and cooling cycles

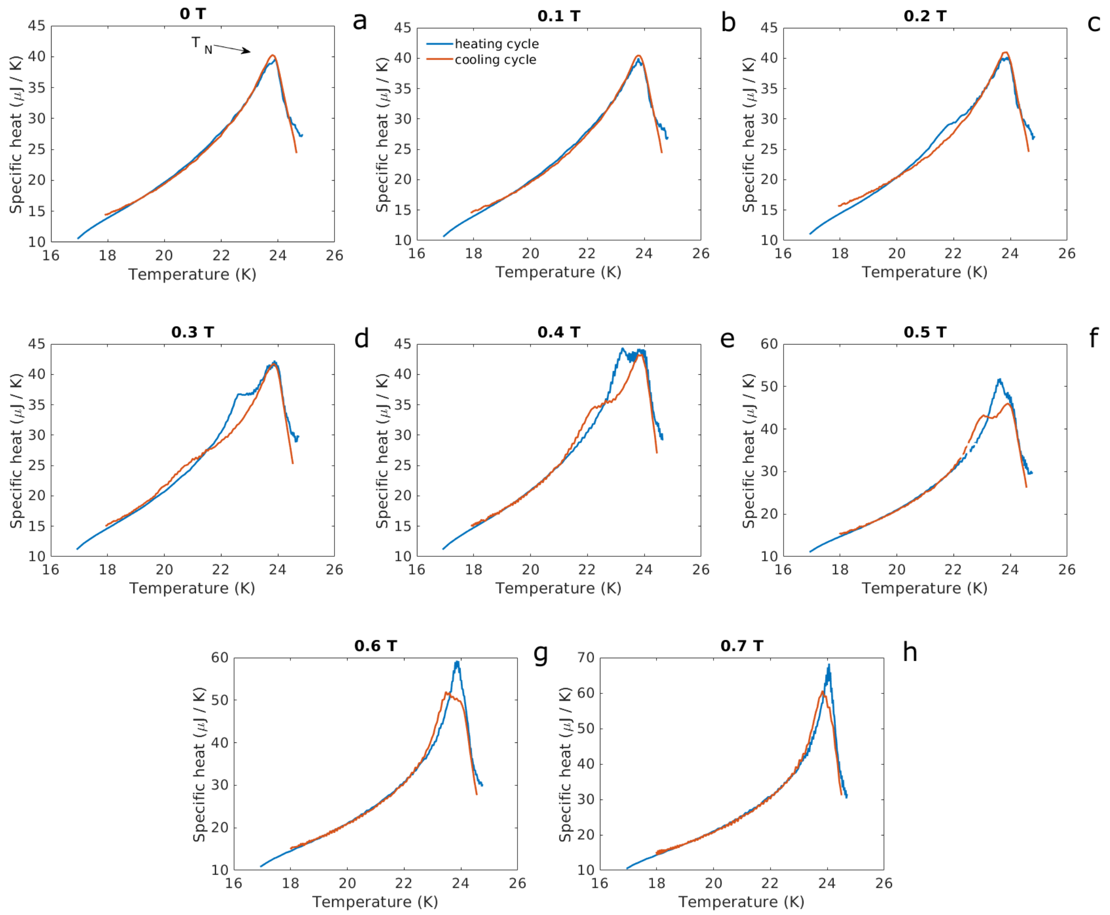

Figure 8.6 – Temperature dependence of heat capacity during heating and cooling cycle are shown for selected fields. A peak is observed at T_N indicated in the figure. Thermomagnetic hysteresis is observed at non-zero magnetic fields between ± 0.2 T and ± 0.7 T.

and no significant hysteretic behavior is observed hereafter.

The origin of this broad feature is likely due to short range effects in the energy scale indicating the presence of magnetic clusters or domains developed along the chains. These short range effects propagate towards T_N with increase in the field, complementing the trajectory of phase boundaries in B-T phase diagram (refer figure 8.3). At higher fields this feature becomes narrower and sharper indicating increasing presence of medium and long range effects in energy scale.

Colorplots of heating and cooling cycles of heat capacity (figure 8.7), where each temperature dependence is normalized to unity, are plotted to establish the hysteretic behavior. The hysteresis between heating and cooling cycle is well reflected in the contours. Heat capacity measured with subsequent magnetic field change from -1 T to 0 T and 0 T to +1 T show no qualitative difference in character.

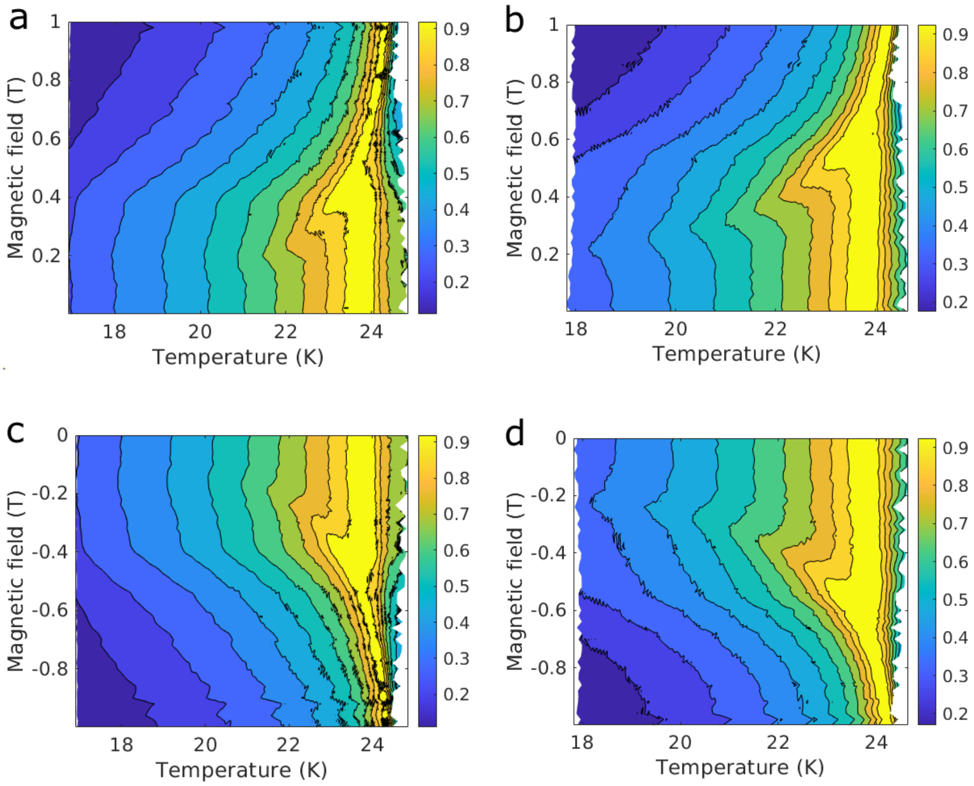

Figure 8.7 – Color plots of specific heat in temperature-field phase space around zero-field. Specific heat measured during heating cycle are displayed on left and cooling cycle on right. Broad features and thermomagnetic hysteresis between heating and cooling cycles are evident from the contour lines.

8.4 Discussion and Conclusion

Previous study by Agrestini *et al* [59] had reported on a slow order-order transition between high temperature spin density wave (SDW) and low temperature commensurate antiferromagnetic (CAFM) phases at 12 K in zero-field. It has been observed that this transition is reflected in zero-field cooled magnetization (M_{zfc}) of $Ca_3Co_2O_6$ single-crystals where for $12\text{ K} < T < 25\text{ K}$ M_{zfc} exceeds M_{fc} [95], as well in other unique time dependent observations like slow magnetization relaxation [57] and frequency dependence of susceptibility. Neutron scattering patterns along c-axis also confirm this transition where a single Gaussian is observed at 12.3 K indicating a single unit cell for CAFM phase while two Gaussians are observed at 14.1 K with larger unit cell representing SDW phase [56, 57].

Field-induced magnetization measurements across $\mathscr{T}_0$ provides additional insights for SDW-CAFM transition. If the measurements were performed quasi-statically then the multi-critical point around 14 K or possibly at lower temperature would be observed at SDW-CAFM transition. However, the intricacies and dynamics heterogeneity observed in ac susceptibility and specific heat measurements would make it difficult to determine the exact nature of

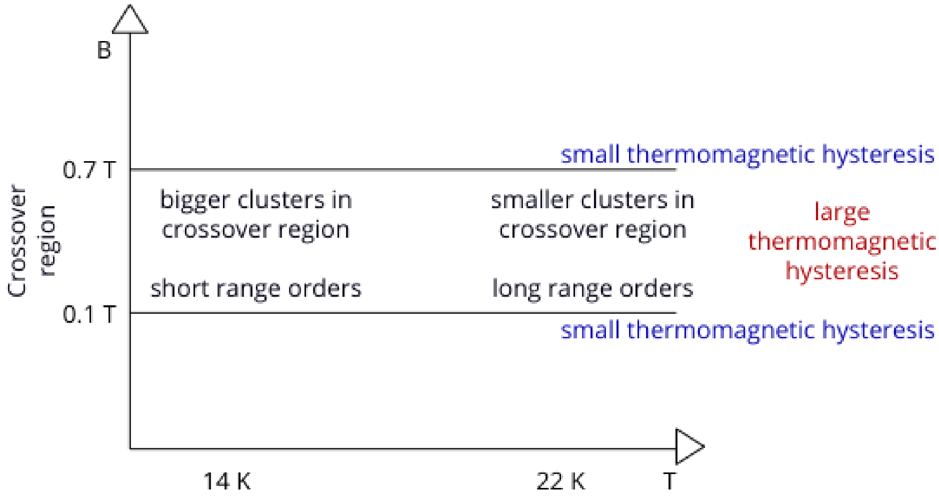
B
0.7 T
0.1 T
Crossover region
small thermomagnetic hysteresis
bigger clusters in crossover region
short range orders
smaller clusters in crossover region
long range orders
large thermomagnetic hysteresis
small thermomagnetic hysteresis
14 K
22 K
T

Figure 8.8 – Taken together the behavior of intermediate phase probed from ac susceptibility and specific heat measurements are summarized in this schematic. The findings related to intermediate phase which exists in the crossover region between two well defined states are mainly focused.

this intermediate phase, or even to proclaim if this intermediate phase is simply SDW phase reported previously.

The dynamical aspects of this intermediate phase can be visualized with an interplay between ac susceptibility and specific heat measurements. Ac susceptibility measurements at 18 K indicate crossover phase at low frequencies but no intermediate phase at high frequencies, indicating that bigger spin-clusters go undergo crossover but not smaller spin-clusters. With increase in temperature to 22 K we can notice that smaller spin-clusters also participate in crossover phase. One can also think of another possibility where at low temperatures there are only bigger clusters and with increase in temperature they disintegrate into smaller ones. In specific heat measurements The broad feature observed becomes narrower at high temperatures. An oversimplified picture from these observations would suggest that in the crossover region at low temperatures bigger spin-clusters are noticed with short range effects where as higher temperatures smaller spin-clusters dominate with medium and long range effects as shown in this diagram (figure 8.8). The actual structure is more complicated due to observed thermomagnetic hysteresis (figure 8.6), indicating non-equilibrium processes in these spin-clusters.

Due to long relaxation times magnetization measurements at slower ramp rate probe the system in non-equilibrium state. When measured using ac susceptibility measurements at different frequencies we observe there is discrepancy in the behavior at low and high frequencies. The system doesn't behave uniformly up to the characteristic resonance frequency. This suggests that the intermediate phase is a short range ordered meta phase and not a thermodynamic phase.

Since the occurrence of intermediate phase is frequency dependent in ac susceptibility, in principle, Widom lines can be drawn to establish the phase boundary. These lines are defined as locus of maximum correlation length, usually representing an extension of 'hard' phase boundary beyond the critical point [96, 97]. The sharp transitions observed in $Ca_3Co_2O_6$ may be seen as a transition between two phases in a quasiparticle, for example, a soliton. Incommensurate modulation of Ising chain in $Ca_3Co_2O_6$ has been understood within soliton theory [98], where the domain wall boundary consisting of solitons separate two commensurate segments of up and down spins [60]. Analogy with pressure-volume phase diagram (figure 8.9) is useful in understanding the crossover region. In the pressure-volume phase diagram below the critical point, at low pressures, there exists an intermediate phase between liquid and vapor, whereas above critical point distinction between the two phases is somewhat arbitrary. This is where Widom lines are drawn from response functions like specific heat C_p to identify subtle dynamic heterogeneities in the supercritical region. In general, for magnetic systems, field and temperatures are the sought-after control variables and change in magnetization is the order parameter. These entities take over the roles of pressure and volume (control variables), and change in density (order parameter) in the pressure-volume phase diagram.

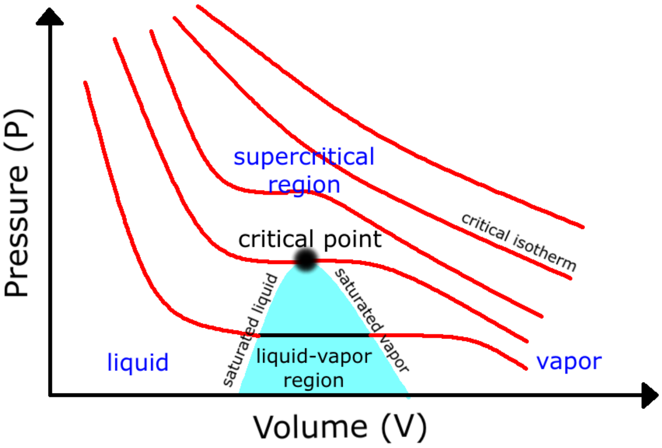

Figure 8.9 – Single component pressure-volume phase diagram. Near the phase boundary liquid, vapor and mixed (liquid-vapor) phases exist as shown in the diagram. The boundary of liquid-vapor region constitutes of saturated liquid and vapor. The region near and above critical point is the supercritical fluid, which in some ways is an arbitrary distinction. Higher temperature isotherms don't indicate a phase change since they are beyond the critical point. In the absence of 'hard' boundary, it may be possible to distinguish phases from a Widom line drawn from response functions, whose local maximum indicates the locus of this line.

In $Ca_3Co_2O_6$ Widom lines in the crossover region can be drawn to identify the discrepancy between well-defined $\pm 1/3 M_s$ states and the intermediate phase. But the response function (ac susceptibility), especially at higher temperatures do not display a maximum, instead a wider profile with several kinks. These factors make it more challenging to establish a Widom line from this technique. One can observe these complexities in ac susceptibility data at 18 K, where intermediate phase is attained mainly at low frequencies but not at higher ones. With increase in temperature it becomes more challenging to locate the extremum to draw Widom lines. The nature of multiple kinks in susceptibility profile at 22 K are not properly understood, which makes it difficult to establish a Widom line.

Magnetization measurements and differential susceptibility reveal the emergence of an intermediate phase around zero-field. With ac susceptibility measurements enunciating non-equilibrium states, and heat capacity measurements revealing thermomagnetic hysteresis, $\mathscr{T}_0$ transition exhibits rich properties. A cursory comparison of magnetization measurements across $\mathscr{T}_0$ and $\mathscr{T}_+$ transitions is sufficient to reveal that the essence of $\mathscr{T}_0$ and $\mathscr{T}_+$ transitions are fundamentally different with some notable differences. A prominent difference would be that at high temperatures across $\mathscr{T}_0$ transition an intermediate phase emerges, whereas in $\mathscr{T}_+$ a kink is developed. Surprisingly, the features of this intermediate phase across $\mathscr{T}_0$ is not well reflected in the SANS measurements at zero-field (figure 6.1) where no qualitative difference is seen in detector images at 11 K and 15 K [5]. Further analysis of ac susceptibility and heat capacity measurements are required to understand the dynamics of this new phase.

9 Summary

This study was set out to investigate universal aspects across metamagnetic phase transitions in frustrated ising chains. We decided on systems containing Co ion as magnetic site where large uniaxial anisotropy is present due to crystal field effects, thereby allowing treatment of magnetic ions in terms of large g-factor and effective spin-1/2 at low temperatures. Considering the simplicity in number of spin configurations and accessibility in local equipment, $Ca_3Co_2O_6$, CoV_2O_6 and $CoCl_2{\cdot}2D_2O$ were chosen for our studies, where all three samples exhibit $\uparrow\uparrow\downarrow \longleftrightarrow \uparrow\uparrow\uparrow$ transition.

For each sample magnetization measurements were performed at several temperatures up to respective T_N. In all samples at low temperatures multiple plateaus are observed and at high temperatures these plateaus smear out due to thermal fluctuations. From the B-T phase diagrams it has been established that all three samples exhibit unique and diverse magnetic properties. Here we summarize some notable observations from our experiments and analysis.

Metamagnetic transitions in $Ca_3Co_2O_6$ traverse through zero-field which is not the case in CoV_2O_6 and $CoCl_2{\cdot}2D_2O$. In $CoCl_2{\cdot}2D_2O$ $\mathscr{T}_\mathrm{I}$ and $\mathscr{T}_\mathrm{II}$ transitions terminate with a multicritical point, where as in CoV_2O_6 $\mathscr{T}_\mathrm{II}$ vanishes into a supercritical region. In $Ca_3Co_2O_6$ at sufficiently high temperatures (below T_N) as well in $CoCl_2{\cdot}2D_2O$ ($T > T_\mathrm{MC}$), a kink is developed within the transition. This kink is absent in CoV_2O_6 and intrinsic disorder is believed to be one possible reason. In $Ca_3Co_2O_6$ a sudden decrease in $\frac{dM}{dB}$ below 10 K indicates development of a different energy scale in the system. This is also observed for $CoCl_2{\cdot}2D_2O$ where $\frac{dM}{dB}$ drops abruptly at low temperatures for $\mathscr{T}_\mathrm{I}$ but not observed for $\mathscr{T}_\mathrm{II}$ which is puzzling. On contrary in CoV_2O_6 we don't observe this disparity in energy scales at low temperatures.

Each sample exhibits seemingly different characteristics in magnetization profile across $\uparrow\uparrow\downarrow \longleftrightarrow \uparrow\uparrow\uparrow$ transition. But the initial and final states across this transition remains the same, which suggest universal behavior. Using the approach of data collapse we tried to establish if there exists a scaling behavior between the three samples. Data collapse was performed at $\uparrow\uparrow\uparrow$ state since this is well defined in all samples. During this analysis magnetization profile of one sample was fixed at a particular temperature and that of another sample was compared at different temperatures. Considering the best case a scaling diagram was generated as shown in figure 4.19.

The dynamical aspects of $\uparrow\uparrow\downarrow\longleftrightarrow\uparrow\uparrow\uparrow$ transition were studied from ac susceptibility measurements. Due to its complex structure $Ca_3Co_2O_6$ exhibits rich behavior in ac susceptibility measurements across this transition. Temperature scans of ac susceptibility verify the superparamagnetic-like nature in this material. Using the relaxation models developed for superparamagnetic systems (refer appendix C), frequency dependent behavior in ac susceptibility was analyzed to obtain information on relaxation time and size of energy barriers across the $\mathscr{T}_+$ transition. Ac susceptibility measurements were also performed across $\mathscr{T}_{\text{II}}$ transition in CoV_2O_6 and $CoCl_2{\cdot}2D_2O$ where a distinction between B_{dc} and B_∞ is seen but the crossover frequency may exist beyond the range of measured frequencies.

Magnetic SANS measurement was performed on $Ca_3Co_2O_6$ in the middle $\mathscr{T}_+$ to probe the magnetic nano-clusters. Only long-range correlations seem to exist contrary to the zero-field case where both long-range and short-range orders co-exist. The data wasn't further analyzed due to inadequate statistics.

Field-induced magnetization measurements across $\mathscr{T}_0$ transition in $Ca_3Co_2O_6$ reveal an intermediate phase providing a new insight to SDW-CAFM order-order transition. Ac susceptibility data display sharp features instead several kinks are observed indicating crossover between FiM and intermediate state. Thermomagnetic hysteresis reflects non-equilibrium behavior in the system. These measurements suggest the presence of bigger clusters and short range ordering around 14 K whereas smaller clusters and long range orders become significant around 22 K.

Insights and motivation for future measurements are provided in the next chapter.

10 Outlook

Universality in dynamical systems has been one of the prominent aspects of critical phenomena. This has been well established in continuous phase transitions but not envisioned in first-order due to finite correlation length. Metamagnetic phase transitions in frustrated Ising chains display remarkable similarities despite seemingly different material specific behavior governed by internal processes. An exclusive study on these transitions hasn't been performed before despite a lot of attention had been being given to metastable plateaus in the past. This was the primary motivation for us to explore universal aspects of these transitions in this project.

In our measurements all the three samples that we investigated display plethora of unusual behaviors which are less understood. Although zero-field state of $Ca_3Co_2O_6$ was well studied in the past, field-induced magnetization measurements reveal an intermediate phase which hasn't been properly explored. Observations in ac susceptibility and thermomagnetic hysteresis in specific heat are yet to be thoroughly analyzed and interpreted. Another new feature is the presence of kink in $\mathscr{T}_+$ transition whose origin is not known. Surprisingly this kink is also seen in $\mathscr{T}_{\mathrm{III}}$ transition of $CoCl_2{\cdot}2D_2O$ but not in CoV_2O_6. $\mathscr{T}_{\mathrm{II}}$ transition in CoV_2O_6 ends prematurely into a supercritical region. Measurement of response functions like ac susceptibility or specific heat will be useful for a better understanding of the crossover between $\uparrow\uparrow\downarrow$ and $\uparrow\uparrow\uparrow$ in the supercritical region using Widom lines. Reasons for abrupt changes of energy scales in $CoCl_2{\cdot}2D_2O$ at different temperatures is not known. Low frequency ac susceptibility measurements on $Ca_3Co_2O_6$ are required to obtain clear information on additional energy scales developed in the middle of $\mathscr{T}_+$ transition.

Additional measurements that can assist in understanding these puzzling behaviors should also be considered in future. Due to experimental and technical difficulties we could not complete several experiments like SANS, coherent soft X-rays, thermal conductivity, transverse-field measurements across $\mathscr{T}_+$ transition in $Ca_3Co_2O_6$. These experiments have to be redone in the future.

We have tried to establish scaling of metamagnetic transitions via data collapse. Our observations are qualitative and a rigorous mathematical approach using a theoretical model or an analytical function is required to further process the scaling. Our approach of data collapse is performed away from critical region and hence 'universality' per se is not established. However, the metamagnetic transitions compared between the three samples display a degree of similarity approaching $\uparrow\uparrow\uparrow$ state and we have established universal behavior in this region for a range of temperatures in each sample.

Study of metamagnetic transitions goes beyond the relevance of condensed matter systems. For example, recently Lampo *et al* [99] have addressed the challenges in urban road network bottleneck and how to optimize the efficiency in urban transport systems. The congestion nodes in urban traffic where transitions between different congestion regimes are observed to be abrupt. The shape of "betweenness distribution", a path dependent measure of flow is claimed to be universal. These systems, although governed by different dynamics, may provide an inexact parallel perception of universal features in our systems.

A Linear Response Theory

For an arbitrary system in isolation the properties can be tested with a weak external perturbation. An assumption can be made such that the observable follows hamiltonian of isolated system but the states are influenced by external perturbation. If the generalized response d of such system is linear in the leading term with respect to a generalized force or stimulus f acted upon, then the approach in finding expectation value of the system using such assumption can be termed as linear response theory. These generalized forces are simply perturbations to the equilibrium state of the system. The response at an arbitrary time t is given as,

$$d(t) = \int_{-\infty}^{\infty} r(t-t')f(t')dt' \tag{A.1}$$

where $r(t-t')$ is the generalized response function (often termed as *susceptibility*). During a measurement there exists a problem of causality where the stimulus (at time t') and response (at time t) are recorded at different time [6]. To counter that one can make an assumption of causality,

$$r(t-t') = 0, \text{ for } t < t' \tag{A.2}$$

which can be mathematically implemented using a Heaviside step function.

This theory unveils the intimacy between time-dependent response functions and dynamical properties of system at equilibrium [100]. But this approach is valid only when the generalized force is small such that the non-linear effects are negligible.

Some examples of response functions are specific heat, susceptibility, isothermal compressibility etc. When the perturbation is time-dependent this results in response function to be time or frequency dependent too.

In a magnetic system application of a small external field (stimulus) will change the magnetization (response) with a linear response which is termed as susceptibility (χ), given by.

$$\mathrm{d}M = \chi\, \mathrm{d}H \tag{A.3}$$

A.1 Single Relaxation Time

Considering simplest case of magnetic relaxation in a material with single energy barrier and relaxation time, the time dependence of susceptibility can be described using an exponential relaxation function given by,

$$\chi(t) = \chi_0 \exp(-t/\tau) \tag{A.4}$$

where χ_0 and τ correspond to superparamagnetic (isothermal response) susceptibility and relaxation time respectively.

In real materials single relaxation time is rarely found and hence, in general, relaxation function is non-exponential. Here we will discuss on modeling non-exponential relaxation from ac susceptibility measurements which are reflected in their frequency dependence. This technique serves as a very useful tool since a large window of relaxation times can be explored just by altering the frequency of ac field.

A.2 Generalized Debye Model

Using the framework of linear response theory phenomenological methods are developed that can simulate the frequency dependence of susceptibility. Consider the simplest case where moments relax within a single time scale. Borrowing expressions from dielectric relaxation, complex susceptibility can be expressed using Debye model as,

$$\chi(\omega) = \chi_\infty + \frac{\chi_0 - \chi_\infty}{1 + i\omega\tau} \tag{A.5}$$

where χ_∞ corresponding to susceptibility of blocked (adiabatic response) is included additionally. This equation is simply Fourier transform of equation A.4.

Cooperative effects in real systems lead to complexities and it is accounted by introducing a phenomenological parameter α, which quantifies 'spread' of the distribution.

$$\chi(\omega) = \chi_\infty + \frac{\chi_0 - \chi_\infty}{1 + (i\omega\tau)^{1-\alpha}} \tag{A.6}$$

This particular model is known as Cole-Cole model. α can be associated with a distribution function (refer equation B.3 in appendix B),

$$g(\ln\tau) = \frac{1}{2\pi} \frac{\sin(\pi\alpha)}{\cosh[(1-\alpha)\ln(\tau_c/\tau)] - \cos(\pi\alpha)} \tag{A.7}$$

Cole-Davidson is another phenomenological model similar to Cole-Cole. In this model relaxation time (τ) has an upper limit. The functional form of this model can be expressed as,

$$\chi(\omega) = \chi_\infty + \frac{\chi_0 - \chi_\infty}{(1 + i\omega\tau)^{\beta}} \tag{A.8}$$

Although these models may well describe a system, there is no obvious physical basis. The goodness-of-fit of one model over another can only interpret that the characteristics of an actual relaxation function is similar to that model. Debye model can be extended for coexisting relaxation entities with different relaxation times. A generalized Debye model is given by,

$$\chi(\omega) = \chi_{\infty} + (\chi_0 - \chi_{\infty}) \int_{\tau_{\min}}^{\tau_{\max}} \frac{g(\tau)}{1+(i\omega\tau)} d\tau \tag{A.9}$$

where $g(\ln\tau)$ is the distribution of relaxation times. A distribution of relaxation times can also arise due to interactions between relaxing objects, which is outside the scope of this thesis.

A.3 Uniqueness Criteria

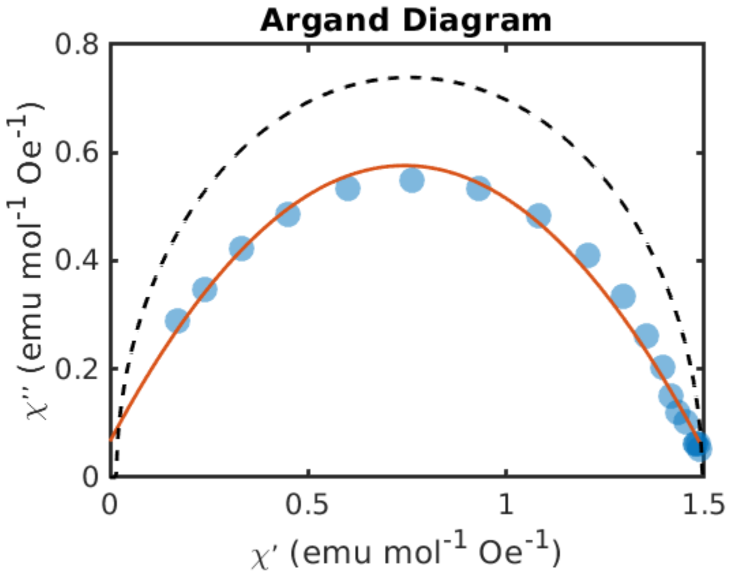

Figure A.1 – Argand diagram, of frequency dependence of susceptibility data for $Ca_3Co_2O_6$ at 15 K and 3.5 T, created using equation A.10. The blue dots are χ'' plotted as a function of χ' and the red line is the fit on the data. The black arc is the semi-circle which is expected when the system has single relaxation time.

A plot of χ' vs χ'' known as Cole-Cole plot or Argand diagram serves as a uniqueness criteria in choosing appropriate model to describe experimental data. In a physical system with single relaxation time the experimental data is in accordance with Debye model such that Cole-Cole plot is a perfect half-circle.

In a physical system with multiple relaxation times, Cole-Cole plot will manifest as a distorted half-circle. Depending upon the nature of relaxation time, Cole-Cole plot assumes different shapes. If the experimental data is in accordance with Cole-Cole model then a symmetric arc is observed. In case of Cole-Davidson model the Cole-Cole plot is seen as a non-symmetric arc. Hence the shape of arc will aid in choosing the right model to fit the data [6].

One can obtain the spread α using the relation between χ' and χ'',

$$\chi'' = -\left[\frac{\chi_0-\chi_\infty}{2}\tan\frac{\pi\alpha}{2}\right] \pm \sqrt{\left(\frac{\chi_0-\chi_\infty}{2}\tan\frac{\pi\alpha}{2}\right)^2 + (\chi'-\chi_\infty)(\chi_0-\chi')} \tag{A.10}$$

A distribution in particle size or inclusion of dipolar interactions will be immediately observed in argand diagram where the shape of arc deviates significantly from half-circle. If the energy barrier of particles are temperature independent then argand diagrams at different temperatures will collapse into a single curve [49].

If there are multiple energy scales in the system then the argand diagram exhibits multiple arcs. Considering relaxation times of each individual domains to be well separated the frequency dependent susceptibility can be de-convoluted to treat each channel separately.

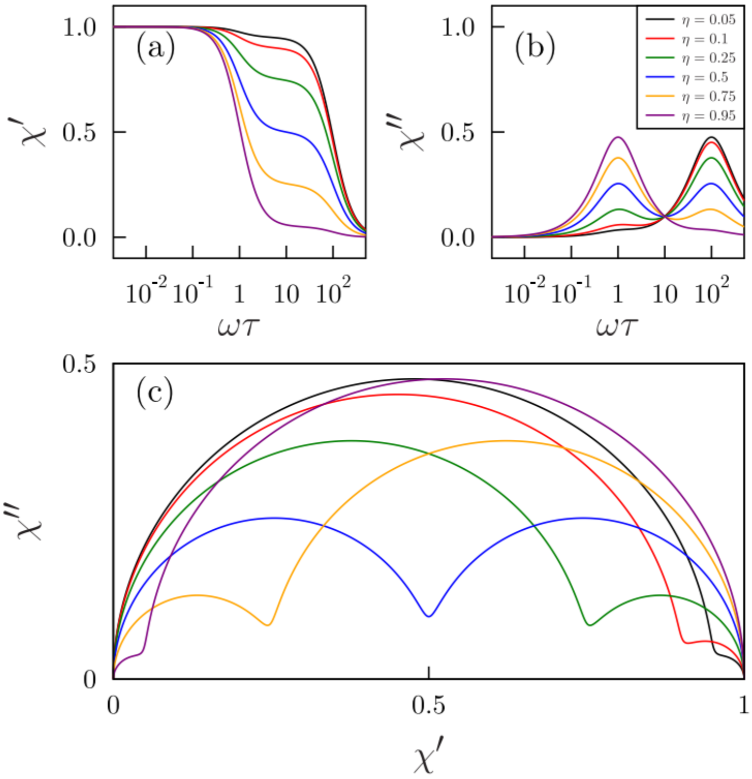

Figure A.2 – Frequency dependence of susceptibility with real (a), imaginary (b) parts. Using Cole-Cole equation susceptibility is modeled with $\tau_1/\tau_2 = 100$, plotted for various values of η (in our descriptions we have used the symbol α to quantify 'spread'). This plot is reused with permission from [6].

B Cole-Cole Distribution

Stieltjes transform can be used to extract the distribution function of Cole-Cole equation. The functional form of this transform is given below.

$$\begin{aligned} S_p(z) &= \int \frac{p(t)dt}{z-t}, x \in [-2,2] \\ p(t) &= \lim_{\epsilon\to 0} \frac{S_p(t-i\epsilon)-S_p(t+i\epsilon)}{2i\pi} \end{aligned} \tag{B.1}$$

This transformation can be used in a distribution function,

$$\mathrm{g}\,(\,\ln\tau\,) = \frac{1}{2\pi}\lim_{\epsilon\to 0}\underbrace{[\mathrm{Im}\chi_{\mathrm{cc}}(-\omega+i/\tau)-\mathrm{Im}\chi_{\mathrm{cc}}(-\omega-i/\tau)]}_{\text{imag.}} \tag{B.2}$$

Considering only the imaginary part of the equation

$$\begin{aligned} &\mathrm{Im}\ \chi_{\mathrm{cc}}(-\omega+i/\tau)-\mathrm{Im}\ \chi_{cc}(-\omega-i/\tau) \\ &=\mathrm{Im}\frac{1}{1+i(-\omega+i/\tau)^{1-\alpha}}-\frac{1}{1+i(\omega+i/\tau)^{1-\alpha}} \\ \\ &=\mathrm{Im}\ \frac{1}{1+e^{-i\pi(1-\alpha)(\tau_c/\tau)^{1-\alpha}}}-\frac{1}{1+e^{i\pi(1-\alpha)(\tau_c/\tau)^{1-\alpha}}} \\ \\ &\text{substitute } (\tau_c/\tau)^{1-\alpha}=a, \text{ and } \pi(1-\alpha)=b \\ &=\mathrm{Im}\ \frac{1}{1+ae^{-ib}}-\frac{1}{1+ae^{ib}} \\ &=\mathrm{Im}\ \frac{1}{1+a(\cos b-i\sin b)}-\frac{1}{1+a(\cos b+i\sin b)} \\ &=\frac{2(\tau_c/\tau)^{1-\alpha}\sin(\pi(1-\alpha))}{(1+(\tau_c/\tau)^{1-\alpha}\cos[\pi(1-\alpha)]^2+((\tau_c/\tau)^{1-\alpha}\sin[\pi(1-\alpha)]^2} \end{aligned}$$

On simplifying this equation using trigonometric and hyperbolic identities the distribution function can be expressed as below,

$$g(\ln\tau) = \frac{1}{2\pi}\frac{\sin(\pi\alpha)}{\cosh((1-\alpha)\ln(\tau_c/\tau)) - \cos(\pi\alpha)} \tag{B.3}$$

The geometric profile of Cole-Cole distribution function for different values of α $(0 < \alpha < 1)$ is shown in figure B.1.

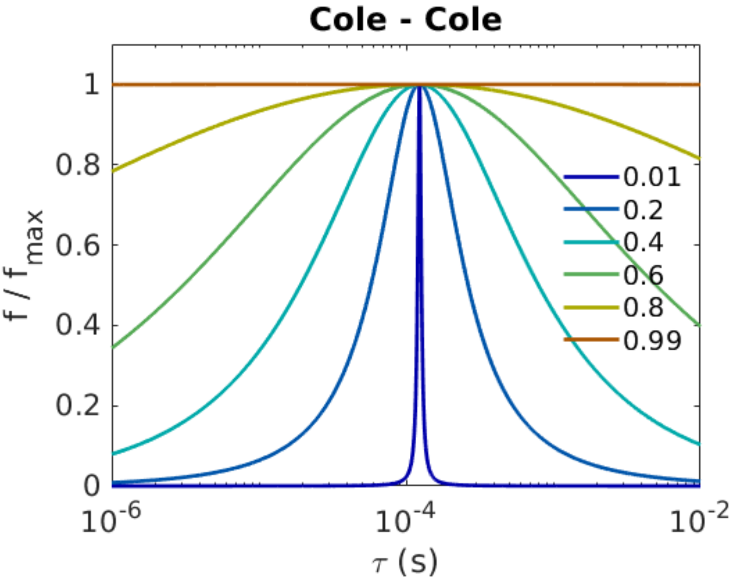

Figure B.1 – As we already know α is a measure of width of Cole-Cole distribution. For different values of α the distribution function is computed. At the lower limit $\alpha \rightarrow 0$, the system is close to having a singe relaxation time. Hence the distribution narrows down. For $\alpha = 0$, the distribution function is a dirac-delta. At the higher limit $\alpha \rightarrow 1$, the system has infinite width due to multiple relaxation times. In this comparison the mean relaxation time (τ_c) is assumed to be around 10^{-4} s.

C Superparamagnet Susceptibility

Here we use Gittleman model to obtain an analytical expression for susceptibility of non-interacting superparamagnetic or single-domain particles [101]. Other models for non-interacting superparamagnetic susceptibility developed by Khater *et al*, Kumar and Dattagupta are discussed here [47].

In an ac magnetic field $h = h_0 \sin(\omega\tau)$ time-dependent magnetization of a sample can be written as $M(t) = \chi_{\mathrm{ac}}(\omega, T)h(t)$. Corresponding ac susceptibility (χ_{ac}) in time-domain is expressed as,

$$\chi_{\mathrm{ac}}(t,\tau) = \chi_\infty + (\chi_0 - \chi_\infty)(1 - \exp(-t/\tau)) \tag{C.1}$$

where χ_∞ and χ_0 are susceptibility of blocked and unblocked particles in a superparamagnetic system. Fourier transform of equation C.1 yields,

$$\chi_{\mathrm{ac}}(\omega,\tau) = \chi_\infty + \frac{\chi_0 - \chi_\infty}{1 + i\omega\tau} \tag{C.2}$$

For a particle of volume V susceptibility of blocked and unblocked particles are given by [102],

$$\begin{aligned} \chi_0 &= \frac{\mu_0 M^2(V)V}{3k_B T} \\ \chi_\infty &= \frac{\mu_0 M^2(V)}{3K} \end{aligned} \tag{C.3}$$

Here K, termed as anisotropy barrier, is the measure of energy density of superparamagnetic particle whose magnitude depends upon temperature and composition. χ_0 is isothermal susceptibility related to spin-lattice relaxation time, and χ_∞ is adiabatic susceptibility related to spin-spin relaxation time. Usually energy exchange between spins is orders of magnitude faster than between spin and lattice.

K can be experimentally obtained from the difference between field-induced magnetization curves along easy and hard axes of a material [103],

$$K = \int_0^{M_\mathrm{s}} (H_\mathrm{eff}^\mathrm{hard} - H_\mathrm{eff}^\mathrm{easy})\, dM \tag{C.4}$$

where M_s is the saturation magnetization and H_eff is the effective field calculated after eliminating the demagnetization factor.

For a paramagnet at zero-field $\chi_0 = \chi_\infty$ [42]. On inserting the expressions of equation C.3 in C.2, an expression of susceptibility for a particle of volume V can be written as,

$$\chi_\mathrm{V}(\omega, T) = \left(\frac{\mu_0 M^2(V)}{1 + i\omega\tau}\right) \left[\frac{V}{3k_\mathrm{B}T} + \frac{i\omega\tau}{3K}\right] \tag{C.5}$$

For simulation and fitting experimental data this equation can be simplified by splitting into real and imaginary components.

$$\begin{aligned} \chi'_\mathrm{V}(\omega, T) &= \frac{\mu_0 M^2(V)}{3K} \left[\frac{KV}{k_\mathrm{B}T}\frac{1}{1+(\omega\tau)^2} + \frac{(\omega\tau)^2}{1+(\omega\tau)^2}\right] \\ \chi''_\mathrm{V}(\omega, T) &= \frac{\mu_0 M^2(V)}{3K} \left[\frac{\omega\tau}{1+(\omega\tau)^2} - \frac{KV}{k_\mathrm{B}T}\frac{\omega\tau}{1+(\omega\tau)^2}\right] \end{aligned} \tag{C.6}$$

Experimentally obtaining V is difficult. Hence activation energy E $(= KV/k_\mathrm{B})$ is directly used as a parameter in analytical calculations. Here we simplify this equation by substituting E for KV/k_B and A for $\frac{\mu_0 M^2(V)}{3K}$.

$$\begin{aligned} \chi'_\mathrm{V}(\omega, T) &= A \left[\frac{E}{T}\frac{1}{1+(\omega\tau)^2} + \frac{(\omega\tau)^2}{1+(\omega\tau)^2}\right] \\ \chi''_\mathrm{V}(\omega, T) &= A \left[\frac{\omega\tau}{1+(\omega\tau)^2} - \frac{E}{T}\frac{\omega\tau}{1+(\omega\tau)^2}\right] \end{aligned} \tag{C.7}$$

For particles with a distribution of volumes, using equation A.9 one can reformulate C.7 as,

$$\chi(\omega, T) = \int_0^\infty \chi_\mathrm{V}(\omega, T) f_\mathrm{V}(y)\, dy \tag{C.8}$$

where $f_\mathrm{V}(y)$ is a probability density function. To achieve this E is parameterized using a scaling relation $x = E/E_\mathrm{m}$, where E_m is the median activation energy barrier. For particles with a distribution of energy barriers, susceptibility can be written as,

$$\begin{aligned} \chi'(\omega, T) &= A_\mathrm{m} \int_0^\infty \left[\frac{E_\mathrm{m}}{T}\frac{x}{1+(\omega\tau)^2} + \frac{(\omega\tau)^2}{1+(\omega\tau)^2}\right] f_\mathrm{E}(x)\, dx \\ \chi''(\omega, T) &= A_\mathrm{m} \int_0^\infty \left[\frac{\omega\tau}{1+(\omega\tau)^2} - \frac{E_\mathrm{m}}{T}\frac{x\omega\tau}{1+(\omega\tau)^2}\right] f_\mathrm{E}(x)\, dx \end{aligned} \tag{C.9}$$

For non-interacting superparamagnets or single-domain particles relaxation time (τ) is given by equation 1.5.

$$\tau = \tau_0 \exp\Big(\frac{KV}{k_B T}\Big) \quad = \tau_0 \exp\Big(\frac{E}{T}\Big) = \tau_0 \exp\Big(\frac{E_\mathrm{m}}{T} x\Big) \tag{C.10}$$

On substituting this expression of τ, equation C.9 can be further simplified during computation. The mean activation energy barrier ($\bar{E}$) of a cluster can be calculated as follows:

$$\bar{E} = \int_0^\infty E\, f_\mathrm{E}(x) dx = E_\mathrm{m} \int_0^\infty x\, f_\mathrm{E}(x) dx \tag{C.11}$$

C.1 Probability Distributions

The choice of probability distribution depends upon the geometric nature of relaxation time distribution. From this one can extract statistical moments mean, variance and skewness which will provide us with a physical understanding of the nature of relaxation time in a material. Probability distributions like Gaussian or Lorentzian are widely used to describe phenomena in real materials. Frequency dependence of ac susceptibility can be well described using Cole-Cole distribution function (equation B.3).

Here we compare the characteristics of log-normal, Cauchy-Lorentz and Cole-Cole distribution functions. The functional forms of Lognormal and Cauchy-Lorentz are given below. τ_E and σ_E are the mean and variance of any distribution function.

$$\begin{aligned} \text{Lognormal} \;\; f_\mathrm{E}(x) &= \frac{1}{\sqrt{2\pi}\sigma_\mathrm{E} x} \exp\Big(-\frac{[\ln(x) - \ln(\tau_E)]^2}{2(\sigma_\mathrm{E})^2}\Big) \\ \text{Cauchy-Lorentzian} \;\; f_\mathrm{E}(x) &= \frac{1}{\pi \sigma_\mathrm{E} x \left(1 + \frac{[\ln(x)-\ln(\tau_E)]^2}{\sigma_\mathrm{E}^2}\right)} \end{aligned} \tag{C.12}$$

During the simulation or fit τ_E, σ_E, A_E are used as parameters. Temperature T is fixed since it is known. Ac frequency ω is the quantity w.r.t. the fit is performed. During the fit it is ensured that $\omega\tau = 1$ condition is satisfied at the maximum of $\chi''(\omega, T)$.

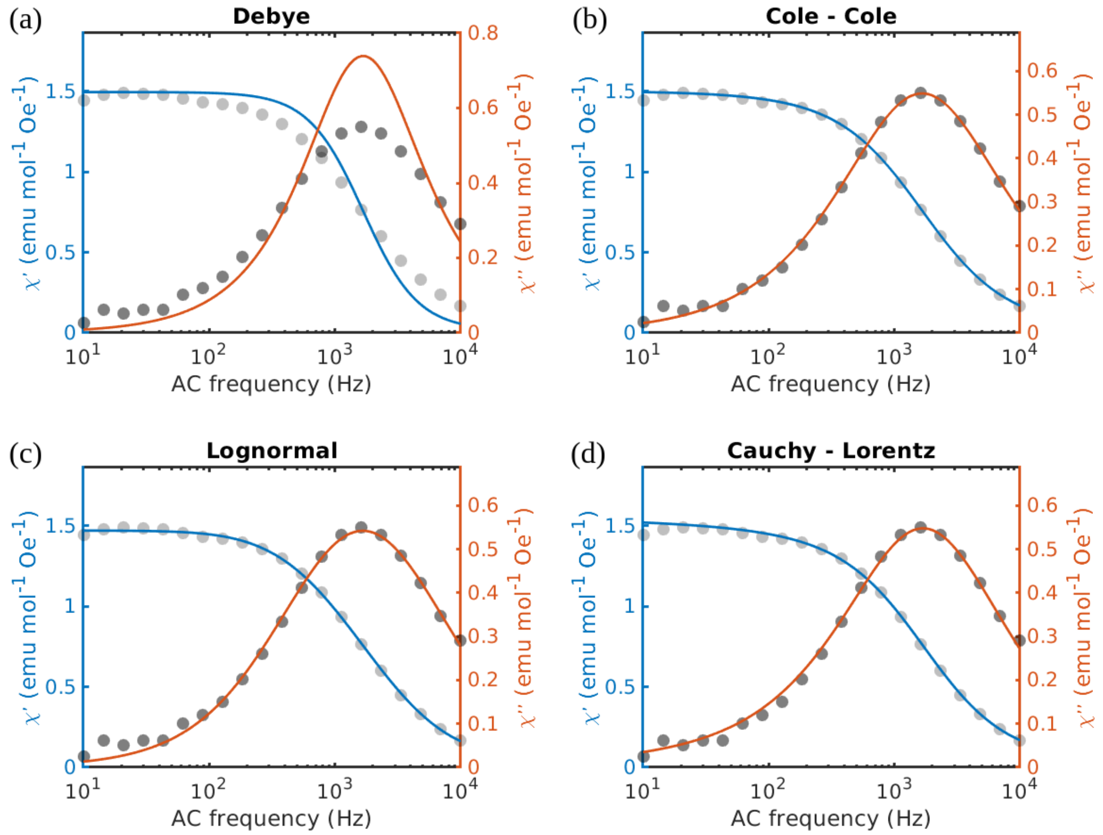

Figure C.1 – An example of modeling frequency dependence of susceptibility across $\mathscr{T}_+$ transition in $Ca_3Co_2O_6$. We have considered data at 15 K 3.5 T to show a comparison between different distributions used in generalized Debye model. The real part of susceptibility saturates and low and high frequency limits where as imaginary part displays a bell curve close to the mean relaxation time. (a) A fit was attempted using Debye model (without distribution function). The data can't be fitted using this model due to the existence of multiple relaxation times. Generalized Debye model has been employed to fit the data using (b) Cole-Cole (b) Lognormal and (d) Cauchy-Lorentz distribution functions. All the three distribution functions produce a good fit on the data, however based on goodness-of-fit test Cole-Cole distribution best describes susceptibility data for maximum number of reliable data set.

A brief comparison of different probability distributions that have been employed to describe frequency dependent susceptibility in $Ca_3Co_2O_6$ across $\mathscr{T}_+$ transition is shown in figure C.2. The susceptibility data was fitted using all three distribution functions using equation C.9 (figure C.1). Based on a cursory examination Cole-Cole and Cauchy-Lorentz display similar geometric behavior.

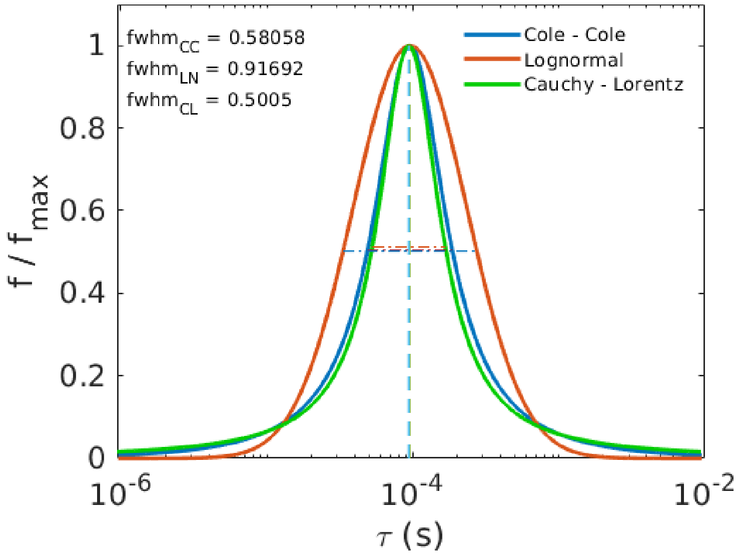

Figure C.2 – Comparison of Cole-Cole, Lognormal and Cauchy-Lorentzian distributions in $Ca_3Co_2O_6$ at 15 K 3.5 T. Cole-Cole and Cauchy-Lorentz distribution functions show very similar behavior with smaller width and longer curvatures around the mean relaxation time, compared to Lognormal distribution.

Frequency dependence of susceptibility analysis has been a useful tool to understand relaxation time and its temperature dependence in different materials. Parameters extracted from the fit like, attempt period (τ_0), energy barrier (E_B), its mean and variance obtained from the distribution function ($f_E(x)$) will be sufficient to paint a physical picture of the dynamical characteristics of a system. Further, this technique may be combined with remanent magnetization and/or Mössbauer spectroscopy to look for multiple energy scales.

D Code to Fit Superparamagnet Susceptibility

This chapter contains the Matlab code (version R2020a) that was used to fit frequency dependence of susceptibility on the basis of generalized Debye model. This code contains functions which have been implemented to fit real (χ') and imaginary (χ'') part of susceptibility simultaneously with shared parameters.

```
%% variables and parameters

% omega := ac frequency
% tauz  := mean relaxation time
% sigma := width of relaxation time
% Xz1   := susceptibility of unblocked particles
% Xinf1 := susceptibility of blocked particles

% initial values provided for parameters in the fit
sigma0 = 1e-1;
tauz0 = 1e-4;
Xinf0 = 1e-7;
Xz0 = 1e-5;
```

Using appropriate initial values are a must to obtain a good fit on the experimental data. In addition, optional fit parameters like weights, tolfun, tolX etc can be used to improve the fit. Examples of fitted experimental data has been shown in figure C.1.

```
%% function to compute real value of susceptibility

function RE = real(omega,sigma1,tauz1,Xinf1,Xz1)

sigma = sigma1*sigma0;
tauz = tauz1*tauz0;
Xinf = Xinf1*Xinf0;
Xz = Xz1*Xz0;

% defining the range of relaxation time used during fit
x = logspace(−5,−1,1e2);

% functional form of distribution function: cauchy−lorentzian ...
   distribution function have been used in this example which can be ...
   easilty replaced with cole−cole or lognormal distribution function
dist = @(x) 1./(pi.*sigma .* x .* (1 + ((log(x) − log(tauz))./sigma).^2));

% real part of susceptibility for single relaxation time
z = dist(x)./(1 + (2.*pi.*omega.*x).^2);

[n, ¬] = size(z);
re = [];
for i = 1 : n
x = logspace(−5,−1,1e2);
y = z(i, :);
idx = isnan(y);
x(idx) = [];
y(idx) = [];
re = cat(1, re, trapz(x, y));
end

% real part of suscptibility for a range of relaxation times
RE  = Xinf + (Xz − Xinf).*re;

end
```

```
%% function to compute imaginary value of susceptibility

function IM = imag(omega,sigma1,tauz1,Xinf1,Xz1)

sigma = sigma1*sigma0;
tauz = tauz1*tauz0;
Xinf = Xinf1*Xinf0;
Xz = Xz1*Xz0;

% defining the range of relaxation time used during fit
x = logspace(-5,-1,1e2);

% ensure that you are using the same functional form as in real part
dist = @(x) 1./(pi.*sigma .* x .* (1 + ((log(x) - log(tauz))./sigma).^2));

% rimaginary part of susceptibility for single relaxation time
z = (2.*pi.*omega.*x).*dist(x)./(1 + (2.*pi.*omega.*x).^2);

[n, ¬] = size(z);
im = [];
for i = 1 : n
x = logspace(-5,-1,1e2);
y = z(i, :);
idx = isnan(y);
x(idx) = [];
y(idx) = [];
im = cat(1, im, trapz(x, y));
end

% imaginary part of suscptibility for a range of relaxation times
IM = (Xz - Xinf).*im;

end
```

```
%% a combined function to fit real and imaginary parts simultaneously ...
  using shared parameters

function total = combined_function(omega,sigma1,tauz1,Xinf1,Xz1)

cheat = false;

if floor(length(omega) / 2) * 2 ¬ = length(omega)
cheat = true;
end

if ¬cheat
% frequency array
wReal = omega(1 : length(omega)/2);
wImag = −omega(length(omega)/2 + 1 : end);

% susceptibility array
yReal = real(wReal,sigma1,tauz1,Xinf1,Xz1);
yImag = imag(wImag,sigma1,tauz1,Xinf1,Xz1);
total = [yReal ; yImag];

else
total = omega;
warning('make sure this is intended');
end

end
```

Bibliography

[1] H. Eugene Stanley. Scaling, universality, and renormalization: Three pillars of modern critical phenomena. *Reviews of Modern Physics*, 71(2):S358–S366, March 1999.

[2] Somendra M Bhattacharjee and Flavio Seno. A measure of data collapse for scaling. *Journal of Physics A: Mathematical and General*, 34(33):6375–6380, August 2001.

[3] Leon Gunther. Quantum tunneling of magnetization. In J. L. Dormann and D. Fiorani, editors, *Magnetic Properties of Fine Particles*, North-Holland Delta Series, pages 213–224. Elsevier, Amsterdam, January 1992.

[4] Hironori Nishihara, Hiroshi Yasuoka, and Akira Hirai. NMR of Co59 in an Approximate Ising System: CoCl2·2H2O. *Journal of the Physical Society of Japan*, 32(4):1135–1145, April 1972.

[5] Krunoslav Prsa, Mark Laver, Martin Mansson, Sebastian Guerrero, Peter M. Derlet, Ivica Zivkovic, Hee Taek Yi, Lionel Porcar, Oksana Zaharko, Sandor Balog, Jorge L. Gavilano, Joachim Kohlbrecher, Bertrand Roessli, Christof Niedermayer, Jun Sugiyama, Cecile Garcia, Henrik M. Ronnow, Christopher Mudry, Michel Kenzelmann, Sang Wook Cheong, and Joel Mesot. Magnetic nano-fluctuations in a frustrated magnet. *arXiv:1404.7398 [cond-mat]*, April 2014. arXiv: 1404.7398.

[6] C V Topping and S J Blundell. A.C. susceptibility as a probe of low-frequency magnetic dynamics. *Journal of Physics: Condensed Matter*, 31(1):013001, January 2019.

[7] K Binder. Theory of first-order phase transitions. *Reports on Progress in Physics*, 50(7):783–859, July 1987.

[8] Paul Ehrenfest. *Phasenumwandlungen im ueblichen und erweiterten Sinn, classifiziert nach den entsprechenden Singularitaeten des thermodynamischen Potentiales.* N. V. Noord-Hollandsche Uitgevers Maatschappij, 1933.

[9] Tilman Sauer. A Look Back at the Ehrenfest Classification. Translation and Commentary of Ehrenfest's 1933 paper introducing the notion of phase transitions of different order. *The European Physical Journal Special Topics*, 226(4):539–549, April 2017. arXiv: 1612.03062.

[10] Kerson Huang. *Statistical mechanics*. Wiley, New York, 2nd ed edition, 1987.

[11] J. M. Yeomans and Joseph Rudnick. Statistical Mechanics of Phase Transitions. *Physics Today*, 46(7):80, January 2008.

[12] Praveen Chaddah. *First Order Phase Transitions of Magnetic Materials : Broad and Interrupted Transitions*. CRC Press, November 2017.

[13] R. Prozorov and V. G. Kogan. Effective Demagnetizing Factors of Diamagnetic Samples of Various Shapes. *Physical Review Applied*, 10(1):014030, July 2018.

[14] Vladimir Privman and Michael E. Fisher. Finite-size effects at first-order transitions. *Journal of Statistical Physics*, 33(2):385–417, November 1983.

[15] Yoseph Imry and Michael Wortis. Influence of quenched impurities on first-order phase transitions. *Physical Review B*, 19(7):3580–3585, April 1979.

[16] Alexander S. Abyzov and Jürn W. P. Schmelzer. Nucleation versus spinodal decomposition in confined binary solutions. *The Journal of Chemical Physics*, 127(11):114504, September 2007.

[17] E. Stryjewski and N. Giordano. Metamagnetism. *Advances in Physics*, 26(5):487–650, September 1977.

[18] Oleg A Starykh. Unusual ordered phases of highly frustrated magnets: a review. *Reports on Progress in Physics*, 78(5):052502, May 2015.

[19] A. V. Zarubin, F. A. Kassan-Ogly, and A. I. Proshkin. Frustrations in the Ising chain with the third-neighbor interactions. *Journal of Magnetism and Magnetic Materials*, 514:167144, November 2020. arXiv: 2002.05430.

[20] Claudine Lacroix, Philippe Mendels, and Frédéric Mila, editors. *Introduction to Frustrated Magnetism*, volume 164 of *Springer Series in Solid-State Sciences*. Springer Berlin Heidelberg, Berlin, Heidelberg, 2011.

[21] B. Sriram Shastry and Bill Sutherland. Exact ground state of a quantum mechanical antiferromagnet. *Physica B+C*, 108(1):1069–1070, August 1981.

[22] Masaki Oshikawa, Masanori Yamanaka, and Ian Affleck. Magnetization Plateaus in Spin Chains: "Haldane Gap" for Half-Integer Spins. *Physical Review Letters*, 78(10):1984–1987, March 1997.

[23] A. Maignan, V. Hardy, S. Hébert, M. Drillon, M. R. Lees, O. Petrenko, D. Mc K. Paul, and D. Khomskii. Quantum tunneling of the magnetization in the Ising chain compound Ca3Co2O6. *Journal of Materials Chemistry*, 14(8):1231–1234, April 2004.

[24] K. C. Rule, A. U. B. Wolter, S. Süllow, D. A. Tennant, A. Brühl, S. Köhler, B. Wolf, M. Lang, and J. Schreuer. Nature of the Spin Dynamics and \$1/3\$ Magnetization Plateau in Azurite. *Physical Review Letters*, 100(11):117202, March 2008.

[25] Norio Achiwa. Linear Antiferromagnetic Chains in Hexagonal ABCl3-Type Compounds (A; Cs, or Rb, B; Cu, Ni, Co, or Fe). *Journal of the Physical Society of Japan*, 27(3):561–574, September 1969.

[26] Mamoru Mekata. Antiferro-Ferrimagnatic Transition in Triangular Ising Lattice. *Journal of the Physical Society of Japan*, 42(1):76–82, January 1977.

[27] Hans-Conrad zur Loye, Qingbiao Zhao, Daniel E. Bugaris, and W. Michael Chance. 2H-perovskite related oxides: Synthesis, structures, and predictions. *CrystEngComm*, 14(1):23–39, December 2011.

[28] M. Ge, O. B. Korneta, T. F. Qi, S. Parkin, P. Schlottmann, and G. Cao. Magnetic anisotropy and geometrical frustration in the Ising spin-chain system Sr5Rh4O12. *Journal of Applied Physics*, 109(7):07E164, April 2011.

[29] G. Cao, V. Durairaj, S. Chikara, S. Parkin, and P. Schlottmann. Partial antiferromagnetism in spin-chain Sr5Rh4O12, Ca5Ir3O12, and Ca4IrO6 single crystals. *Physical Review B*, 75(13):134402, April 2007.

[30] Yurii B. Kudasov, Aleksei S. Korshunov, V. N. Pavlov, and Dmitrii A. Maslov. Frustrated lattices of Ising chains. *Physics-Uspekhi*, 55(12):1169, 2012.

[31] V. Hardy, C. Martin, G. Martinet, and G. André. Magnetism of the geometrically frustrated spin-chain compound Sr 3 Ho Cr O 6 : Magnetic and heat capacity measurements and neutron powder diffraction. *Physical Review B*, 74(6):064413, August 2006.

[32] Xiaoyan Yao. 1/3 Magnetization Plateau Induced by Magnetic Field in Monoclinic CoV2O6. *The Journal of Physical Chemistry A*, 116(9):2278–2282, March 2012.

[33] H. Weitzel and W. Schneider. Neutron diffraction determination of the magnetic phases of CoCl2·2H2O. *Solid State Communications*, 14(10):1025–1027, May 1974.

[34] JAMES SETHNA. *STATISTICAL MECHANICS: entropy, order parameters, and complexity.* OXFORD UNIV PRESS, S.l., 2021. OCLC: 1190831345.

[35] Rodney J Baxter. *Exactly Solved Models in Statistical Mechanics.* 2016. OCLC: 1050372285.

[36] Eduard Vives, Jürgen Goicoechea, Jordi Ortín, and Antoni Planes. Universality in models for disorder-induced phase transitions. *Physical Review E*, 52(1):R5–R8, July 1995.

[37] Karin Dahmen and James P. Sethna. Hysteresis, avalanches, and disorder-induced critical scaling: A renormalization-group approach. *Physical Review B*, 53(22):14872–14905, June 1996.

[38] Guang-Ping Zheng and Mo Li. Dynamic scaling for avalanches in disordered systems. *Physical Review E*, 63(3):036122, February 2001.

[39] Olga Perković, Karin A. Dahmen, and James P. Sethna. Disorder-induced critical phenomena in hysteresis: Numerical scaling in three and higher dimensions. *Physical Review B*, 59(9):6106–6119, March 1999.

[40] T. R. Kirkpatrick and D. Thirumalai. Universal aspects of the random first order phase transition theory of the structural glass transition. *arXiv:1401.2024 [cond-mat]*, January 2014. arXiv: 1401.2024.

[41] Michael E. Fisher and A. Nihat Berker. Scaling for first-order phase transitions in thermodynamic and finite systems. *Physical Review B*, 26(5):2507–2513, September 1982.

[42] M. Bałanda. AC Susceptibility Studies of Phase Transitions and Magnetic Relaxation: Conventional, Molecular and Low-Dimensional Magnets. *Acta Physica Polonica A*, 124(6):964–976, December 2013.

[43] H. B. G. Casimir and F. K. du Pré. Note on the thermodynamic interpretation of paramagnetic relaxation phenomena. *Physica*, 5(6):507–511, June 1938.

[44] Malay Bandyopadhyay and Sushanta Dattagupta. Memory in nanomagnetic systems: Superparamagnetism versus spin-glass behavior. *Physical Review B*, 74(21):214410, December 2006.

[45] J A Mydosh. *Spin Glasses : An Experimental Introduction.* CRC Press, May 1993.

[46] C. Paulsen, M. J. Jackson, E. Lhotel, B. Canals, D. Prabhakaran, K. Matsuhira, S. R. Giblin, and S. T. Bramwell. Far-from-equilibrium monopole dynamics in spin ice. *Nature Physics*, 10(2):135–139, February 2014.

[47] J. L. Dormann, D. Fiorani, and E. Tronc. Magnetic Relaxation in Fine-Particle Systems. In *Advances in Chemical Physics*, pages 283–494. John Wiley & Sons, Ltd, 1997.

[48] Petra E. Jönsson. Superparamagnetism and Spin Glass Dynamics of Interacting Magnetic Nanoparticle Systems. *arXiv:cond-mat/0310684*, October 2003. arXiv: cond-mat/0310684.

[49] X. X. Zhang. Magnetic Relaxation and Quantum Tunneling of Magnetization. In Yi Liu, David J. Sellmyer, and Daisuke Shindo, editors, *Handbook of Advanced Magnetic Materials*, pages 147–181. Springer US, Boston, MA, 2006.

[50] Dante Gatteschi and Roberta Sessoli. Quantum Tunneling of Magnetization and Related Phenomena in Molecular Materials. *Angewandte Chemie International Edition*, 42(3):268–297, 2003.

[51] S. Aasland, H. Fjellvåg, and B. Hauback. Magnetic properties of the one-dimensional Ca3Co2O6. *Solid State Communications*, 101(3):187–192, January 1997.

[52] V. Hardy, D. Flahaut, M. R. Lees, and O. A. Petrenko. Magnetic quantum tunneling in ca3co2o6 studied by ac susceptibility: Temperature and magnetic-field dependence of the spin-relaxation time. *Physical Review B*, 70(21):214439, December 2004.

[53] Brett Leedahl, Martin Sundermann, Andrea Amorese, Andrea Severing, Hlynur Gretarsson, Lunyong Zhang, Alexander C. Komarek, Antoine Maignan, Maurits W. Haverkort, and Liu Hao Tjeng. Origin of Ising magnetism in Ca 3 Co 2 O 6 unveiled by orbital imaging. *Nature Communications*, 10(1):5447, November 2019.

[54] G. Allodi, P. Santini, S. Carretta, S. Agrestini, C. Mazzoli, A. Bombardi, M. R. Lees, and R. De Renzi. Exchange interactions in Ca${}_{3}$Co${}_{2}$O${}_{6}$ probed locally by NMR. *Physical Review B*, 89(10):104401, March 2014.

[55] S. Agrestini, L. C. Chapon, A. Daoud-Aladine, J. Schefer, A. Gukasov, C. Mazzoli, M. R. Lees, and O. A. Petrenko. Nature of the Magnetic Order in ${\mathrm{Ca}}_{3}{\mathrm{Co}}_{2}{\mathrm{O}}_{6}$. *Physical Review Letters*, 101(9):097207, August 2008.

[56] Taketo Moyoshi and Kiyoichiro Motoya. Incommensurate Magnetic Structure and Its Long-Time Variation in a Geometrically Frustrated Magnet Ca3Co2O6. *Journal of the Physical Society of Japan*, 80(3):034701, February 2011.

[57] Kiyoichiro Motoya, Takumi Kihara, Hiroyuki Nojiri, Yoshiya Uwatoko, Masaaki Matsuda, and Tao Hong. Time and Magnetic Field Variations of Magnetic Structure in the Triangular Lattice Magnet Ca3Co2O6. *Journal of the Physical Society of Japan*, 87(11):114703, October 2018.

[58] O. A. Petrenko, J. Wooldridge, M. R. Lees, P. Manuel, and V. Hardy. Single crystal neutron diffraction study of the magnetisation process in Ca3Co2O6. *The European Physical Journal B - Condensed Matter and Complex Systems*, 47(1):79–83, September 2005.

[59] S. Agrestini, C. L. Fleck, L. C. Chapon, C. Mazzoli, A. Bombardi, M. R. Lees, and O. A. Petrenko. Slow Magnetic Order-Order Transition in the Spin Chain Antiferromagnet ${\mathrm{Ca}}_{3}{\mathrm{Co}}_{2}{\mathrm{O}}_{6}$. *Physical Review Letters*, 106(19):197204, May 2011.

[60] Y. Kamiya and C. D. Batista. Formation of Magnetic Microphases in ca3co2o6. *Physical Review Letters*, 109(6):067204, August 2012.

[61] W. Decelle, J. Vanacken, V. V. Moshchalkov, J. Tejada, J. M. Hernández, and F. Macià. Propagation of Magnetic Avalanches in ${\mathrm{Mn}}_{12}\mathrm{Ac}$ at High Field Sweep Rates. *Physical Review Letters*, 102(2):027203, January 2009.

[62] Zhangzhen He, Jun-Ichi Yamaura, Yutaka Ueda, and Wendan Cheng. CoV2O6 Single Crystals Grown in a Closed Crucible: Unusual Magnetic Behaviors with Large Anisotropy and 1/3 Magnetization Plateau. *Journal of the American Chemical Society*, 131(22):7554–7555, June 2009.

[63] Mikael Markkula, Angel M. Arevalo-Lopez, and J. Paul Attfield. Neutron diffraction study of monoclinic brannerite-type CoV2O6. *Journal of Solid State Chemistry*, 192:390–393, August 2012.

[64] M. Lenertz, J. Alaria, D. Stoeffler, S. Colis, and A. Dinia. Magnetic Properties of Low-Dimensional $\alpha$ and $\gamma$ CoV2O6. *The Journal of Physical Chemistry C*, 115(34):17190–17196, September 2011.

[65] Zhangzhen He and Wendan Cheng. Magnetic phase diagram of an Ising spin-chain system $\alpha$-CoV2O6 with 1/3 magnetization plateau. *Journal of Magnetism and Magnetic Materials*, 362:27–30, August 2014.

[66] Yvo Drees, Stefano Agrestini, Oksana Zaharko, and Alexander Christoph Komarek. Floating Zone Single Crystal Growth of $\gamma$-CoV2O6 with Substantially Enhanced Crystal Size and Quality. *Crystal Growth & Design*, 15(3):1168–1172, March 2015.

[67] N. Hollmann, S. Agrestini, Z. Hu, Z. He, M. Schmidt, C.-Y. Kuo, M. Rotter, A. A. Nugroho, V. Sessi, A. Tanaka, N. B. Brookes, and L. H. Tjeng. Spectroscopic evidence for giant orbital moment and magnetic anisotropy induced by local distortions in $alpha$-CoV2O6. *Physical Review B*, 89(20):201101, May 2014. arXiv: 1307.6690.

[68] Hiroshi Mollymoto, Mitsuhiro Motokawa, and Muneyuki Date. High Field Transverse Magnetization of Ising Antiferromagnet CoCl2·2H2O. *Journal of the Physical Society of Japan*, 49(1):108–114, July 1980.

[69] J. Larsen, T. K. Schäffer, U. B. Hansen, S. L. Holm, S. R. Ahl, R. Toft-Petersen, J. Taylor, G. Ehlers, J. Jensen, H. M. Rønnow, K. Lefmann, and N. B. Christensen. Spin excitations and quantum criticality in the quasi-one-dimensional Ising-like ferromagnet cocl2.2h2o in a transverse field. *Physical Review B*, 96(17):174424, November 2017.

[70] Jens Jensen, Jacob Larsen, and Ursula B. Hansen. Comprehensive cluster-theory analysis of the magnetic structures and excitations in cocl2.2h2o. *Physical Review B*, 97(2):024423, January 2018.

[71] M. Tinkham. Microscopic Dynamics of Metamagnetic Transitions in an Approximately Ising System: Co Cl 2 ·2 H 2 O. *Physical Review*, 188(2):967–973, December 1969.

[72] M. Blume. Magnetic scattering of x rays (invited). *Journal of Applied Physics*, 57(8):3615–3618, April 1985.

[73] J. Bohr. Magnetic X-ray scattering: A new tool for magnetic structure investigations. *Journal of Magnetism and Magnetic Materials*, 83(1-3):530–534, January 1990.

[74] H. A. D&uuml;rr. Chiral Magnetic Domain Structures in Ultrathin FePd Films. *Science*, 284(5423):2166–2168, June 1999.

[75] Guillaume Beutier, Alain Marty, Frédéric Livet, Gerrit van der Laan, Stefan Stanescu, and Peter Bencok. Soft x-ray coherent scattering: Instrument and methods at ESRF ID08. *Review of Scientific Instruments*, 78(9):093901, September 2007.

[76] J. Miao, T. Ishikawa, I. K. Robinson, and M. M. Murnane. Beyond crystallography: Diffractive imaging using coherent x-ray light sources. *Science*, 348(6234):530–535, May 2015.

[77] Friso van der Veen and Franz Pfeiffer. Coherent x-ray scattering. *Journal of Physics: Condensed Matter*, 16(28):5003–5030, July 2004.

[78] J. Miguel, J. F. Peters, O. M. Toulemonde, S. S. Dhesi, N. B. Brookes, and J. B. Goedkoop. X-ray resonant magnetic scattering study of magnetic stripe domains in $\alpha$ GdFe thin films. *Physical Review B*, 74(9):094437, September 2006.

[79] V. Hardy, S. Lambert, M. R. Lees, and D. McK. Paul. Specific heat and magnetization study on single crystals of the frustrated quasi-one-dimensional oxide ca3co2o6. *Physical Review B*, 68(1):014424, July 2003.

[80] E. Riordan, J. Blomgren, C. Jonasson, F. Ahrentorp, C. Johansson, D. Margineda, A. Elfassi, S. Michel, F. Dell'ova, G. M. Klemencic, and S. R. Giblin. Design and implementation of a low temperature, inductance based high frequency alternating current susceptometer. *Review of Scientific Instruments*, 90(7):073908, July 2019.

[81] A. Maignan, C. Michel, A.C. Masset, C. Martin, and B. Raveau. Single crystal study of the one dimensional Ca Co O compound: five stable configurations for the Ising triangular lattice. *The European Physical Journal B - Condensed Matter and Complex Systems*, 15(4):657–663, June 2000.

[82] Christopher Jarzynski. Diverse phenomena, common themes. *Nature Physics*, 11(2):105–107, February 2015.

[83] D Huser, A J van Duyneveldt, G J Nieuwenhuys, and J A Mydosh. Phenomenological model for the frequency dependence of the susceptibility of spin glasses and related compounds. *Journal of Physics C: Solid State Physics*, 19(19):3697–3717, July 1986.

[84] Anil Jain, P. Y. Portnichenko, Hoyoung Jang, G. Jackeli, G. Friemel, A. Ivanov, A. Piovano, S. M. Yusuf, B. Keimer, and D. S. Inosov. One-dimensional dispersive magnon excitation in the frustrated spin-2 chain system Ca\$\{\}_\{3\}\$Co\$\{\}_\{2\}\$O\$\{\}_\{6\}\$. *Physical Review B*, 88(22):224403, December 2013.

[85] Soshi Takeshita, Juichiro Arai, Tatsuo Goko, Kusuo Nishiyama, and Kanetada Nagamine. Muon Spin Relaxation Study of Partially Disordered State in Triangular-Lattice Antiferromagnet: Ca3Co2O6. *Journal of the Physical Society of Japan*, 75(3):034712, March 2006.

[86] M. Månsson, J. Sugiyama, B. Roessli, B. Hitti, Y. Ikedo, I. Zivkovic, H. Nozaki, M. Harada, Y. Sassa, D. Andreica, T. Goko, A. Amato, O. Ofer, E. J. Ansaldo, J. H. Brewer, K. H. Chow, H. T. Yi, S.-W. Cheong, and K. Prsa. Magnetic Spin Correlations in the One-dimensional Frustrated Spin-chain System Ca3Co2O6. In *Proceedings of the 14th International Conference on Muon Spin Rotation, Relaxation and Resonance (?SR2017)*, volume 21 of *JPS Conference Proceedings*. Journal of the Physical Society of Japan, February 2018.

[87] H. Shu, Z. W. Ouyang, Y. C. Sun, M. Y. Ruan, J. J. Li, X. Y. Yue, Z. X. Wang, Z. C. Xia, and G. H. Rao. Size-dependent magnetism in nanocrystals of spin-chain α-CoV2O6. *Journal of Magnetism and Magnetic Materials*, 407:129–134, June 2016.

[88] G. C. DeFotis, R. V. Chamberlain, W. R. A. Jarvis, and D. J. Krovich. Magnetism and spin glass behavior of CoCl2·H2O. *Journal of Magnetism and Magnetic Materials*, 104-107:1603–1604, February 1992.

[89] Yōichi Kuramitsu, Kiichi Amaya, and Taiichiro Haseda. Relaxation Phenomena of Metamagnetic Transition in CoCl2·2H2O. *Journal of the Physical Society of Japan*, 33(1):83–87, July 1972.

[90] D. H. Reich, B. Ellman, J. Yang, T. F. Rosenbaum, G. Aeppli, and D. P. Belanger. Dipolar magnets and glasses: Neutron-scattering, dynamical, and calorimetric studies of randomly distributed Ising spins. *Physical Review B*, 42(7):4631–4644, September 1990.

[91] Jeffrey B. Kortright, Olav Hellwig, Karine Chesnel, Shouheng Sun, and Eric E. Fullerton. Interparticle magnetic correlations in dense Co nanoparticle assemblies. *Physical Review B*, 71(1):012402, January 2005.

[92] Claudio Mazzoli. Resonant X-ray scattering study of Ca3Co2O6 ground state: Preliminary results of magnetic field effects. *Physica B: Condensed Matter*, 404(19):3042–3044, October 2009.

[93] S.-W. Chen, H. Guo, K. A. Seu, K. Dumesnil, S. Roy, and S. K. Sinha. Jamming Behavior of Domains in a Spiral Antiferromagnetic System. *Physical Review Letters*, 110(21):217201, May 2013.

[94] Allen Scheie. LongHCPulse: Long-Pulse Heat Capacity on a Quantum Design PPMS. *Journal of Low Temperature Physics*, 193(1):60–73, October 2018.

[95] Paula "Paige" Lampen-Kelley. Impact of reduced dimensionality on the correlation length and magnetization dynamics of the spin chain cobaltite Ca3Co2O6. *Journal of Magnetism and Magnetic Materials*, 493:165690, January 2020.

[96] Paul F. McMillan and H. Eugene Stanley. Going supercritical. *Nature Physics*, 6(7):479–480, July 2010.

[97] Muralikrishna Raju, Daniel T. Banuti, Peter C. Ma, and Matthias Ihme. Widom Lines in Binary Mixtures of Supercritical Fluids. *Scientific Reports*, 7(1):3027, June 2017.

[98] Per Bak and J. von Boehm. Ising model with solitons, phasons, and "the devil's staircase". *Physical Review B*, 21(11):5297–5308, June 1980.

[99] Aniello Lampo, Javier Borge-Holthoefer, Sergio Gómez, and Albert Solé-Ribalta. Multiple abrupt phase transitions in urban transport congestion. *Physical Review Research*, 3(1):013267, March 2021.

[100] Ryogo Kubo. Statistical-Mechanical Theory of Irreversible Processes. I. General Theory and Simple Applications to Magnetic and Conduction Problems. *Journal of the Physical Society of Japan*, 12(6):570–586, June 1957.

[101] J. I. Gittleman, B. Abeles, and S. Bozowski. Superparamagnetism and relaxation effects in granular nisio2 and nial2o3 films. *Physical Review B*, 9(9):3891–3897, May 1974.

[102] Daniel Esmarch Madsen, Mikkel Fougt Hansen, and Steen Mørup. The correlation between superparamagnetic blocking temperatures and peak temperatures obtained from ac magnetization measurements. *Journal of Physics: Condensed Matter*, 20(34):345209, August 2008.

[103] K. Inoue, H. Shima, A. Fujita, K. Ishida, K. Oikawa, and K. Fukamichi. Temperature dependence of magnetocrystalline anisotropy constants in the single variant state of L10-type FePt bulk single crystal. *Applied Physics Letters*, 88(10):102503, March 2006.

Nagabhushan Ganesh Hegde

Assistant-doctorant – Laboratoire de magnétisme quantique
École Polytechnique Fédérale de Lausanne – Station 3, CH-1015
✉ nagabhushan.ganesh@epfl.ch
✉ nagabhushan.ganesh.hegde@gmail.ch

Education

09/2017–present	*PhD*	École Polytechnique Fédérale de Lausanne
08/2012–04/2017	*BSMS*	Indian Institute of Science Education and Research Thiruvananthapuram

Research

09/2017–present Graduate	*Investigation of Universal Aspects across Metamagnetic Transitions in Frustrated Ising Magnets* *Advisors*: Prof. Henrik M. Rønnow, Dr. Ivica Zivkovic *Laboratory for Quantum Magnetism* EPFL (Funded by Swiss National Science Foundation SNSF)
05/2016–04/2017 Masters	*Synthesis and Characterization of Spin-$5/2$ Dimer and Spin-$1/2$ TLAF* *Advisor*: Dr. Ramesh Chandra Nath *School of Physics* IISER TVM

Publications

1. "*Magnetic dynamics across the in-field transition in $Ca_3Co_2O_6$*"
   Nagabhushan G Hegde, Ivana Levatic, Arnaud Magrez, Henrik M Rønnow and Ivica Zivkovic
   Physical Review B **102** 104418 (2020)

2. "*Triangular and Linear Co3 Cluster Based Metal-Organic Frameworks: Structures and Magnetic Properties*"
   Prabu Mani, Prashanta Mukharjee, **Nagabhushan G Hegde**, Ramesh Chandra Nath, Sukhendu Mandal
   Journal of Solid State Chemistry **265** 123-128 (2018)

3. "*Double phase transition in the triangular antiferromagnet $Ba_3CoTa_2O_9$*"
   K M Ranjith, K Brinda, U Arjun, **N G Hegde** and R Nath
   J. Phys.: Condens. Matter **29** 115804 (2017)

Experimental Skills

- Magnetometry (PPMS, MPMS) - VSM & AC modules
- Powder- & Single Crystal XRD

Programming Languages

- MATLAB (intermediate)
- Python (basic)
- LabVIEW (basic)
- Solidworks

Large Facility Experiments

09/2020	Magnetic SANS	Institut Laue-Langevin
10/2019	Coherent Soft X-ray Scattering	Brookhaven National Laboratory
11/2018	Single Crystal XRD	European Synchrotron Radiation Facility
05/2018	Polarized Neutrons & TOF	Forschungsreaktor München II
11/2017	μSR: GPS & LTF	Paul Scherrer Institute

Teaching Experience

Autumn 2020	Phys 309	Solid State Physics I
Autumn 2019	Phys 309	Solid State Physics I
Spring 2019	Math 115(b)	Advanced Linear Algebra II
Autumn 2018	Phys 114	Electromagnetism
Spring 2018	Math 1B	Mise à niveau (MAN)
Autumn 2017	Phys 324	Classical Electrodynamics

Schools/Workshops

08/2019	*Contributed Poster–* Summer School on Quantum Magnetism, EPFL
05/2019	*Contributed Poster–* Quantum Ferromagnetism and Related Phenomena, MPI-PKS Dresden
04/2018	Powder Diffraction and Rietveld Refinement School, Durham University
03/2018	38th Berlin School on Neutron Scattering, Helmholtz-Zentrum Berlin
04/2017	*Contributed Poster–* School on Frustrated Magnetism, IMSc Chennai
07/2016	Ultracold Few- and Many- Body Systems: Quantum Mechanics Made Crystal Clear, Uni-Freiburg
12/2014	Lecture Workshop on Classical Mechanics, Loyola College Chennai
12/2013	Vijyoshi Science Camp, IISc Bengaluru (KVPY Fellow)
12/2012	Vijyoshi Science Camp, IISc Bengaluru (INSPIRE Scholar)
01/2009	Five-day nurturance programme for NTSE Awardees, RIE Mysuru (*sponsored by* NCERT)

Conferences/Symposium

08/2018	*Contributed Poster–* Annual Meeting of the Swiss Physical Society, EPFL
04/2017	*Contributed Poster–* Conference on Frustrated Magnetism, IMSc Chennai
09/2016	Student Conference on Optics and Photonics, PRL Ahmedabad
03/2016	International Symposium on Cluster, Cluster-Assemblies and Nanomaterials, IISER TVM
07/2014	National Conference on Materials Science and Technology, IIST Thiruvananthapuram

Academic Honors

◦ Joint CSIR-UGC Test: *All India Rank 87* (Lectureship) [Roll No. 501096]	12/2016
◦ Kishore Vaigyanik Protsahan Yojana (KVPY) *Fellowship*	2013–2017
◦ Innovation in Science Pursuit for Inspired Research (INSPIRE) *Fellowship*	2012–2013
◦ National Talent Search Exam (NTSE) *Scholarship*	2009–2012

Extracurricular

◦ Weekly football match organization	2 years
◦ Video editing (using Premiere Pro)	6 months

Languages

◦ English	fluent (C1-C2)
◦ French	basic (A2)
◦ Kannada	Native

Last Updated: May 17, 2021